8-1-2001

Collection and analysis of multispectral magnetic resonance imaging data using a clinical imaging system

Thomas G. Servoss

Collection and Analysis of Multispectral Magnetic Resonance Imaging Data using a Clinical Imaging System

BY

THOMAS G. SERVOSS

M.S. IMAGING SCIENCE ROCHESTER INSTITUTE OF TECHNOLOGY, 1993

A THESIS SUBMITTED IN PARTIAL FULFILLMENT OF THE
REQUIREMENTS FOR THE DEGREE OF DOCTOR OF PHILOSOPHY
IN THE CHESTER F. CARLSON CENTER FOR IMAGING SCIENCE
IN THE COLLEGE OF SCIENCE OF THE
ROCHESTER INSTITUTE OF TECHNOLOGY

AUGUST 2001

SIGNATURE OF AUTHOR _____

ACCEPTED BY Henry E. Rhody

COORDINATOR, PH.D. DEGREE PROGRAM

COLLEGE OF SCIENCE

ROCHESTER INSTITUTE OF TECHNOLOGY

ROCHESTER, NEW YORK

CERTIFICATE OF APPROVAL

PH.D. DEGREE THESIS

The Ph.D. Degree Thesis of Thomas G. Servoss has been examined and approved by the thesis committee as satisfactory for the thesis requirement for the Ph.D. degree in Imaging Science.

DR. JOSEPH P. HORNAK

DR. JEROME WAGNER

DR. ROBERT D. FIETE

DR. NAVALGUND RAO

DR. JIANHUI ZHONG

8/23/01

DATE

THESIS RELEASE PERMISSION

ROCHESTER INSTITUTE OF TECHNOLOGY

ROCHESTER, NEW YORK

Collection and Analysis of Multispectral Magnetic Resonance Imaging Data using a Clinical Imaging System

I, Thomas G. Servoss, hereby grant permission to Wallace Memorial Library of RIT to reproduce my thesis in whole or in part. Any reproduction will not be for commercial use or profit.

Thomas G. Servoss

8/23/01

Date

Collection and Analysis of Multispectral Magnetic Resonance Imaging Data using a Clinical Imaging System

BY

THOMAS G. SERVOSS

SUBMITTED TO THE
CHESTER F. CARLSON CENTER FOR IMAGING SCIENCE
IN PARTIAL FULFILLMENT OF THE REQUIREMENTS
FOR THE DOCTOR OF PHILOSOPHY DEGREE
AT THE ROCHESTER INSTITUTE OF TECHNOLOGY

AUGUST 2001

Abstract

As most radiologists would attest, the accuracy of pathology diagnosis is greatly increased by acquiring more information about the tissue in question. An innovative data acquisition technique has been developed that will do just that - gather more information about the tissues being studied. As each tissue type is composed of a unique arrangement of chemical components, each tissue exhibits a characteristic nuclear magnetic resonance (NMR) frequency spectrum. Unfortunately, current clinical magnetic resonance imaging (MRI) systems integrate the characteristic spectra of the tissue within a voxel to create a single signal for the voxel, thus throwing away what could be invaluable information. In an effort to regain the typically discarded information, a spatial-spatial-spectral imaging technique has been developed and demonstrated using a clinical MRI system. The technique, which was originally developed and demonstrated by Lauterbur on a NMR system, involves acquiring projections through the spatial-spectral plane of

the spatial-spatial-spectral volume and reconstructing that plane through use of a back-projection procedure. This technique is made possible on clinical MRI systems through the advent of variable bandwidth imaging – a technological advance that allows for a variation in the sampling bandwidth used in the acquisition steps of MRI. Combined with specific variations of the frequency-encoding gradient, specific bandwidth values can be used with existing pulse sequences to acquire projections through the spatial-spectral plane at very particular angles. The technique has been demonstrated on a 1.5T, whole-body, clinical imaging system (Signa, GE Medical Systems, Milwaukee, WI) using chemical shift phantoms as well as *in vivo* tissue. In addition, the accuracy of the technique has been analyzed via point spread function (PSF) estimation and classification accuracy techniques. The impacts on these analysis metrics due to variations in acquisition and processing parameters have also been investigated.

Acknowledgments

MY COMMITTEE

I'd like to thank my dissertation committee for applying a portion of their time toward the betterment of my education. I have benefited from their knowledge and experience and for this, I am grateful.

THE CIS FACULTY & STAFF

I'd like to thank the CIS faculty and staff for their assistance and cooperation in guiding me through the maze of logistical issues involved with completion of this research and the program. Particular thanks go to Sue Chan, Georgia Rothacker, and Bryce Nordgren.

MY FRIENDS

I'd like to thank my friends for their support and understanding when I was more compelled to work on this project than I was to join them in revelry.

MY FAMILY

I'd like to thank my family. Without their support, assistance, guidance, and love none of this would have been possible.

MY ADVISOR

Finally, I'd like to thank Dr. Joseph Hornak. I'm sure Dr. Hornak never imagined that I was going to walk into his office on the day in August 1996 and demand that he work with me on this project. Thank you for your patience and guidance, Joe. I couldn't have done it without you.

Dedication

Elizabeth,

to you I dedicate this work.

Your patience, understanding, encouragement, and love not only made this work possible,

but also made it a reality.

Thank you for believing in me.

Table of Contents

Heading **Page**

Abstract iv

Acknowledgments vi

Dedication vii

Table of Contents viii

Table of Figures xi

Table of Tables xv

Table of Symbols xvii

1. Introduction 1

1.1 Motivation 3

1.2 Goals 6

2. Background 8

2.1 MRI Image Formation 8

2.1.1 Larmor Frequency 8

2.1.2 Fourier Imaging 10

2.1.3 Coordinate Systems 13

2.1.4 Signal Generation & Recording 14

2.1.5 Timing Diagram 19

2.1.6 Signal Decay 21

2.2 Chemical Shift Artifact 26

2.2.1 Cause of Chemical Shift 27

2.2.2 Effects of Chemical Shift 28

2.2.3 Variable Bandwidth 30

2.3 Magnetic Resonance Spectroscopy 33

2.3.1 Localization 35

2.3.2 Phase-Encoding Imaging 36

2.4 Radon Transform 38

2.4.1 Example Scenario *39*
2.4.2 Data Transformation *41*
2.4.2.1 Sinograms 43
2.4.3 Backprojection *46*
2.4.4 Filtering *48*

3. Spatial-Spatial-Spectral Theory 50

3.1 Foundation Research 51

3.2 Multi-Spectral MRI (MSMRI) Approach 53
3.2.1 Sampling Bandwidth Selection *55*
3.2.2 Gradient Manipulation *57*

3.3 Post-acquisition Data Manipulation 59
3.3.1 Sinogram Creation *59*
3.3.2 Projection Interpolation *60*
3.3.3 Filtered Back-projection *64*

4. Experimental 66

4.1 3Tubes Phantom 68
4.1.1 Phantom Construction *68*
4.1.2 Data Acquisition *70*
4.1.3 Results *74*

4.2 Chambered Phantom 77
4.2.1 Phantom Construction *77*
4.2.2 Data Acquisition *81*
4.2.3 Results *86*
4.2.3.1 Three-Dimensional Surface Rendering 89

4.3 Susceptibility 92

4.4 In Vivo 96
4.4.1 Data Acquisition *96*
4.4.2 Results *99*
4.4.2.1 Three-Dimensional Surface Rendering 102

5. Analysis 104

5.1 Full Width at Half Max (FWHM) Measurements 104
5.1.1 T_2^* Discussion *105*
5.1.2 One Inch Diameter Spheres *105*
5.1.3 3Tubes FWHM *108*
5.1.3.1 Dependency upon # of projections 110
5.1.3.2 Expected FWHMs 113

5.2 Classification Analysis 119
5.2.1 3Tubes Classification *119*
5.2.2 Chambered Phantom Classification *124*
5.2.3 In vivo *Classification* *130*

6. Conclusions 133

6.1 Summary 133
6.2 Recommendations 136

References 139

Appendix A: Backprojection Filters 143

Appendix B: Spin-Echo Imaging 154

Appendix C: Imaging Parameters 158
3Tubes Phantom Collection Parameters 158
Chambered Phantom Collection Parameters 161
In Vivo Collection Parameters 163

Appendix D: Code 165
Sinogram Creation Code 165
Backprojection Code 167
MRI Image Conversion Code 168

Table of Figures

Figure **Page**

Figure 1 Various imaging systems depend on signals from various portions of the electromagnetic spectrum. 3

Figure 2 Acquiring imagery from various portions of the EM spectrum can take advantage of differences in spectral signature [2, page 25] 4

Figure 3 Camouflaged areas can go undetected in a panchromatic image (left), while they become apparent in an image created using signals from the NIR portion of the EM spectrum (right) Used with permission. [2, page 26 and color plate 2.5] 5

Figure 4 MR images are created via a Fourier Transform (FT) of k-space data. 11

Figure 5 Orthogonal gradients are used during MRI image acquisition. 12

Figure 6 Two coordinate systems are used in MRI, one stationary (x, y, z) and one rotating at the Larmor frequency (x', y', z). 14

Figure 7 Magnetic moment precession is similar to the precession exhibited by a spinning child's top when either is pushed away from alignment with the original spin axis 17

Figure 8 The net magnetic moment, M_0, is rotated to the transverse plane by applying B_1 to produce a recordable signal. 18

Figure 9 A simplified 90°-FID timing diagram (or pulse sequence) [3]. 19

Figure 10 Spin-Lattice relaxation time, T_1, describes the time it takes for ~63%, or $1\text{-}e^{-1}$, of the original net magnetic moment M_0, to realign with B_0. 23

Figure 11 After rotation down to the transverse plane (t=0), the net magnetic moment begins to diphase (t>0) at a rate described by T_2 24

Figure 12 Spin-Spin relaxation time, T_2, describes the time it takes for all but ~37%, or e^{-1}, of the transverse magnetic moment, M_{xy0}, to dephase. 25

Figure 13 Chemical shift is manifested as a separation of signals in MR images. Used with permission [3]. 29

Figure 14 (A) ^1H spectrum of rat brain tissue acquired via high-resolution NMR and (B) via surface coil MRS. Used with permission [16] 34

Figure 15 An example object used to demonstrate the principles of the Radon transform and its inverse: the backprojection. 39

Figure 16 An imaging plane (blue) was chosen such that all aspects of the example object were included. 40

Figure 17 Two dimensional slice through the example object. Each grey level represents a unique tissue type. 40

Figure 18 Projections at every angle compose the information held in the Radon transform. 42

Figure 19 A sinogram, b, is named as such due to the sinusoidal path described by an object, a, in the Radon domain. 44

Figure 20 A sinogram is a useful method in which to display Radon transform information. 44

Figure 21 A sinogram is a collection of all the projections in a 2-dimensional representation of the original object or slice. 46

Figure 22 The backprojection process smears each projection through the original object across the reconstruction space at a corresponding projection angle to reconstruct an estimate of the original object 47

Figure 23 The reconstruction estimate, b, of the original object, a, falls a little short implying a characteristic PSF of the process, but the Ram-Lak filtered reconstruction, c, is very representative of the original. 49

Figure 24 An example 1D object (cylindar at right) and its associated spatial-spectral signature used by Lauterbur to demonstrate his spatial-spectral imaging technique using an NMR spectrometer. Used with permission [1, pg. 537]. 52

Figure 25 Lauterbur, was able to demonstrate the result of his spatial-spectral technique by using a simulated object. Used with permission [1, pg. 539]. 53

Figure 26 Sampling rate is a function of projection angle. 55

Figure 27 A sinogram (right, S(x)) can be created using the data from the same column of each acquisition (left, $P(\theta)$). 60

Figure 28 Hardware and software limitations create a situation in which the acquired bandwidth does not match the desired bandwidth for most projections. 63

Figure 29 3Tube phantom solution spectra as measured by an NMR spectrometer (signal levels have been normalized to a common maximum). 69

Figure 30 The imaging slice through the 3Tubes phantom was oriented perpendicularly to the phantom's vertical axis. 71

Figure 31 As should be expected, the $\pi/2$, or purely spatial, projection appears to be a typical MRI acquisition. 74

Figure 32 The 0 degree, or purely spectral, projection does not appear to be a typical MRI acquisition. 74

Figure 33 The purely spatial projection image of the 3Tubes Phanotm (a) with a vertical line indicating the location of the (b) spatial-spectral plane. 75

Figure 34 Plots of the spectra indicated by the horizontal lines in Figure 33b, with peak location identified. 77

Figure 35 2D renderings of the chambered phantom: a) three primary pieces, b) fully assembled, and c) cut-away showing each of the 5 reservoirs. 79

Figure 36 The component comparison between corn oil and olive oil is very close, but the two solutions are not identical. 81

Figure 37 Relative placement and thickness of the 2D slice through the Chambered phantom is first viewed using a sagittal slice 82

Figure 38 Each solution chamber is clearly visible in the $\pi/2$, or purely spatial, projection. 85

Figure 39 In the 0 degree, or purely spectral, projection only spectral peaks are distinguishable. 86

Figure 40 The purely spatial projection image of the chambered phantom (a) with a vertical line indicating the location of the (b) spatial-spectral plane. 87

Figure 41 Plots of the spectra indicated by the horizontal lines in Figure 40b, with peak location identified. 89

Figure 42 A 3-dimensional surface rendering of the spatial-spatial-spectral volume obtained using the chambered phantom. 91

Figure 43 Susceptibility maps based on solutions in the chambered phantom for a) water and b) and corn oil. 93

Figure 44 Combined susceptibility maps. 95

Figure 45 The $\pi/2$, or purely spatial, projection appears to be a typical MRI acquisition. ... 99

Figure 46 The 0 degree, or purely spectral, projection only contains spectral peaks as a function of spatial position 99

Figure 47 The spatial-spatial plane at ~1.92 ppm has large signals from bone marrow. 101

Figure 48 The spatial-spatial plane at ~2.10 ppm has large signals from the fatty layer near the surface of the leg. 101

Figure 49 The spatial-spatial plane at ~5.09 ppm has large signals from the muscle tissue of the leg. 102
Figure 50 Three-dimensional rendering of the *in vivo* spatial-spatial-spectral data volume. 103
Figure 51 Water and RM solution spectra as measured by the clinical MRI system and an NMR spectrometer (signals normalized to single maximum). 107
Figure 52 FWHM measurements for the three primary spectral peaks in the 3Tubes spatial-spatial-spectral data volume. 109
Figure 53 Water peak FWHM measurements for a variety of back-projection angle offset and delta values. 112
Figure 54 Including fewer and fewer projection angles in the spatial-spectral back-projection procedure is obviously detrimental to final quality. 113
Figure 55 FWHM measurements for the three primary spectral peaks in the simulated spatial-spectral plane. 116
Figure 56 The simulated spatial-spectral plane quality degrades when including fewer and fewer projection angles in the back-projection procedure. 117
Figure 57 Class maps generated from data volumes reconstructed from a varying number of projection angles. 121
Figure 58 Class maps generated from data volumes reconstructed from a varying number of projection angles. 125
Figure 59 Class information can be gleaned from portions of many spectral planes. 129
Figure 60 Even from mildly corrupted data a class map can be created. 130
Figure 61 Spectral plane images extracted from the *in vivo* spatial-spatial-spectral volume and used in the classification procedure. 131
Figure 62 Even a very rudimentary classification procedure seems to be able to distinguish between major tissue types. 132
Figure 63 Dealing with a) an original dirac delta, each projection b) is also a dirac delta function, whereas the c) reconstruction is anything but. 143
Figure 64 A 21 sample Ram-Lak filter is a reasonable one to use to back out the back-projection PSF. 152
Figure 65 A basic Spin-Echo timing diagram (or pulse sequence). Use with permission [3]. 155

Table of Tables

Table	Page
Table 1 Acquisition bandwidths are determined by decimating the original sampling bandwidth.	61
Table 2 The spectral peaks of the 3Tubes solutions were measured on an NMR spectrometer.	69
Table 3 3Tubes acquisition parameters.	70
Table 4 Projection acquisition parameters associated with the 3Tubes phantom (for selected projections only).	72
Table 5 The spectral peaks of the chambered phantom solutions were measured on an NMR spectrometer.	80
Table 6 Chambered phantom acquisition parameters.	81
Table 7 Projection acquisition parameters associated with the chambered phantom.	83
Table 8 In vivo acquisition parameters.	96
Table 9 Projection acquisition parameters associated with the *in vivo* acquisition.	97
Table 10 NMR and MRI FWHM measurements for water and RM.	107
Table 11 Average calculated FWHM values using the 3Tubes data volume.	108
Table 12 Water peak FWHM measurements for a variety of back-projection angle offset and delta values.	111
Table 13 FWHM measurements for a variety of numbers of projection angle for each of the three spectral peaks in the simulations.	118
Table 14 3Tubes confusion matrix for 80 projection angles.	122
Table 15 3Tubes confusion matrix for 40 projection angles.	122
Table 16 3Tubes confusion matrix for 26 projection angles.	123
Table 17 3Tubes confusion matrix for 20 projection angles.	123
Table 18 3Tubes confusion matrix for 16 projection angles.	123
Table 19 Chambered phantom confusion matrix for 80 projection angles.	125

Table 20 Chambered phantom confusion matrix for 40 projection angles. 126
Table 21 Chambered phantom confusion matrix for 26 projection angles. 126
Table 22 Chambered phantom confusion matrix for 20 projection angles. 126
Table 23 Chambered phantom confusion matrix for 16 projection angles. 127
Table 24 Chambered phantom histogram segmentation classification scheme. 128
Table 25 *In vivo* histogram segmentation classification criteria. 131
Table 26 Acquisition parameters used for the 3Tubes phantom. 158
Table 27 Chambered phantom acquisition parameters. 161
Table 28 Acquisition parameters used during *in vivo* data collection 163

Table of Symbols

Symbol	Meaning
B_0	External magnetic field that surrounds objects being imaged by an MRI system.
B_1	Magnetic field used to rotate precessing magnetic moments.
BW	Sampling bandwidth.
$BW_{\pi/2}$	Purely spatial sampling bandwidth.
BW_0	Purely spectral sampling bandwidth.
FOV	Field-of-view used during imaging.
G_f	Frequency-encoding gradient.
G_ϕ	Phase-encoding gradient.
G_s	Slice selection gradient.
D	Spatial width of the sample being imaged.
d	Spatial position of a sample.
I	Electrical current.
L	Wire coil loop length.
M_0	Original net magnetization as aligned with the B_0 field.
M_z	Net magnetization along the z-axis.
M_{xy0}	Original net magnetization initially in the x-y-plane.
M_{xy}	Net magnetization in the x-y-plane.
N, M	Number of samples, or number of loops of wire in a coil.
$p(\theta,t)$	Projection as a function of angle, θ, and spatial position, t..
t	Time.
Δt	Change in time.
T_1	Spin-lattice relaxation time.
T_2	Spin-spin relaxation time.
$T_{2inhomo}$	Spin-spin relaxation due to B_0 inhomogenieties.
T_2^*	Effective spin-spin relaxation time.
V(t)	Voltage as a function of time.
x, y, z	Laboratory coordinate system axes.
x', y', z'	Rotating coordinate system axes.
γ	Gyromagnetic constant..
δ	Chemical shift, usually measured in parts per million (ppm).
μ_0	Permeability constant ($4\pi \times 10^{-7}$ Tm/A).
Ω	Spectral width of the sample being imaged.
θ	Angle at which projections are created for the Radon transform.

$\Delta\theta$.....Change in angle form one projection to the next.
$\Delta\phi$.....Change in magnetic flux.
ρ.....Spin-density.
ν.....Precessional, or Larmor, frequency.
ν_r.....Reference precessional frequency.
$\Delta\nu$.....Change in precessional, or Larmor, frequency.

Chapter 1

1. Introduction

As good as MRI is, it can be made better.

Magnetic resonance imaging (MRI) has been long established as an essential part of many clinical examinations, both as a diagnostic tool and as a post-treatment monitoring tool. MRI success is rooted in the uniqueness of the information that it provides and the relative ease with which it is provided. By providing high-resolution imagery of any portion of the human body, non-invasively, and without ionizing radiation, MRI provides invaluable information about the internal structures of the human body and allows medical personnel to distinguish between healthy and unhealthy forms of tissues.

Researchers have theorized that one of the most useful pieces of information that can be used to identify known and unknown tissues is the spectral signature of the tissue[1]. The spectral signature of a tissue is a set of data that describes the response of the tissue to specific frequencies of electromagnetic radiation. Unfortunately, current clinical MRI systems do not acquire spectral signatures. Instead, current clinical MRI systems integrate the spectral signature information into a single signal for each volume element, or voxel, within the imaging plane. In this way, current clinical MRI systems acquire images that are analogous to panchromatic remote sensing images.

This can be said because both imaging systems integrate frequency dependent signals together to create a single signal that is then used to create a single pixel in the final image. If the spectral information for each voxel in an object can be gathered through MRI acquisitions, each tissue would be distinguishable from others based on this spectral information. This type of tissue classification would be very similar to the material classification techniques employed for multi- and hyperspectral remote sensing systems. Because of this similarity, remote sensing classification techniques could be used to classify the tissues in the human body as these techniques have been studied, developed, and used with success for many years. Therefore, a short discussion of how spectral signature information is used in distinguishing between ground objects in multispectral aerial images is presented to explain the ways in which spectral information may increase the utility of MRI images.

When discussing remote sensing systems, the two system parameters that have the most influence on the system's ability to distinguish between ground-based targets are spatial resolution and spectral resolution. Understanding the former is relatively straightforward: the better the spatial resolution, the smaller the target that is resolvable in the resulting image. Fundamentally, the resolution of a remote sensing system is proportional to the size of the individual detectors of the system. Therefore, in general, the smaller the detectors, the better the resolution. Unfortunately, as detector size is reduced, the signal-to-noise ratio of the system is also reduced. The net result can be a very noisy image, if a usable one is produced at all.

[1] See for example references 5, 8, 9, 10, 12, 14, 16, 17, 20, 24, 30, 31, 34, 37

While spatial resolution is very important, spectral resolution can be just as important. Spectral resolution describes the ability of the imaging system to distinguish between different frequencies, or wavelengths, of electromagnetic radiation. In laymen's terms, spectral resolution describes how well the system is able to distinguish between various colors of light. The difference between two systems, one with low spectral resolution and one with high spectral resolution, is analogous to the difference between taking photographs with a camera that has been loaded with black & white film and another that has been loaded with color film. The primary distinction between these two systems is one system's ability to distinguish between sub-bands (i.e. red, green, and blue) within the *Visible* portion of the electromagnetic (EM) spectrum (see Figure 1) while the other integrates across those bands.

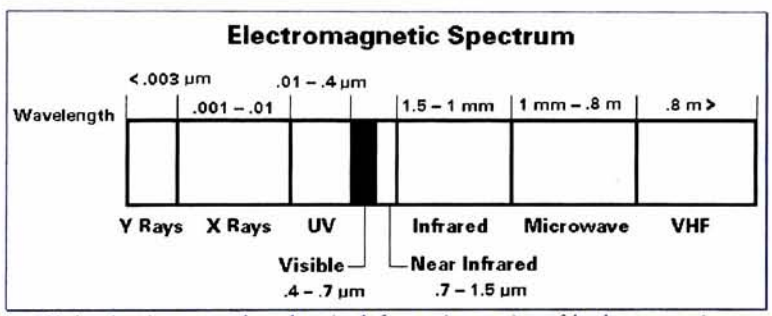

Figure 1 Various imaging systems depend on signals from various portions of the electromagnetic spectrum.

1.1 Motivation

The concept of spectral resolution is illustrated in a very common remote sensing example. Aerial imaging systems are able to acquire images that allow for camouflage detection (CD) even though, when viewed by a human, the camouflage appears to be identical to the vegetation that surrounds it. This is made possible by exploiting the fact that camouflage exhibits

a different spectral signature than vegetation in a part of the electromagnetic spectrum that humans cannot detect. Figure 2 depicts the spectral signature curves for vegetation and for a first generation camouflage. One can see that in the 0.4 to 0.7μm wavelength range, which is the general human sensitivity range, the two spectral signatures are virtually identical. This is important because early remote sensing systems tried to mimic the human visual system in order to ease exploitation of their resulting imagery products.

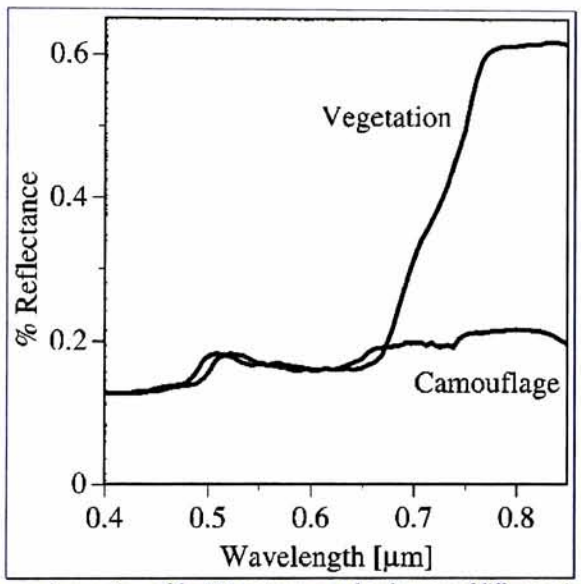

Figure 2 Acquiring imagery from various portions of the EM spectrum can take advantage of differences in spectral signature [2, page 25].

Eventually, remote-sensing systems evolved to take advantage of the difference in the spectral signatures exhibited in Figure 2. By acquiring imagery in the 0.7 to 0.9μm wavelength range, referred to as the near infrared (NIR) range of the EM spectrum, the process of CD became much easier. Figure 3 illustrates the CD problem and its solution. The image on the left represents an image as acquired using a panchromatic aerial imaging system. This system integrates EM energy across the *Visible* region of the EM spectrum to produce a greyscale image.

The image on the right was acquired by an aerial imaging system that takes advantage of the spectral signature differences in the NIR range of the EM spectrum. Display of this information is made possible by substituting the "green" image into the "blue" channel of the display; the "red" image into the "green" channel; and the "NIR" image into the "red" channel. With the proper information, displayed in a manner to expedite exploitation, the camouflaged areas become readily apparent even though the spatial resolution of the imaging system remains constant.

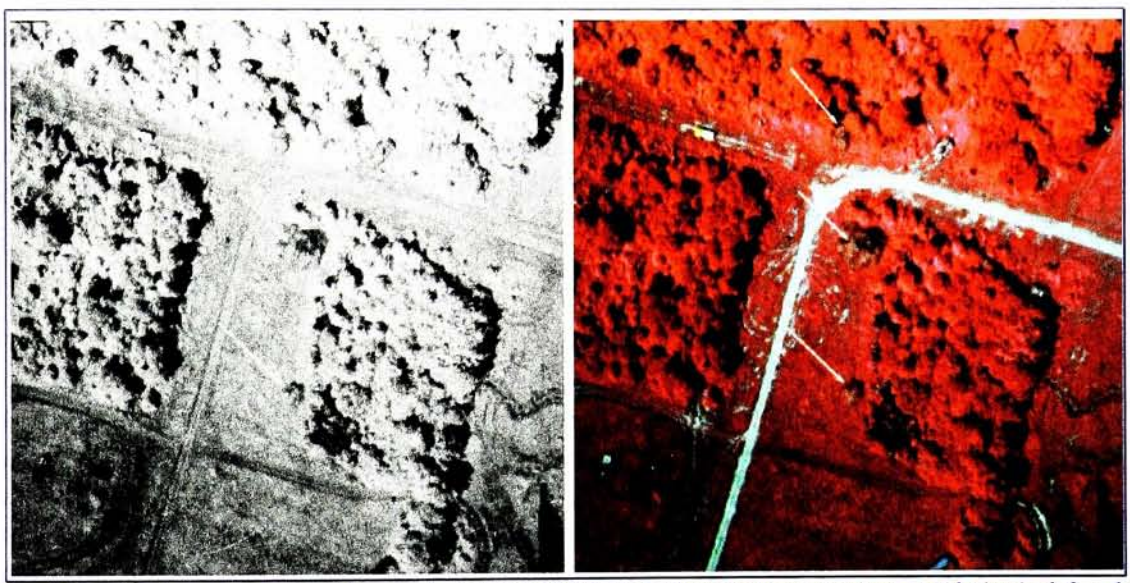

Figure 3 Camouflaged areas can go undetected in a panchromatic image (left), while they become apparent in an image created using signals from the NIR portion of the EM spectrum (right) Used with permission. [2, page 26 and color plate 2.5].

Just as vegetation and camouflage have unique spectral signatures, each tissue in the human body has a unique spectral signature. This is caused by the fact that each tissue is composed of a different combination of molecules, which are each made up of a different set, or arrangement, of atoms. Each of these differences could allow for tissue-type distinction, assuming that the information can be acquired and then properly utilized. Spatial-spatial-spectral

imaging will validate this assumption. By acquiring spectral signatures for each spatial location in an image, one will be able to acquire the tissue-unique spectral information needed to identify a particular spatial location as one tissue-type or another.

1.2 Goals

Several goals presented themselves during the course of this research. Here is a summary of those goals:

- Investigate the historical and contemporary methods of acquiring spatial-spatial-spectral information.
- Develop the theory for variable bandwidth spatial-spatial-spectral MRI and the parameters necessary for its implementation.
- Develop a protocol for use of the variable bandwidth spatial-spatial-spectral MRI technique.
- Demonstrate the variable bandwidth spatial-spatial-spectral MRI technique, and its associated protocol, as an applicable method for acquiring spatial-spatial-spectral data.
- Evaluate the performance of the variable bandwidth spatial-spatial-spectral MRI technique.
- Investigate the impacts of variations of the variable bandwidth spatial-spatial-spectral technique.
- Identify areas of potential improvement and for future study.

Each of these goals is addressed in one manner or another in the write-up to follow. Then, potential areas of improvement are discussed. But first, understanding MRI, chemical shift, spatial-spatial-spectral imaging, Radon transforms, and filtered back-projection are prerequisites for following the specifics of the variable bandwidth spatial-spatial-spectral imaging technique.

Chapter 2

2. Background

MRI image formation: some physics and some chemistry.

In order to give a complete understanding of the project being studied, a brief discussion of the physics of MRI and a simplified acquisition procedure will be presented. Then, a phenomenon that is usually considered an artifact in MRI, called chemical shift, will be discussed, as the project relies heavily on exploiting the side-effects of the phenomenon. Finally, MRI systems are being equipped with a piece of technology that is meant to mitigate the effects of chemical shift. This piece of technology, called variable bandwidth imaging, will be discussed as it pertains to chemical shift and the project.

2.1 MRI Image Formation

2.1.1 Larmor Frequency

Each nucleus in the atoms of the human body has a characteristic magnetic moment that is created by the atom's fundamental property of nature known as spin. Spin creates a tiny magnetic field resembling the magnetic field of a North-South bar magnet – the North end points in the direction of the magnetic moment [3]. Magnetic resonance imaging is made possible by placing the object that is to be imaged, usually some piece of human anatomy, inside a strong

magnetic field, referred to as the B_0 field. This has the effect of causing the magnetic moments of the atoms within the object to align with the B_0 field – the North ends of the magnetic moments line up with the North end of the B_0 field.

The rate at which magnetic moment precesses about the direction of B_0 is called the Larmor frequency, ν, and is influenced by the magnitude of the B_0 field. The Larmor frequency for each magnetic moment, for a given B_0 field strength, is also dependent upon the atom to which it belongs. For example, with a B_0 field of 1.0 Tesla (T) the Larmor frequency for ^1H is 42.58 x 10^6 Hz, while the Larmor frequency for ^{13}C is 10.71 x 10^6 Hz [7]. In fact, the Larmor frequency for each is described by equation 1, in which γ represents the chemical-dependent gyromagnetic ratio:

Equation 1 $$\nu = \gamma B_0$$

The Larmor frequency is important because it describes the frequency of both the energy required to manipulate the magnetic moment as well as the frequency at which the atom will emit a signal after the magnetic moment has been manipulated. One advantage to this situation is the fact that when imaging an object, particular atom types can be selected without disturbing others by applying and receiving the Larmor frequency appropriate for that particular atom type. This is useful because it allows for more control over the tissue content being imaged as different tissue types have a different make-up of atom types. For example, detecting signals at the 10.71 MHz Larmor frequency will result in images of tissues that contain ^{13}C, while detecting signals at 42.58 MHz will result in images of tissues that contain ^1H [3, 7, 11].

Now we know the frequency of the signal that will be emitted from objects and we can record the emitted signal such that we capture the signal from only the types of atoms in which we are interested. However, with what has been discussed so far, recording the signal after applying the B_0 field would result in one large signal with no physical location information. It would essentially give an idea of the relative amount of the particular atom type in the object, but no spatial distribution information about those atoms would be available. Therefore, additional procedures must be performed in order to relate the received signal to the physical location from whence it came.

2.1.2 Fourier Imaging

Most clinical MRI systems utilize an imaging technique called Fourier Imaging. This technique is used to gather the signals emitted from the object being imaged and then convert the collection of recorded signals to an image that represents the spatial distributions of structures in the slice being imaged. The conversion is performed through use of a Fourier transform (FT). In essence, frequency information is acquired and temporarily stored in an array referred to as k-space (see Figure 4). Once the full k-space set of data has been collected, it is transformed through a two-dimensional Fourier transform to create a spatial domain image. The tricky part is collecting the k-space data and storing it in the appropriate locations in k-space.

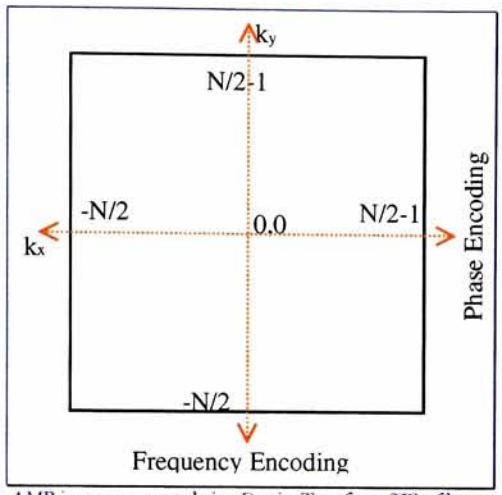

Figure 4 MR images are created via a Fourier Transform (FT) of k-space data.

In order to gather the k-space data required to create an accurate spatial domain image, three magnetic gradients are applied to the object. The three gradients (labeled G_s, G_f, and G_ϕ in Figure 5) are applied in directions that are orthogonal to one another. The slice selection gradient, G_s, is applied in order to limit the atoms from which signal is recorded to a finite spatial plane, or slice, through the object being imaged. The orientation of the slice will be perpendicular to the slice selection gradient. For example, using Figure 5 as a reference, if G_s is applied along the z-axis, the selected slice will be a plane that is parallel to the xy-plane[2]. The z-axis position of the slice will be determined by the interaction of the slice selection gradient and a radio frequency (RF) pulse that is applied concurrently. The RF pulse will be discussed in detail below.

[2] This does not necessarily have to be the case. With current clinical MRI systems, the slice being imaged can be oriented in any direction relative to the B_0 field, which is along the z-axis of the system. This is referred to as *oblique* imaging [3].

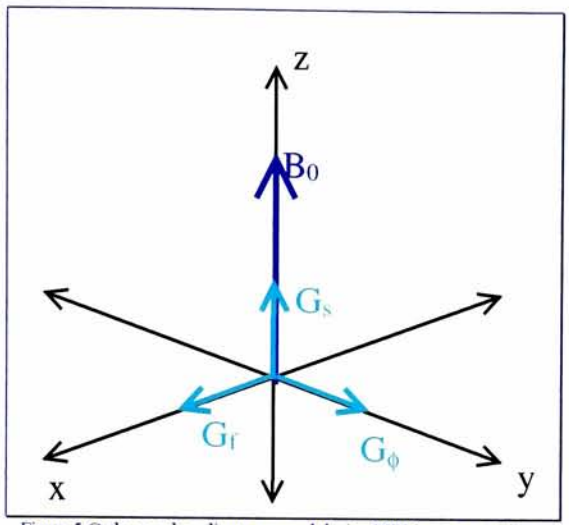

Figure 5 Orthogonal gradients are used during MRI image acquisition.

As signals are emitted from the slice being imaged, they are recorded and placed in the appropriate location in k-space. The appropriate k-space location for a particular signal is determined by *coding* the emitted signals. Signal coding is accomplished by using the other two gradients mentioned and equation 2.

Equation 2

$$\nu = \gamma(B_0 + dG)$$

The frequency-encoding gradient, G_f, is applied in order to place the emitted signals along *columns* in k-space. The frequency-encoding gradient will modify the Larmor frequency along the gradient direction as described by equation 2, with d representing the distance from the isocenter[3] along the gradient direction. Since the magnitude and direction of G_f will be known, the k-space location of particular frequencies will be easily predicted. When the emitted signal is received, it is relatively straightforward to place the particular frequencies contained in the signal in their

[3] The isocenter is the physical center of the MRI system. It is also the point where the net magnetic gradient, regardless of magnetic gradient amplitudes, is equal to B_0 [3].

appropriate k-space location. This is accomplished by Fourier transforming the received signal, as it is being recorded, and then placing the result in the appropriate column of k-space.

Unfortunately, the column to which the results of the Fourier transform belong will be ambiguous unless additional information is also acquired. The signal acquired to this point would effectively be a projection along constant frequency as determined by equation 2. A similar result would be arrived at if k-space were summed along constant values of k_x (see Figure 4). While this might prove useful in certain circumstances, it is not useful for Fourier imaging. For Fourier imaging, additional information is required.

By applying a short duration gradient, G_ϕ, in a direction that is orthogonal to both the slice selection and frequency-encoding gradients, a linear variation in phase can be imparted on the precessing magnetic moments along *rows* within k-space for the slice being imaged. The G_ϕ gradient is short because the precessional frequency of the magnetic moments need only change enough, as described by equation 2, to impart a phase shift relative to the other magnetic moments in the same row of the imaged slice. The phase shift provides a method for properly placing the Fourier transformed signals, which have been coded by G_f, into k-space.

2.1.3 Coordinate Systems

Now is a good time to explain the laboratory and rotating coordinate systems. As has been implied above, there is an implicit set of coordinates within the MRI system, where the B_0 field is along the +z-axis and the slice being imaged is a x-y-plane. This is referred to as the laboratory, or stationary, frame of reference. There is also a rotational frame of reference, whose

use will allow for an easier visualization and understanding of the signal production and recording systems, whose discussion will follow. The +z-axis of the rotating frame, as depicted in Figure 6, is coincident with the +z-axis of the laboratory frame. The x- and y-axes of the rotating frame of reference, however, rotate at the same rate as the spinning magnetic moments, which is, of course, the Larmor frequency. While the laboratory frame axes are labeled x, y, and z, the rotating frame axes are labeled x', y', and z.

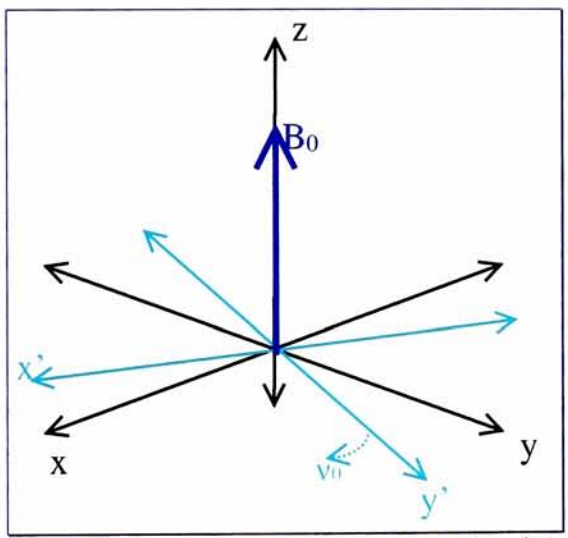

Figure 6 Two coordinate systems are used in MRI, one stationary (x, y, z) and one rotating at the Larmor frequency (x', y', z).

2.1.4 Signal Generation & Recording

We have discussed a method for assigning components of the recorded signal to particular k-space positions. Now we should discuss how the signal is generated and recorded. First, we should understand Ampere's Law and Faraday's Law. We have already relied upon Ampere's Law in our discussion as it tells us that we will generate a magnetic field, B, by applying an electrical current, I, to a coil of wire, where N is the number of loops of length L in the coil.

The magnitude of the magnetic field, B, is described by equation 3, in which μ_0 is the permeability constant, which has a value of $4\pi \times 10^{-7}$ Tm/A.

Equation 3

$$B = \mu_0 I \frac{N}{L}$$

Ampere's Law is put to good use to generate the B_0 magnetic field and the magnetic field gradients (G_s, G_f, and G_ϕ) used to select a slice to image and to relate the recorded signal to particular k-space positions. These gradients are generated by running currents, whose amplitudes are calculated by equation 3, through independent coils of wire.

Faraday's Law describes the theory of producing a time-dependent voltage, V(t), by applying a changing magnetic flux, $\Delta\phi$, to a coil with N loops of wire. Faraday's Law is the basic premise used for signal recording. The signal, when it is produced, will be recorded by two coils of wire, which have been wrapped around the x- and y-axes of the MRI machine. The basic idea is described by Faraday's Law, which is represented by equation 4.

Equation 4

$$V(t) = -N\left(\frac{\Delta\phi}{\Delta t}\right)$$

Two coils of wire are used in the recording system since a Fourier transform is used to place the frequency components in the recorded signal at particular positions in k-space. Unfortunately, the Fourier transform of a sinusoid, which is the most basic signal component, will produce two locations relative to the zero-point, or center of k-space. This creates an ambiguous

position for the signal component. To avoid positional ambiguity, two loops of wire are used to record the signal. By treating the signal recorded by one loop of wire as the real part of a complex signal and the other as the imaginary part, the resulting Fourier transform will provide an unambiguous k-space position for the signal. This signal-recording configuration is referred to as *quadrature* and is the preferred recording configuration for most clinical MRI systems.

Since it is a changing magnetic field flux that will cause a voltage in the coils of wire in the recording system and the magnetic moments in the slice are aligned with the B_0 field to this point in the discussion, there is no recordable signal, as of yet. Therefore, the net magnetic moments[4] need to be manipulated into producing a current in the recording system electronics. Applying a B_1 magnetic field performs manipulation of the magnetic moments in the object being imaged.

The purpose of the B_1 field is to rotate the net magnetic moments, M_0, in the imaging plane away from their equilibrium position of alignment with the B_0 field. The motivation behind this is that as M_0 is rotated away from alignment with the B_0 field, it starts to precess about the z-axis like a precessing, or wobbling, child's top (see Figure 7).

[4] When magnetic moments from many atoms in a localized spatial location act in a similar manner, the net magnetic moment is referred to as M_0.

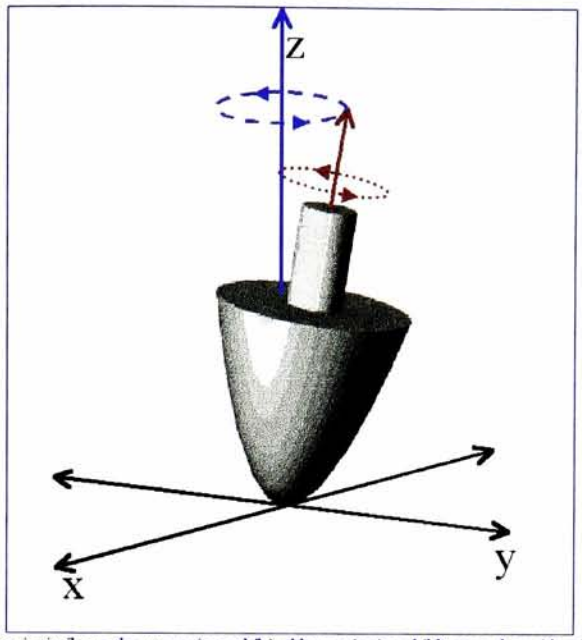

Figure 7 Magnetic moment precession is similar to the precession exhibited by a spinning child's top when either is pushed away from alignment with the original spin axis.

This precession, or movement, of the magnetic moment is what induces current in the recording system. As the rotated magnetic moment sweeps around the z-axis, the magnetic field flux induces an oscillating voltage in the coils of wire of the recording system. Extending this theory shows that a maximum amount of precession, and therefore a maximum voltage, would be created when the magnetic moment has been rotated to a position that is orthogonal to the B_0 field. In other words, rotating the precessing magnetic moment down to the x-y, or transverse, plane would create the largest signal in the recording system. The M_0 rotation angle is controlled by the duration of time, τ, that the B_1 field is applied. In particular, the rotation angle, θ, is calculated as in equation 5.

Equation 5

$$\theta = 2\pi\tau B_1\gamma$$

The B_1 field is a magnetic field created by a system of wires that have been looped around the x-axis of the MRI machine. These loops are a separate set of loops from those in the recording system. By running a current through these loops of wire, another magnetic field, the B_1 field, is created. The tricky part about this is the fact that since M_0 is precessing about the +z-axis, applying a constant current would not produce the desired affect of rotating M_0 down to the x-y-plane. In order to obtain the desired affect, an alternating current is applied to the loops of wire, which produces an alternating B_1 field. When viewed in the laboratory frame of reference M_0 will essentially spiral down to the x-y-plane, but when viewed in the rotating frame of reference, as in Figure 8, M_0 rotates directly down to the x'-y'-plane.

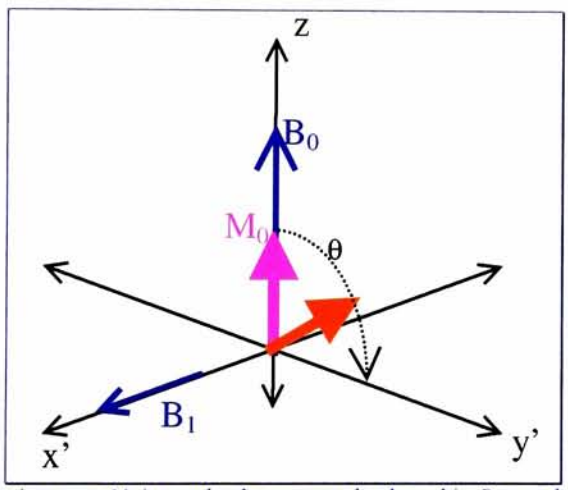

Figure 8 The net magnetic moment, M_0, is rotated to the transverse plane by applying B_1 to produce a recordable signal.

Once M_0 has been rotated down to the transverse plane, the precessing magnetic moment will produce a voltage change in the receiving loops of wire that have been wrapped around the x- and y- axes of the MRI system. The recorded signals are then fed into the signal-processing portion of the MRI system.

2.1.5 Timing Diagram

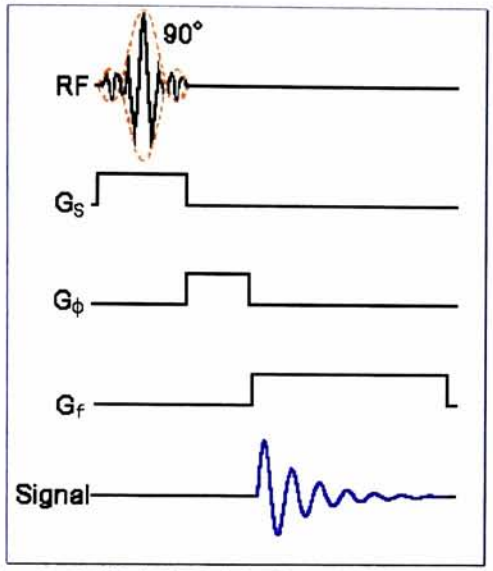

Figure 9 A simplified 90°-FID timing diagram (or pulse sequence) [3].

At this point, it would be helpful to explain the relative timing of the various gradients, the B_1-producing RF signal, and the subsequent signal. Figure 9 depicts a sketch of the relative timing of these events for a simplified version of an imaging sequence, which is referred to as the 90°-FID sequence[5]. The first step in the procedure, one that is not depicted in Figure 9, is to place the object to be imaged into the B_0 field. This is accomplished in a clinical setting by placing the patient inside the bore of the MRI machine, whose B_0 field is continuously resident. The next procedure in the imaging sequence is the concurrent application of the slice selection gradient, G_s, and the B_1-producing radio-frequency pulse. The effects of G_s on the Larmor frequencies can be calculated through use of equation 2.

The top line of Figure 9, which is the RF application timing line, indicates that the pulse shape is a truncated sinc function [37]. The reason for this shape is to ensure that the slice to be

imaged has sharply defined surfaces when combined with the G_s application. If the RF pulse were shaped like a rect function, then the slice profile would be sinc-shaped because the frequency content of a rect-shaped pulse is sinc-shaped. Conversely, the frequency content of a sinc-shaped pulse will be rect-shaped. By applying this logic, use of a sinc-shaped pulse will result in definitive cutoff frequencies and therefore definitive surfaces for the imaging plane.

Once the slice selection gradient and the RF pulse have been applied and then discontinued, causing the net magnetic moment to rotate down onto the transverse plane, the phase encoding gradient, G_ϕ, is applied. As was discussed above, the phase encoding gradient need only be applied for a short duration, as the objective is to impart a distinguishable phase shift in the precessing magnetic moments from various locations along the phase-encoding direction. The resulting phase shift is linear with respect to the physical location of the moments within a row in the slice being imaged.

Finally, the frequency-encoding gradient, G_f, is applied while the emitted signal is recorded. As was also discussed above, applying G_f has the affect of coding the received signal such that individual components of the signal can be correlated to physical positions within columns of the slice being imaged.

While Figure 9 depicts a simplified version of the 90°-FID sequence, it only depicts the sequence used to construct one column of k-space. The only way to acquire the data to fill the rest of k-space is to apply the imaging sequence depicted in Figure 9 once for each column in k-

[5] FID is an acronym for Free Induction Decay, which refers to the characteristic signal emitted and received during MRI imaging.

space; each with a different G_ϕ amplitude. The reason for this is that in order to form an accurate two-dimensional image, a complex two-dimensional Fourier "image" must first be constructed. The Fourier image is the k-space representation of the recorded signals. In other words, in order to reconstruct a 256x256 image of the slice of interest, the 90°-FID sequence as depicted in Figure 9 would have to be applied 256 times with 256 different G_ϕ amplitudes. This will completely fill the k-space image, which will then be Fourier transformed to produce a spatial domain representation of the slice being imaged. While it is true that other methods for filling k-space have been studied [23], the fact remains that a Fourier Transform is most often used to create the spatial domain representation of the slice being imaged.

2.1.6 Signal Decay

An observation that one could make from Figure 9 is that the bottom row in the timing diagram depicts the FID signal as a decaying signal. Although the figure has been greatly simplified, this aspect of the timing diagram is not altogether incorrect. After each application of the B_1 field, and subsequent signal recording, the signal will decay away to levels too low to be recorded. The signal decay is caused by two primary factors: spin-lattice relaxation, and spin-spin relaxation.

If you'll recall, in order to produce the recordable signal, the net magnetic moment was rotated away from alignment with the B_0 field through application of the B_1 field along the x-axis. Also recall that it was stated, and depicted in the timing diagram, that the B_1 field is applied for a finite duration – the duration required to rotate the magnetic moment down to the transverse

plane. Imagine, if you will, the situation at this point in the timing sequence: there is a large magnetic field, B_0; the magnetic moment has been forced out of alignment with that large magnetic field; and the force that caused the magnetic moment out of alignment has been taken away. It is completely logical to conclude that the magnetic moment will attempt to realign itself with the large magnetic field. That is precisely what happens, but it doesn't happen instantaneously.

Just as it takes time to rotate the net magnetic moment away from alignment with the B_0 field (t of equation 5), it takes time for the magnetic moment to realign with the B_0 field. The rate at which individual magnetic moments realign with the B_0 field is dependent upon the atoms, molecules, and tissues to which the moments belong. The parameter that describes the rate at which the realignment occurs is called the spin-lattice relaxation time, T_1. Assuming the net magnetic moment amplitude before B_1 application is represented by M_0 and M_z represents the amount of M_0 that has realigned with B_0 at any given time, t, then equation 6 describes how the spin-lattice relaxation time fits into the realignment relationship.[6]

Equation 6

$$M_z = M_0\left(1 - e^{-t/T_1}\right)$$

Plotting M_z as a function of time, τ, for an arbitrary M_0 and T_1, results in a graph similar to that depicted in Figure 10. Keep in mind that T_1 is dependent upon many factors, not least of

[6] M_z is also referred to as the longitudinal magenetization as it is aligned with the z-axis when in a state of equilibrium.

which is the type of atoms being imaged, the tissue to which the atoms belong, and the strength of the external magnetic field, B_0.

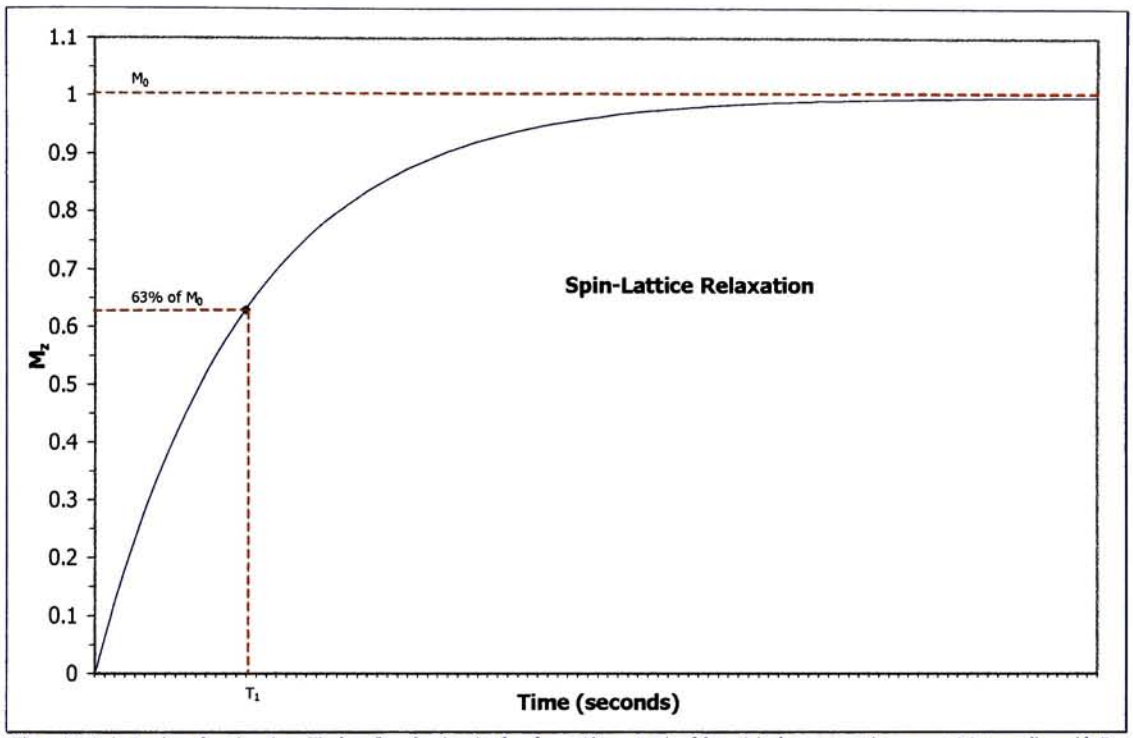

Figure 10 Spin-Lattice relaxation time, T_1, describes the time it takes for ~63%, or 1-e^{-1}, of the original net magnetic moment M_0, to realign with B_0.

In addition to spin-lattice relaxation, there is another relaxation time that must be considered when designing protocols for MRI imaging. That relaxation time is called spin-spin relaxation time, T_2. Spin-spin relaxation is a signal decay that is not as intuitively obvious as spin-lattice relaxation. One should remember that although the net magnetic moment seems to be stationary in the rotating coordinate system after rotation down to the transverse plane, it is actually precessing at the Larmor frequency when viewed in the laboratory coordinate system. Remember, too, that the net magnetization is actually the compilation of individual magnetic moments that act very similarly and are in close physical proximity to one another. Spin-spin

relaxation is caused by the fact that the individual magnetic moments begin to precess at slightly different rates; each with its own Larmor frequency – some faster, some slower. As the precessing magnetic moments spread out, the net magnetic moment is said to *dephase.* This dephasing causes degradation to the net magnetic moment, as is depicted in Figure 11.

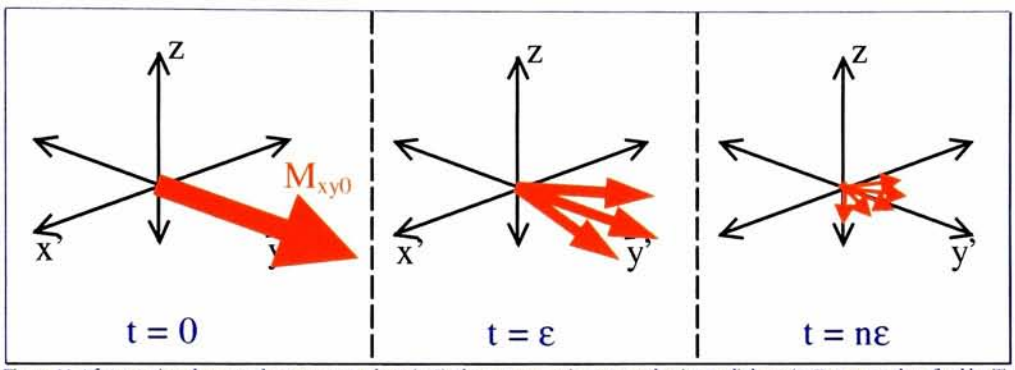

Figure 11 After rotation down to the transverse plane (t=0), the net magnetic moment begins to diphase (t>0) at a rate described by T_2.

Assuming the net magnetic moment amplitude in the transverse plane after B_1 application is represented by M_{xy0} and M_{xy} represents the amount of M_{xy0} that remains at any given time, t, then equation 7 describes how the spin-spin relaxation time fits into the dephasing relationship.[7]

Equation 7

$$M_{xy} = M_{xy0} e^{-t/T_2}$$

Plotting M_{xy} as a function of time, τ, for an arbitrary M_{xy0} and T_2 results in a graph similar to that depicted in Figure 12. Keep in mind that T_2 is dependent upon many factors, including the type of atoms being imaged, the tissue to which the atoms belong, and the strength of the external magnetic field, B_0. It is also worth pointing out that T_2 is always shorter than T_1. That is to say that spin-spin relaxation always takes less time than spin-lattice relaxation.

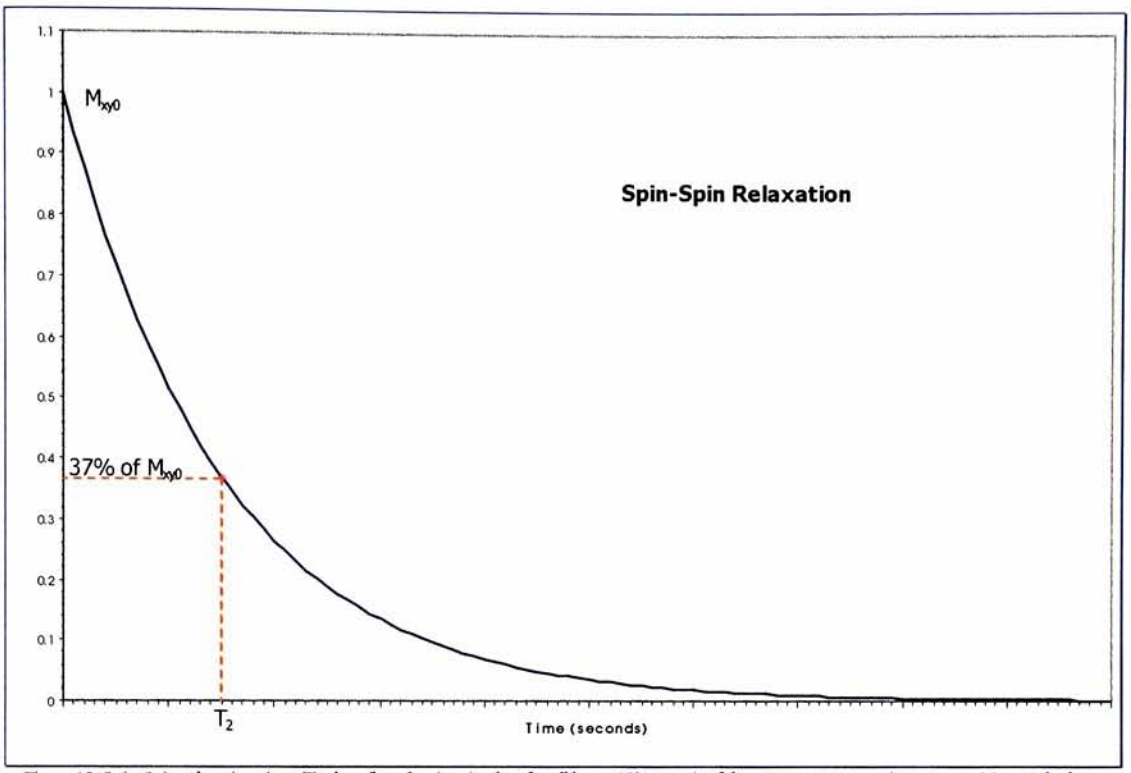

Figure 12 Spin-Spin relaxation time, T_2, describes the time it takes for all but ~37%, or e^{-1}, of the transverse magnetic moment, M_{xy}, to dephase.

There are two factors that cause the individual magnetic moments to precesses at slightly different rates – the root of spin-spin relaxation. The first factor, T_2, is due to molecular interactions and is said to be a pure T_2 relaxation [3]. The second, $T_{2inhomo}$, is due to inhomogeneities in the B_0 magnetic field and is therefore system dependent. These two interactions combine to produce an overall spin-spin relaxation time, T_2^*, as in equation 8.

Equation 8

$$\frac{1}{T_2^*} = \frac{1}{T_2} + \frac{1}{T_{2\text{inhomo}}}$$

[7] M_{xy} is also referred to as the transverse magenetization as it is rotated away from the z-axis down to the x'-y' plane.

When referring to spin-spin relaxation, most people refer to T_2, but are really referring to T_2^* as even systems with the most uniform B_0 fields likely have at least a small $T_{2inhomo}$ contributor.

2.2 Chemical Shift Artifact

One of the primary assumptions made while acquiring MR images is that the localized magnetic field in the environment surrounding the precessing magnetic moments will be homogeneous. The reason for this assumption is that the Fourier imaging theory, upon which MRI is based, assumes that the only variation in precessional frequency observed in the recorded signal is caused by the imaging gradient, which is predictable as described by equation 2. This permits signals of specific frequencies to be spatially positioned based on the difference between their frequency and that of the same atom located at the isocenter. In reality, however, many factors can influence the magnetic field of the environment surrounding the atom being imaged. For example, the electron clouds around nuclei create a small magnetic field that can oppose the applied B_0 field. Because the density of electron clouds is spatially varying within the molecule, the magnetic field experienced by any particular atom will vary depending on its location in the molecule. Based on this description, one can gather that the amount of change in the localized magnetic field is probably based, at least partly, on the molecular make-up of the localized environment. In fact, this is true.

One of the side effects of a non-uniform localized magnetic field is that each individual type of molecule has a characteristic spectral signature. The spectral signature is dependent upon the B_0 field strength, but is also dependent upon the atomic make-up of the molecule. Extending

this principle to collections of molecules and eventually to tissue types, one could argue that particular tissue types would exhibit a particular spectral signature due to localized magnetic field inhomogenieties caused by the molecular make-up of those tissues. Referring back to the analogy between MR imaging and aerial imaging, if spectral signatures can be collected, then they might be exploited to identify the tissue from whence they came. To that end, understanding the cause and the way in which current MRI systems deal with the spectral information will be helpful in understanding the spatial-spatial-spectral imaging technique discussed later.

2.2.1 Cause of Chemical Shift

The root cause of the spectral signatures is called chemical shift, which is usually denoted by δ. The basic concept of chemical shift refers to the fact that magnetic moments of particular chemicals and molecules will resonate at a slightly different frequency, ν, than that of a reference proton, ν_r, when placed in the same B_0 field [7, 11]. The chemical shift of a particular molecule, or tissue type, is specified in parts-per-million relative to the reference frequency and is calculated via equation 9.

Equation 9

$$\delta = \frac{(\nu - \nu_r) \times 10^6}{\nu_r}$$

Typically, the chemical shift of a particular atom type is specified for the atom's Larmor frequency relative to the Larmor frequency of tetramethylsilane (TMS)[8]. However, the human body does not naturally contain TMS, so when using MRI systems to image the human body

chemical shift is calculated for one tissue's Larmor frequency relative to another tissue's Larmor frequency. For example, biological fat protons (CH_2) display a chemical shift of approximately 3.45 ppm with respect to water protons (H_20) [7]. When imaged in an MRI machine with a B_0 field of 1.5T, that amount of chemical shift results in a difference in Larmor frequency, $\Delta\nu$, of about 220Hz, as calculated by equation 10.

Equation 10

$$\Delta\nu = \frac{\delta\gamma B_0}{1x10^6}$$

2.2.2 Effects of Chemical Shift

Since a Fourier transform is used to spatially position particular frequency components of the recorded signal, changes in the frequency can cause the signal components to be misplaced. Making a quick estimate of the Larmor frequency, via equation 2, shows that it is approximately 63.87 MHz on a 1.5T MRI system for ^1H atoms. While a 220Hz frequency shift seems insignificant relative to such a large Larmor frequency, imagine the scenario in which an MRI image of 512x512 pixels is acquired for a field-of-view (FOV) of 24cm. This FOV and number of pixels translate to 0.47 mm/pixel in the final image. Suppose that within that 24cm FOV there is a particular voxel whose tissue contains both water and fat. A frequency-encoding gradient value for this scenario could be 0.15 G/cm, or $1.5x10^{-5}$ T/cm. Plugging these values into equation 2 shows that the chemical shift between the fat and water protons would separate the signals from these two tissue components by approximately 3.44 mm, or more than 7 pixels.

[8] Tetramethylsilane ($Si(CH_3)_4$) is used as it is extremely stable and relatively easily available.

Because the effects of chemical shift are misrepresentative of the actual phenomena of the object being imaged, those effects are referred to as an artifact, called chemical shift artifact. In the scenario described, it would likely be very difficult to determine that an artifact is present in the resulting imagery. An easier situation in which to detect the artifact is one in which water and fat are physically adjacent to one another, but the imagery shows that they are separated.

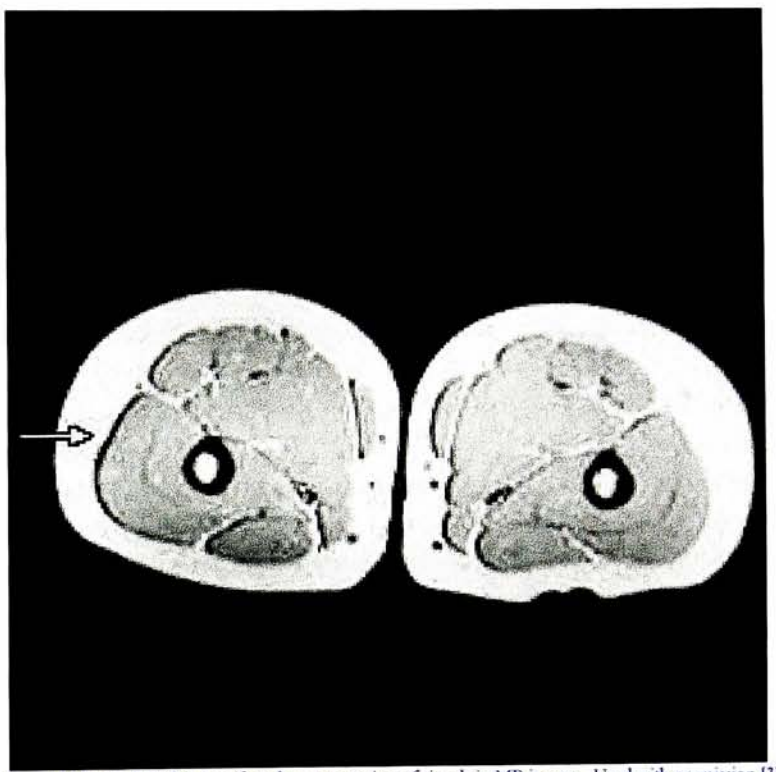

Figure 13 Chemical shift is manifested as a separation of signals in MR images. Used with permission [3].

Figure 13 depicts an axial slice though a patient's legs in which a chemical shift artifact appears between the fat and muscle tissue (see arrow). It is fairly obvious that there is not a physical separation between the fat and muscle in this patient's legs as is depicted in the image.

And, even if there were, it is likely that the separation would be exhibited at all interfaces between the tissues, which is clearly not depicted in the image.

2.2.3 Variable Bandwidth

One way in which chemical shift artifacting is mitigated is through a reduction in the number of pixels in the MRI acquisition, and therefore in the final image. The idea is to limit the chemical shift artifact to a spatial area that is less than a pixel and therefore it will not be exhibited in the final imagery. The obvious drawback to this technique is that the final imagery will have fewer pixels and therefore less resolution – something that MRI researchers have been fighting to increase since the inception of MRI. A similar method of reducing chemical shift is to increase the frequency-encoding gradient amplitude. Increasing the frequency-encoding gradient amplitude will impart more of a frequency difference between spatial locations, thereby reducing the chemical shift impact on the imagery. This has the negative effect of reducing the field of view, however, as well as potentially reducing the signal-to-noise ratio of the recorded signal.

In recent MR imaging systems, chemical shift is avoided through judicious use of sampling rate. During the receive portion of image acquisition procedures, the voltages induced in the x- and y-axis coils by the emitted signal is recorded. As part of the recording step, the analogue voltages are converted to digital amplitudes by using an analog-to-digital (A/D) converter. Current clinical MRI systems employ an A/D converter that will sample the emitted signals such that the chemical shift artifact is virtually eliminated. Elimination of the artifact is ensured by making sure that each pixel in the final image is composed of a wide range of

frequencies relative to chemical shift ranges. This will become clearer after a more detailed explanation of the A/D converter and sampling bandwidth.

The A/D converter samples the emitted signal in the time direction and quantizes the signal in the amplitude direction. The *bit depth* of the A/D converter controls amplitude quantization. Contemporary MRI systems typically use an A/D converter with a bit depth of 16, which allows for 2^{16}, or 65536, individual amplitude levels. By allowing such a wide range of amplitude levels, current clinical MRI systems are able to distinguish between very subtle changes in signal intensity, as well as between wide swings in intensity, both at the same time.

The time direction sampling is controlled by the *bandwidth* of the A/D converter. The bandwidth of the A/D converter describes how often the emitted signal is sampled. As with any sampling situation, the more samples used, the more accurately the input signal is represented by those samples. This is the essence of the Nyquist sampling theory, which states that the maximum frequency that can be accurately represented by a sampled signal is at most two times the inverse of the sampling rate [37]. For example, the maximum signal frequency that can be accurately represented by a linear sampling bandwidth of 10Hz (cycles/second) is 5Hz.

In addition to the A/D sampling, clinical MRI systems employ a secondary sampling scheme. This sampling scheme is used to reduce the number of samples down to a more manageable, and displayable, size such as 256 or 512. Therefore, no matter what the original A/D sampling bandwidth, the final image will have only 256 or 512 samples. This means that each pixel in the final image is composed of the samples across a wide range of frequencies in the A/D

quantized signal, depending on the original A/D converter bandwidth. For example, if the originally received signal is sampled at 30kHz and the output image size is to be 512 pixels wide, then each pixel's final signal will be an integration of the signal across 30kHz / 512Hz = 59Hz. This is important when dealing with the chemical shift artifact because the spectral width of the signal from any individual voxel can be up to 220Hz, if that voxel contains both water and fat and we are using a 1.5T MRI system. This results in a separation of approximately 3.75 pixels between the water and the fat in the same voxel. By sampling over a range of 128kHz, the chemical shift separation can be reduced to less than one pixel (0.88 p), which would be undetectable in the resulting imagery. Likewise, sampling a 64kHz bandwidth with 256 samples would result in an undetectable chemical shift artifact of 0.88 pixels. This would result, however, in a reduction in spatial resolution as well, which often not desirable.

Following this logic, using as high a bandwidth as the A/D converter will allow is desirable in order to get the most accurate rendition of the input signal and to reduce the impacts of chemical shift. The drawback to this is the fact that as more and more A/D samples are used, the width of each is reduced accordingly. In an ideal situation this would not be problematic, but in the real world very narrow sample sizes can negatively affect signal-to-noise. In other words, as the sampling bandwidth increases, the signal-to-noise of the quantized signal is likely to decrease. This can impact the ability of the sampled signal to accurately represent the original signal. Moreover, in an imaging system that is already susceptible to signal-to-noise issues, such as MRI, this can become a limiting factor in choosing the sampling bandwidth to be used.

Unfortunately, the highest available sampling rate cannot be used effectively in every imaging situation due to the impact on signal-to-noise. Therefore, current clinical MRI systems are equipped with a variable bandwidth A/D converter. By manipulating the sampling bandwidth, a MRI system can optimize the trade-off between chemical shift and signal-to-noise. Since this can be very complicated and time consuming, most clinical MRI systems perform this trade-off automatically, while allowing the operator nearly complete control if it is needed. The word "nearly" was included in the last sentence because the available sampling bandwidths are not arbitrary. Typically, they are determined by dividing the maximum possible bandwidth of the A/D converter by integer values, which results in very particular bandwidths. This is unimportant for most clinical imaging situations, but has a significant impact on spatial-spatial-spectral imaging, as will be discussed later.

2.3 Magnetic Resonance Spectroscopy

Despite the artifacts associated with chemical shift, clinical magnetic resonance systems have been used to acquire tissue spectra in recent years. The procedures used for this sort of acquisition have been categorized as magnetic resonance spectroscopy (MRS). MRS has been the subject of study for several years. The objective of most of the MRS work to date is to quantitatively identify particular metabolites that are present within the human body [10, 12, 14, 16, 17]. Figure 14 depicts a detailed spectrum of a rat's brain acquired via high-resolution NMR (top), and a spectrum as acquired via MRS (bottom). The labels in the top spectra of Figure 14 indicate individual chemical compounds or metabolites. By acquiring the spectrum of physical

positions, or voxels, within the human body, the relative amounts of particular chemical compounds can be evaluated, as depicted in the figure. The chemical composition of the voxels is then used to identify particular metabolites present, which lead to knowledge about the biological processes present in that voxel.

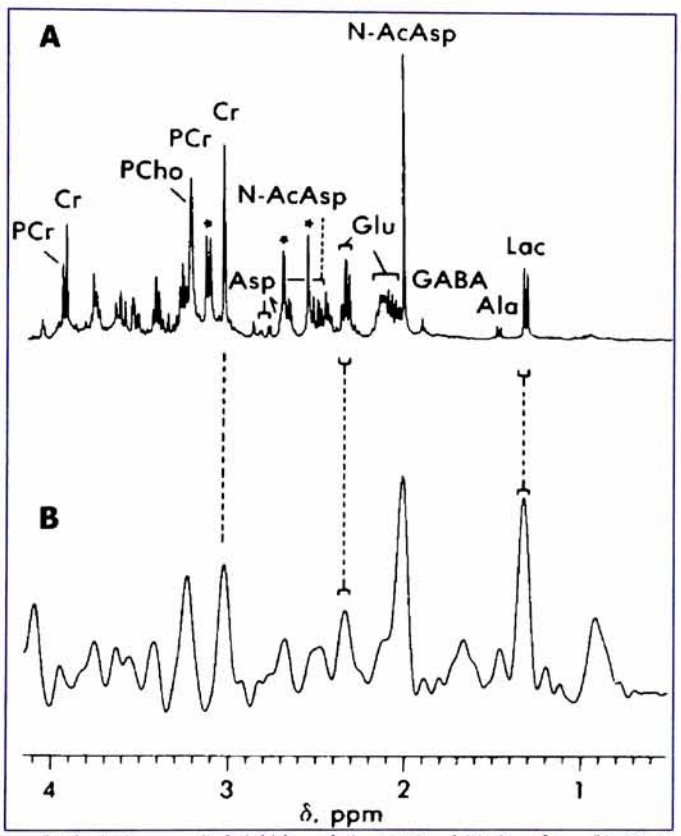

Figure 14 (A) ^{1}H spectrum of rat brain tissue acquired via high-resolution NMR and (B) via surface coil MRS. Used with permission [16].

Identification of metabolites, and therefore the biological processes present, is not the only use for MRS. The other use for spectral information is to identify tissue types, or at least distinguish tissue types from one another. There have been researchers [14, 15] who believe that each tissue type exhibits a unique spectrum due to the unique chemical arrangement and composition of the tissue type. Extending this theory to include pathological tissue types is an

easy step. If it can be determined that pathology exhibit unique spectral characteristics, then acquiring spectral data might allow for the identification of the pathology. Indeed, pathology detection might well become an automated process.

The first of many obstacles in the path of spectroscopic imaging is the need for very homogeneous magnetic fields. Subtle changes in the local magnetic field can disrupt the Larmor frequencies of metabolites enough to shift their nominal positions in the spectrum. Even the relatively low-magnitude eddy currents of an MRI system, created by switching gradients on and off, are often enough to render the acquired spectrum unusable. There are two ways around this obstacle. The first is to create and maintain a homogeneous magnetic field. As this is limited by the technological maturity of the magnetic field gradient architecture, it is a difficult path around the obstacle. The other way around the obstacle is to limit the physical area from which signals are recorded. This path is accomplished through techniques referred to as localization.

2.3.1 Localization

Although localization technique development seems to have become a research topic of its own, the prominent techniques can be grouped into four categories: surface coil methods, surface coil B_1 gradient methods, B_0-gradient methods, and slice-selective B_0 gradient methods [13]. Rather than present a dissertation on the various methods of localization, it is sufficient to note that their shared goal is to create a localized homogeneous magnetic field to allow for accurate spectra acquisitions. Then, the localized area from which the spectrum is acquired is shifted to a new physical location where the next spectrum is acquired. This process is repeated

until the area, or volume, over which spectral information is desired, has been sampled. One of the major drawbacks to localization methods is the extremely long imaging times required to perform the localization steps, acquire the spectral data, and then repeat the process. Because of this drawback, spectral acquisitions are typically limited to very small physical regions of the object being imaged.

Another reason to acquire a localized spectrum, rather than attempting to gather the spectra of a full slice is to avoid the effects of noise or inaccuracies due to motion. By relying on Fourier transform processing to convert k-space data to spatial images, acquired noise can have very detrimental effects. Since each pixel in k-space influences all pixels in the spatial domain even very low levels of noise in k-space can create inaccuracies in the spatial image. For example, noise in high frequencies, which are represented by the outer values in k-space, can cause blurring or ringing near the edges of structures in the spatial domain. Now, consider using the Fourier transform to create spectra. As spectra are composed almost exclusively of edges, having noise in the acquired signals could have serious repercussions. Therefore, avoiding Fourier transforms to create spatial domain representations of spectra as much as possible will eliminate the possibility of errors induced by noise.

2.3.2 Phase-Encoding Imaging

The alternative to using localization techniques to limit the area from which signals are acquired is to use a phase-encoding technique to code the signal from individual locations [8, 9, 13]. The process used for phase-encoded spectroscopic imaging (SI) is very similar to that of

magnetic resonance imaging. The primary difference is that the frequency-encoding read-out gradient used in MRI protocols is not used in SI protocols. As has been discussed, the frequency-encoding gradient is used in MRI protocols to induce a frequency shift in the signal emitted by protons in the object being imaged. The amount of frequency shift is directly related to the physical location of the magnetic moments, as depicted in equation 2. Since SI is attempting to resolve the frequency shift induced by chemical components within a single location, adding a frequency-encoding gradient would only serve to confuse the Fourier transform used in the image reconstruction process. To avoid using a frequency-encoding gradient, SI simply employs a second phase-encoding gradient to determine a received signal's physical position. Once the phase-encoding gradients have been set for a particular location, the FID signal from that location is acquired and then Fourier transformed to create the spectrum for that location.

Unfortunately, to accurately position the FID signal within the object being imaged, the number of phase-encoding levels required increases to the total number of pixels that will be present in the final image. For example, if the final output image is to be 256x256 pixels in size, then there will have to be 256x256=65536 phase-encoding steps – 256 levels in one direction for each of the 256 levels in the orthogonal direction. This implies that the imaging protocol would have to be performed 65536 times. As limiting as this may seem, SI has some significant advantages over the techniques that rely on localization. To begin with, *a priori* knowledge of the region of interest imaged by SI is not needed to the degree as for localization due to the phase encoding used. In addition, the collection efficiency for SI is much higher than for the localization methods. Although the SI protocol is repeated a large number of times, it is still more

efficient than repositioning through localization. Finally, the information that results from SI can be displayed as position-dependent spectra as well as images, just as MRI data is displayed. On the other hand, SI does have some disadvantages. Chief among them is the fact that volumes are not well defined and metabolite quantitation is difficult [10, 14, 17].

2.4 Radon Transform

One of the most important tools used in medical imaging is the Radon transform. The Radon transform is so important because it allows one to gather information about the interior structure of an object and then reconstruct that information into a representation of that structure without dissecting the object. In fact, the Radon transform is such an important tool its use is not limited to medical imaging modalities. For example, the transform has been used in synthetic aperture radar (SAR) remote sensing systems to allow the systems to gather Earth surface information from aerial- or space-based platforms and then to reconstruct a representation of the Earth's surface via the inverse Radon transform [43, 44].

The most prevalent use of the Radon transform is in X-Ray computed tomography (CT). In a nutshell, X-Ray CT uses X-Ray energy to gather tissue attenuation information through portions of the human body and then the inverse Radon transform to reconstruct a spatial-spatial map of that attenuation.

2.4.1 Example Scenario

Although the Radon transform can, and will, be described via mathematical formulae, an example simulation scenario will be used to assist in understanding the theory and application of the Radon transform. The scenario starts with a three dimensional object. This object is depicted in Figure 15. In an effort to keep the results interesting and easier to follow, the object is the composite of three other objects: two spheres and a rectangular box. As can be seen from Figure 15, the individual objects overlap spatially, which is a physical impossibility, but can be very helpful for demonstrative purposes.

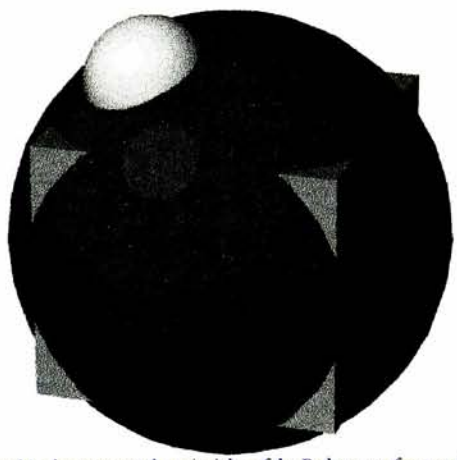

Figure 15 An example object used to demonstrate the principles of the Radon transform and its inverse: the backprojection.

The Radon transform is easiest to understand when dealing with two-dimensional objects, or slices through three-dimensional objects. Therefore, a slice will be cut from the object of Figure 15. The orientation of the slice will be along the diagonal of the box object, as depicted by the blue plan of Figure 16. Figure 17 represents the two-dimensional slice through the object that will be used to demonstrate the Radon Transform. Each grey level in Figure 17 represents a unique tissue type, with black representing the area outside the object.

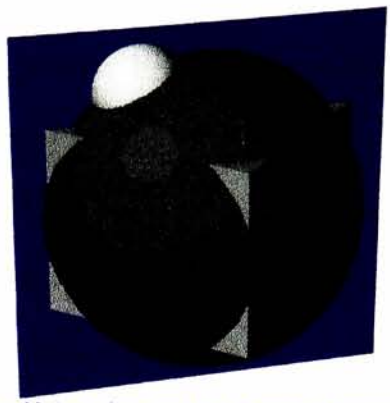

Figure 16 An imaging plane (blue) was chosen such that all aspects of the example object were included..

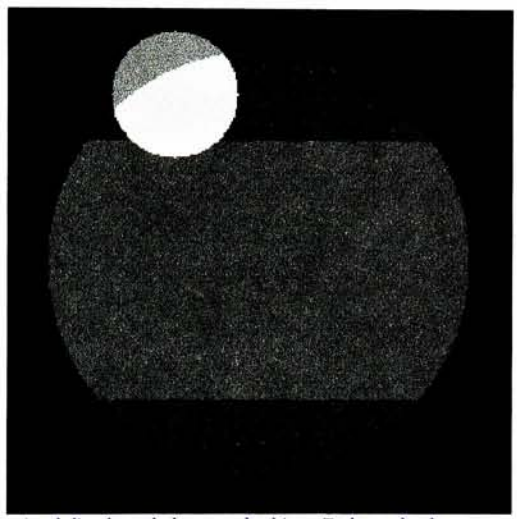

Figure 17 Two dimensional slice through the example object. Each grey level represents a unique tissue type.

Strictly speaking the Radon transform is simply another way in which to represent an object. It is similar, in many respects, to the Fourier transform in that the Fourier representation of an object is simply another representation of that object. Also like the Fourier transform, the information held in Radon space can be inverse transformed to recreate the original spatial representation of the object. The inverse Radon transform can be performed by back-projection.

2.4.2 Data Transformation

The Radon transform can be thought of as a series of projections through the 2D object. Imagine the entire signal in a spatial image, Figure 17 for example, being projected onto a 1D axis, the position in which is described by the variable t, that is oriented at some angle with respect to the bottom edge of the image. As the signal is projected down to the 1D axis, it is added to all the other signals that project to that location on the 1D axis. A full Radon Transform repeats this process for the continuum of angles between 0° and 360°. Figure 18 represents this process pictorially. In the lower left of Figure 18 is the 2D example image of Figure 17. For the 0° projection, the signals of the 2D image are summed along columns, as depicted by the red vertical vectors in Figure 18, resulting in a 1D spatial function representation of the information in the slice. The 90° projection is acquired in a similar manner, but along the rows in the slice (green vectors and plot in Figure 18). The other projection angle depicted in Figure 18 is that for a 45° projection.

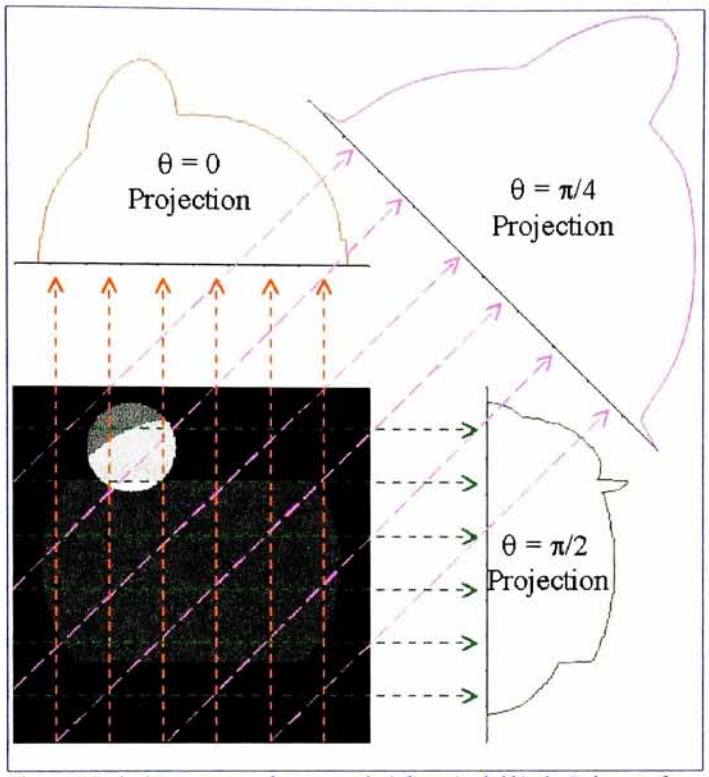

Figure 18 Projections at every angle compose the information held in the Radon transform.

The integration process used to acquire angle-dependent projection, p(θ,t), is represented by equation 11.

Equation 11

$$p(\theta,t) = \int_{-\infty}^{\infty}\int_{-\infty}^{\infty} f(x,y)\delta(x\cos\theta + y\sin\theta - t)dxdy$$

where f(x,y) represents the original 2D object, or slice through a 3D object, and δ(...) is the dirac delta function [37]. One of the better-known properties of the dirac delta function is that it is only non-zero for those arguments that are equal to zero. In other words, the delta function is equal to zero at all times except when it's argument equals zero. Therefore, the delta function of equation 11 is only non-zero when $x\cos(\theta) + y\sin\theta - t = 0$ or

$x\cos(\theta) + y\sin\theta = t$. What this means is that only the values in f(x,y) that fall along vectors defined by θ and t will be integrated together for each value of p(θ,t).

Since the Radon transform is based upon angular projections, it is often easier to represent the Radon transform using polar coordinates. This is relatively straightforward by defining the following:

Equation 12 $$x = \rho\cos(\phi)$$

Equation 13 $$y = \rho\sin(\phi)$$

Inserting these definitions into equation 11 and relying upon a trigonometric identity, namely $\cos\theta\cos\phi + \sin\theta\sin\phi = \cos(\theta - \phi)$, results in the polar coordinate representation of the Radon Transform:

Equation 14 $$p(\theta,t) = \int_0^{2\pi}\int_0^{\infty} f(\rho,\phi)\delta[\rho\cos(\theta-\phi) - t]\rho d\rho d\phi$$

2.4.2.1 Sinograms

The Radon transform of a 2D object, or of a slice through a 3D object, can be represented by a 2D function, called a sinogram. An example sinogram, which was generated using a very simplistic object (Figure 19a), is shown in Figure 19b. The structure of a sinogram is such that projection angle, θ, varies vertically while spatial position along the 1D axis of the projection, t, varies in the horizontal direction. Therefore, each row of a sinogram represents the

projection through the original object at a very particular projection angle. Each column of a sinogram represents the same spatial location along the 1D projection axis for all of the projection angles.

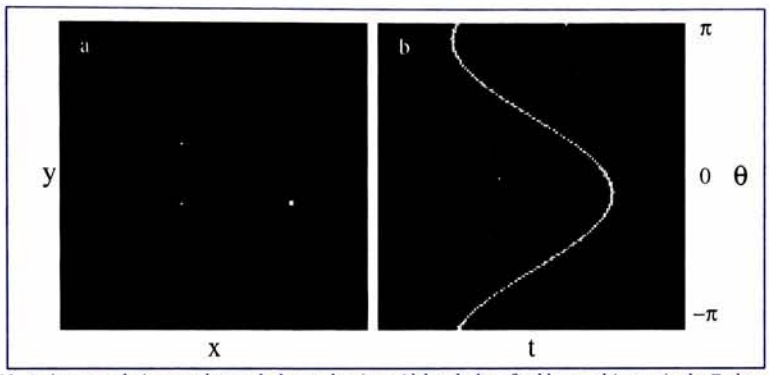

Figure 19 A sinogram, b, is named as such due to the sinusoidal path described by an object, a, in the Radon domain.

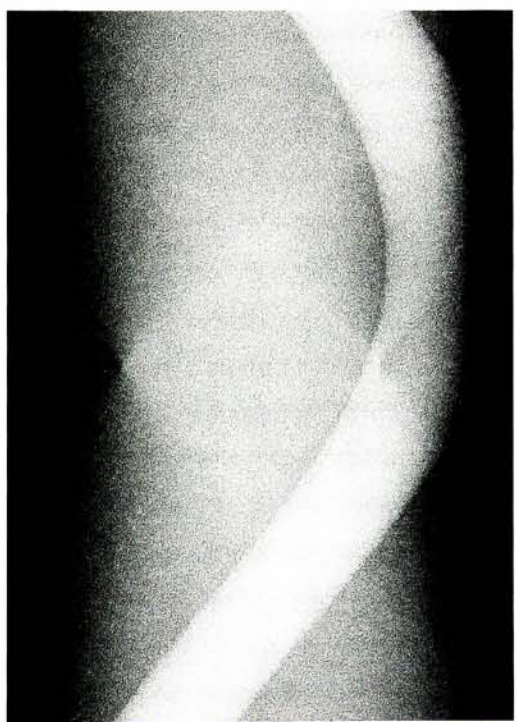

Figure 20 A sinogram is a useful method in which to display Radon transform information.

The sinogram for the example slice depicted in Figure 17 is shown in Figure 21. The structure of a sinogram is also described visually in Figure 22 using the example object's sinogram. One very important point that can be drawn from Figure 22 is the fact that the 180°, or π, projection is actually the inverse of the 0° projection. This makes intuitive sense if one continues the progression of the projections depicted in Figure 18. Due to this symmetric aspect, projections are only collected over one half of a full revolution, or $0 \leq \theta < \pi$. This projection angle range can be shifted, but best results will be obtained from the inverse Radon transform only if the range is maintained. For example, the projection angle range could easily be shifted to $-\frac{\pi}{2} \leq \theta < \frac{\pi}{2}$.

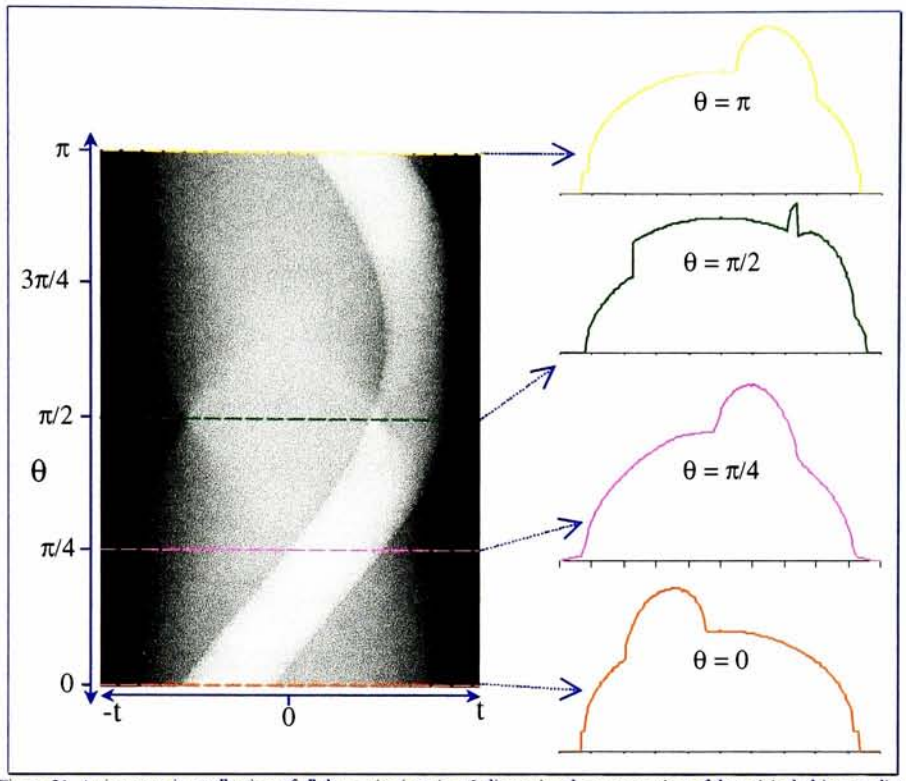

Figure 21 A sinogram is a collection of all the projections in a 2-dimensional representation of the original object or slice.

2.4.3 Backprojection

It was mentioned above that the Radon transform information could be used to recreate the original 2D object. The process of reconstructing the original object from the Radon transform data is called back-projection. The process of back-projection is so named because it aptly describes the actual process used. In the process, each projection through the original object, which is represented by each row in the sinogram, is projected, or smeared, across the reconstruction space.

The visual representation of back-projection is rather straightforward. Imagine, for a moment, taking each projection from the sinogram and smearing across a blank slate at the angle

corresponding to that projection. Then, repeat the process until all the projections in the sinogram have been used. What results is an estimate of the original 2D function, or slice through the 3D object. A very simplified cartoon of the back-projection process is depicted in Figure 22.

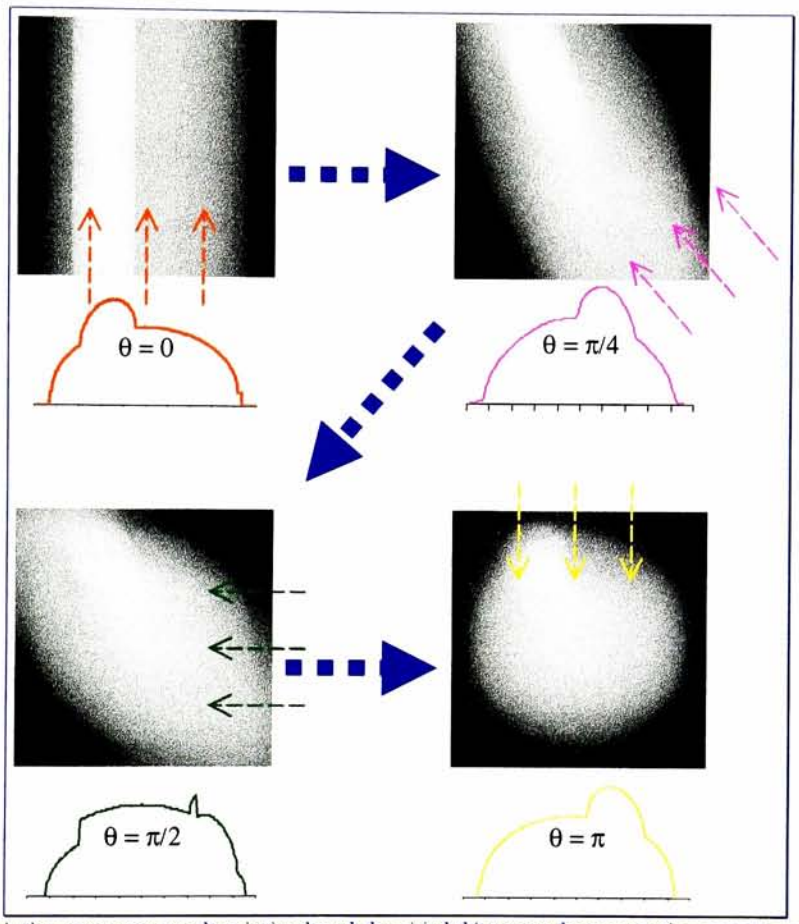

Figure 22 The backprojection process smears each projection through the original object across the reconstruction space at a corresponding projection angle to reconstruct an estimate of the original object

The back projection process used to reconstruct an estimate of the original 2D object, $\hat{f}(x, y)$, is described mathematically via equation 15. Again, it is a property of the delta function, $\delta(\tau)$, to only be non-zero where it's argument, τ, equals zero. Using this property, equation 15

suggests that only those x,y coordinates in $\hat{f}(x, y)$ that allow $x\cos(\theta) + y\sin(\theta) = t$ will receive contributions from a particular projection, p(θ,t).

Equation 15

$$\hat{f}(x, y) = \int_0^{\pi} \int_{-\infty}^{\infty} p(\theta, t)\delta[x\cos(\theta) + y\sin(\theta) - t]dtd\theta$$

As is implied by equation 15, and can be observed in Figure 22, as each projection is smeared across the reconstruction space, the contribution to any one spatial location is added to whatever amount is already there. In this manner, contributions from all projections are integrated, or summed in the discrete case, to result in a final signal at each location.

2.4.4 Filtering

Figure 23 compares a) the original 2D slice through the 3D object and b) the reconstructed 2D estimate of that original. The estimate was created using 360 projections, or one every ½ degree. It is fairly obvious that the reconstruction process, even with so many projections, does not result in an exact representation of the original. As with any discrete version of continuous theory, the Radon transform and back-projection process imparts a characteristic point spread function (PSF) on the resulting estimate of the original object.

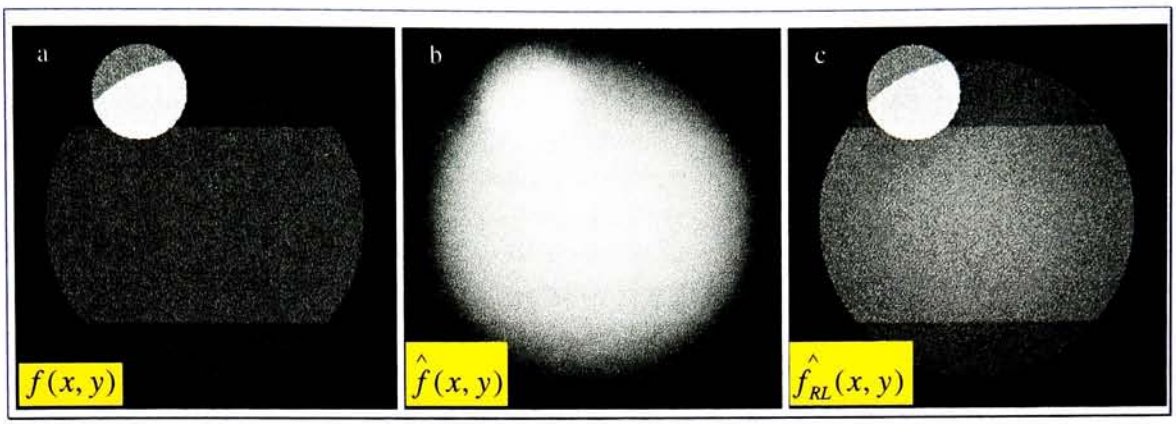

Figure 23 The reconstruction estimate, b, of the original object, a, falls a little short implying a characteristic PSF of the process, but the Ram-Lak filtered reconstruction, c, is very representative of the original.

As is described in Appendix A, and is evident in Figure 23b, the back-projection PSF is effectively a blurring function that can be compensated for by using a specific type of convolution kernel. The filter, in most applications, is implemented as a 1D convolution kernel that is convolved with each projection, or each row of the sinogram, prior to back-projection. While there are several filters that have been specifically designed to work well in the back-projection procedure (see Appendix A), the Ram-Lak filter can be used fairly effectively. Figure 23c represents the filtered reconstruction of the original seen in Figure 23a. The filtered reconstruction employed 360 projections and a 131-sample Ram-Lak filter. It is clear that a good representation of the original object is quite possible using the Radon transform and back-projection process.

Chapter 3

3. Spatial-Spatial-Spectral Theory

Based on prior research, a new spatial-spatial-spectral acquisition technique has been developed.

We have discussed current methods for acquiring spatial-spatial-spectral information, called magnetic resonance spectroscopy (MRS). In particular, localization and phase encoding techniques have been touched upon. We have also discussed some of the more prevalent limitations and disadvantages to using these techniques. In an effort to overcome some of these limitations, an alternate technique for acquiring spatial-spatial-spectral information has been developed for use on clinical MRI systems. Recent technological advances in MRI systems have made the technique a viable option for acquiring spatial-spatial-spectral information over a full MRI field-of-view.

The foundation research for the spatial-spatial-spectral imaging technique was originally studied using nuclear magnetic resonance (NMR) spectrometer systems. A quick overview of that foundation research will be provided followed by a detailed review of how the initial theory was modified and then applied to magnetic resonance imaging systems.

3.1 Foundation Research

The hypothesis that gaining spectral information would aid in quicker, easier, and more accurate identification of internal tissue structures and distinction between healthy and unhealthy tissues has been previously studied [5, 6, 14, 17, 19, 20, 21]. Lauterbur first demonstrated the fact that this information can be acquired in 1984 [1]. Lauterbur proved that projections at predictable angles through the spatial-spectral domain of a sample could be acquired by modifying the amplitude of a one-dimensional read-out gradient when acquiring the NMR data for the sample. The projection angle through the spatial-spectral domain, θ, is determined via equation 16 and from other acquisition parameters, such as the spatial extent of the object (D), sometimes referred to as the field-of-view (FOV), read-out gradient (G), gyromagnetic ratio (γ), and the spectral width of the object (Ω).

Equation 16

$$\theta = \tan^{-1}\left(\frac{\gamma GD}{\Omega}\right)$$

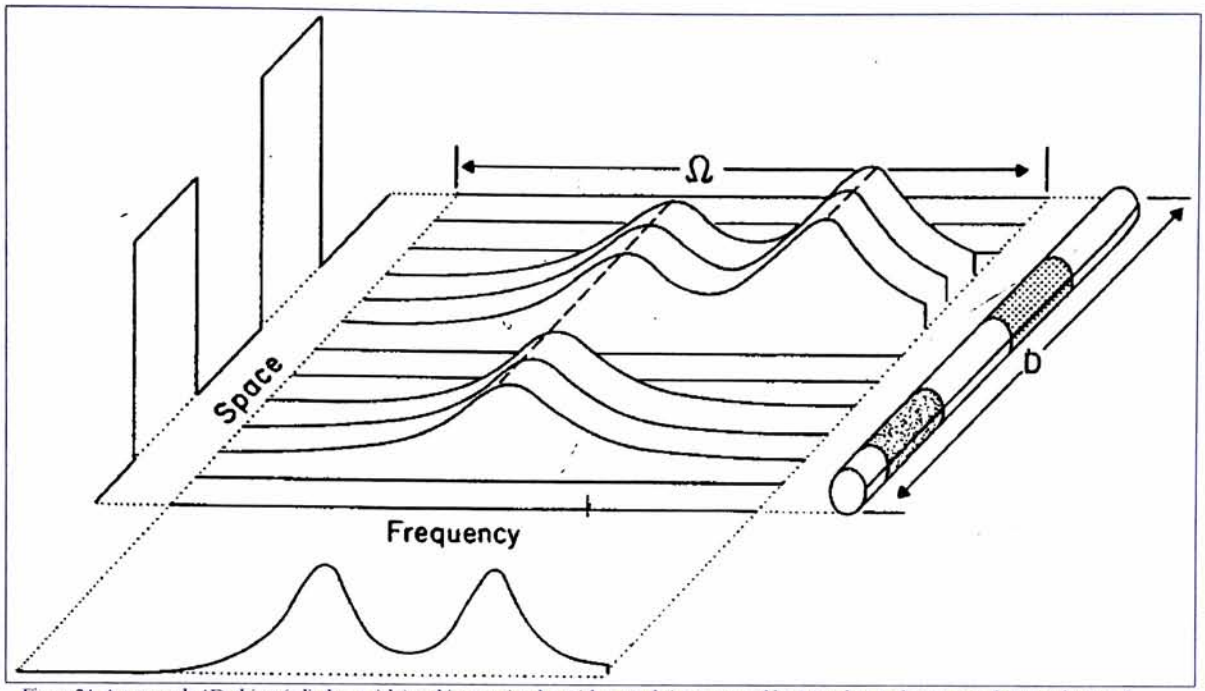

Figure 24 An example 1D object (cylindar at right) and its associated spatial-spectral signature used by Lauterbur to demonstrate his spatial-spectral imaging technique using an NMR spectrometer. Used with permission [1, pg. 537].

Figure 24 is a diagram of Lauterbur's object, it's associated spectral signatures, and the spatial signal that would normally have been acquired from that object. With a read-out gradient amplitude of 0.0 G/cm, a purely spectral signal can be acquired for each spatial location. On the other hand, an infinite read-out gradient amplitude provides a means of acquiring purely spatial content. By modifying the applied gradient appropriately and reacquiring, all combinations of spatial and spectral signals, or a full set of projections (i.e. all angles), can be recorded. The full set of projections can then be used to reconstruct the original spatial-spectral domain information through a back-projection process [4, 24, 26]. The back-projection process, as has been discussed, is a process that is used to reconstruct the interior detail of objects that have been imaged using line projections.

Although his results were quite good, as depicted by Figure 25, Lauterbur was limited by the fact that in order to acquire a full set of projections, a $\pi/2$ projection is required. However, according to equation 16, a $\pi/2$ projection requires an infinitely large gradient. The need for an infinite gradient was the cause of some consternation for Lauterbur. In fact, Lauterbur, specifically addressed a method of compensating for the fact that projections for angles approaching $\pi/2$ are unable to be acquired [5].

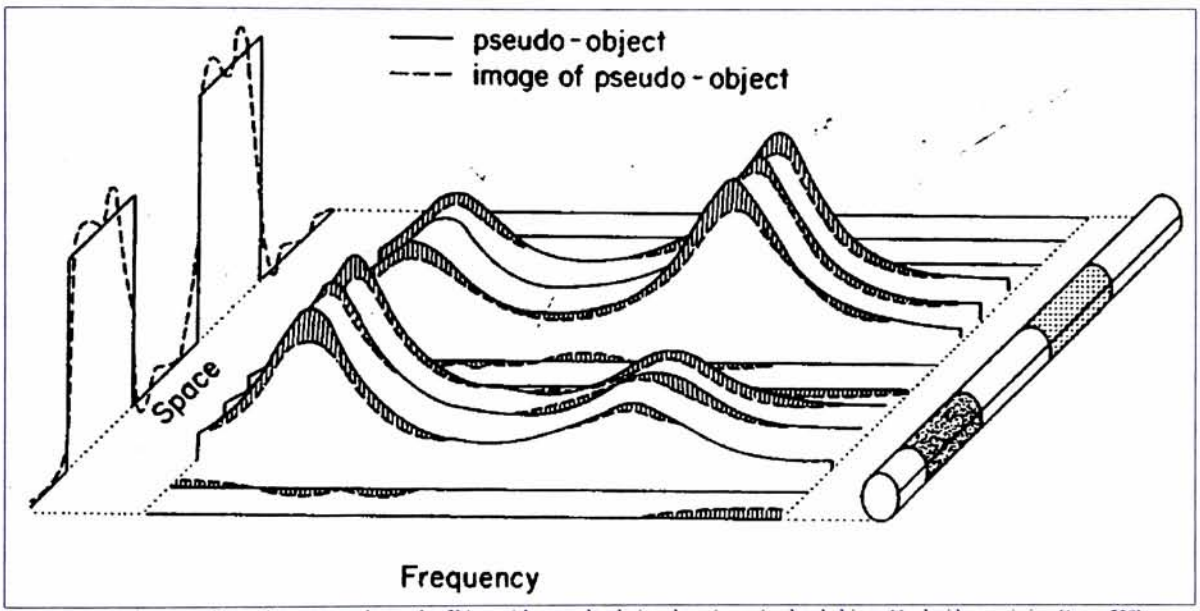

Figure 25 Lauterbur, was able to demonstrate the result of his spatial-spectral technique by using a simulated object. Used with permission [1, pg. 539].

3.2 Multi-Spectral MRI (MSMRI) Approach

A technique, based on Lauterbur's original theory, has been developed that will acquire spectral data for each and every pixel in an MRI image. What's more, this technique can be used on current clinical MR imaging systems. Examining the previously described approach, understanding the limitations of the approach, and augmenting the approach with up-to-date

technology developed the spatial-spatial-spectral imaging technique. Although the original approach was proven using an NMR spectrometer [1, 5], the basic theory works well using a clinical MRI system.

The primary difference between the two imaging systems is that the NMR spectroscopy system only gathers "images" from a 1D object whereas the MR imaging system forms images of two- and three-dimensional objects. In an NMR spectroscopy system, there is only one gradient that can be manipulated to control the projection angle. With an MR imaging system, there are many gradients that can be placed in any orientation and then manipulated to produce nearly any projection angle.

The goal of the spatial-spatial-spectral imaging technique is to acquire projections through the spatial-spectral domain of a sample. The concept is to acquire purely spatial information at one projection angle ($\theta = \pi/2$) and purely spectral information at the orthogonal projection angle ($\theta = 0$). In order to acquire purely spatial information, all chemical shift separation must be eliminated. This is accomplished by using a very large sampling rate and a high sampling bandwidth. In order to collect purely spectral information, a large chemical shift separation is desired. This requires a relatively small sampling rate at the same number of samples.

The chief limitation of Lauterbur's previous work is the fact that a purely spatial projection is unattainable, as this requires a read-out gradient of infinite amplitude, according to equation 16. This is an obvious impossibility. Not only is an infinite frequency-encoding gradient not reasonable, it is also not necessary. The gradient amplitude at the purely spatial ($\theta = \pi/2$)

projection angle need only be large enough to ensure adequate separation of the spatial information of the sample. Overcoming this limitation can be accomplished by allowing the clinical MR imaging system to determine the most appropriate frequency-encoding gradient amplitude based on the field of view of the sample and by judicious manipulation of the sampling bandwidth for each projection. This is possible because current clinical MR imaging systems have been developed to use the largest possible sampling bandwidth in order to reduce chemical shift artifacting, which is objectionable in most MRI studies.

3.2.1 Sampling Bandwidth Selection

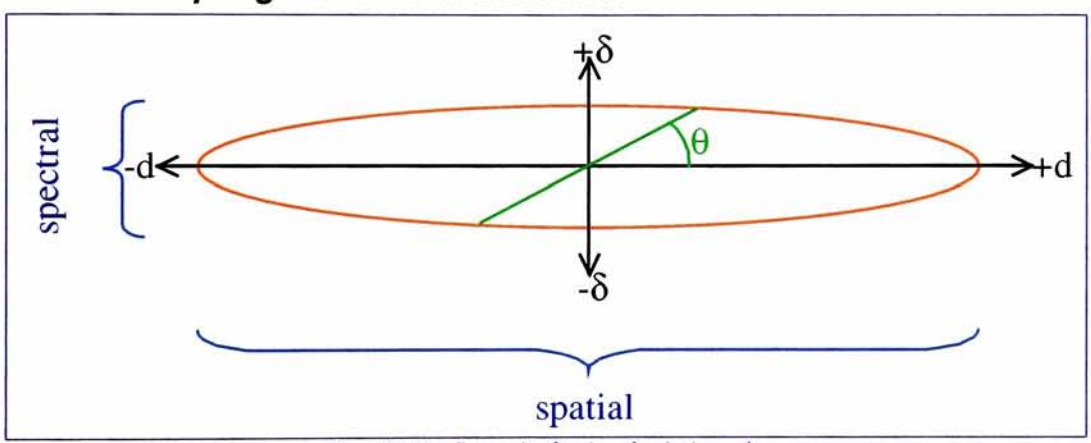

Figure 26 Sampling rate is a function of projection angle.

Figure 26 illustrates the relative relationship (not to scale) between sampling bandwidth and projection angle with respect to the axes of the spatial-spectral domain. The exact relationship is described by equation 17 and is based on the predetermined values for the purely spatial sampling bandwidth, $BW_{\pi/2}$, and the purely spectral sampling bandwidth, BW_0.

Equation 17

$$BW(\theta) = \sqrt{\frac{(BW_0\ BW_{\pi/2})^2}{(BW_0 \sin\theta)^2 + (BW_{\pi/2} \cos\theta)^2}}$$

Since the impacts due to chemical shift are minimized by higher sampling rates and chemical shift impacts should be minimized for the purely spatial ($\theta = \pi/2$) projection, the maximum available sampling bandwidth is used for this projection ($BW_{\pi/2}$). To be accurate, the sampling bandwidth should be large enough to limit all of the chemical shift spread that might be present in a single voxel to one sample in the final image. The required bandwidth can be calculated through equation 18, by using the output image number of pixels, N, and the expected chemical shift within a single voxel in frequency units, $\Delta\nu$.

Equation 18

$$\frac{BW}{N} \geq \Delta\nu$$

Using a sampling bandwidth and a number of samples whose ratio is at least as large as the width of the chemical shift will ensure that no chemical shift information will exceed one sample. This ensures that purely spatial information is collected. In other words, for any given number of samples, using the computed sampling bandwidth will ensure that the only variation in signal from one sample to the next is strictly due to variations in voxel position rather than voxel content. Of course, it is always beneficial to have more pixels in the final imagery as this directly impacts the image resolution, which in turn impacts the ability to distinguish between image features. Acquiring more and more pixels, however, requires a large and larger sampling bandwidth for purely spatial projections, as is obvious from equation 18.

When selecting the sampling bandwidth to be used for the purely spectral ($\theta = 0$) projection, one should consider the expected chemical shift width of the object being imaged. Conversion of the expected chemical shift to a frequency span can be accomplished via equation 10. Using this approach, the purely spectral sampling bandwidth, BW_0, can be determined by either measuring the spectral width of the sample prior to imaging or assuming an *a priori* spectral width for the sample. For example, if the object being imaged contains both fat and water, then one can assume a chemical shift width of approximately 3.45ppm, or 220Hz on a 1.5T MRI system. So, it makes sense for the minimum sampling bandwidth to be set at 220Hz. However, 220Hz is the span between the peaks, not the total span on the signal. Therefore, it probably makes sense to widen the sampling bandwidth a bit in order to fully contain all pertinent signals from the object. In this example, a sampling bandwidth of 300-400Hz would certainly be useful.

3.2.2 Gradient Manipulation

As was previously discussed, the spatial-spectral imaging technique requires manipulation of the read-out gradient in order to control the angle of each projection (see equation 16). Lauterbur, when demonstrating the NMR version of the technique, had only one gradient to use for this control. When employing the spatial-spatial-spectral version of the imaging technique on a clinical MR imaging system, however, there are several gradients, and combinations of gradients, from which to choose to perform this function. The most straightforward approach to implementing the spatial-spatial-spectral version of the imaging technique on a clinical MR imaging system is to manipulate the frequency-encoding gradient, G_f, to control the projection

angle, while using the slice-selection and phase-encoding gradients, G_s and G_ϕ, respectively, as in normal clinical imaging protocols.

It is fairly common with clinical MRI systems that the gradients must be set and remain stable throughout the collection of single images. In other words, G_f, G_s, and G_ϕ should be set at a fixed value and should remain constant during each image acquisition. Likewise, the sampling bandwidth, BW(θ), must remain constant for each image acquisition. Due to these stipulations, each projection angle is treated as a separate image acquisition.

Since each projection is treated as a separate image, selection of the gradient used to manipulate the projection angle is a rather easy choice. Imagine for a moment the scenario in which a slice through a given object, the location of which is controlled by G_s, is imaged such that the phase-encoding gradient, G_ϕ, is oriented along the horizontal direction within the resulting image. This means that the frequency-encoding gradient, G_f, must vary along the vertical direction of the image. By using the frequency-encoding gradient to control the projection angle in this situation the data of each column will be collected over the same spatial-spatial location, as determined by the G_s and G_ϕ gradients, while each acquired image will be at a different projection angle, which is controlled by manipulating the magnitude and direction of G_f. In other words, by setting the frequency-encoding gradient for a particular projection angle, as described by equation 16, many projections can be collected at many physical locations, one at each phase-encoding position or column in an image, all at the same projection angle, and all in one acquisition. The next acquisition, at the next G_f amplitude, will contain many projections, all at the new projection

angle. Following this procedure will produce, after some data manipulation and post-processing, a two-dimensional spatial-spectral plane for each column through the original object.

3.3 Post-acquisition Data Manipulation

Following the procedures outlined above will allow one to gather the various projections needed to back-project the spatial-spectral plane located at each column, or phase-encoding location. It is necessary, however, to perform a bit of data organization and pre-processing in order to make the collected data ready for the back-projection procedure.

3.3.1 Sinogram Creation

As was discussed in the back-projection section, it is quite convenient to format the projection data into sinograms, which will be used as the input to the back-projection procedure. To this point, several projection images have been acquired, one at each of several projection angles, θ. Within each of the projection angles, there is a projection at each of several spatial locations along the phase-encoding gradient direction, corresponding to each column in the acquired MR images. As input to the back-projection procedure, all of the projections for each phase-encoding location should be gathered together into a sinogram. To accomplish this, the same column of data from each of the acquired MR images is copied into the corresponding sinogram space at an angular position that corresponds to that MR image's projection angle. Figure 27 depicts, visually, the process of creating a single sinogram from multiple projection collections.

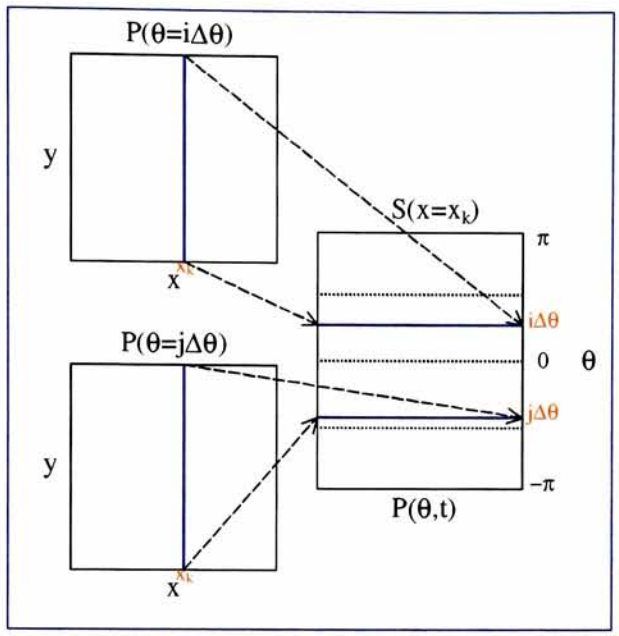

Figure 27 A sinogram (right, S(x)) can be created using the data from the same column of each acquisition (left, P(θ)).

In a way, one should think of the creation of the sinograms, one at each phase-encoding location, as a simple data organization procedure. The acquired data is being reorganized from the acquired projection images to sinograms, which are convenient for ingestion by the back-projection procedure.

3.3.2 Projection Interpolation

Due to hardware and software limitations, only very specific sampling bandwidths are available for use on clinical MRI systems. On the machine used to demonstrate the spatial-spatial-spectral technique being discussed, a maximum sampling bandwidth of 125kHz was available, which resulted in a ±62.5kHz sampling bandwidth centered on the expected Larmor frequency of the atoms being imaged. Sampling bandwidths of lower rates were only available at specific decimation ratios of this maximum rate. These lower bandwidths are determined by

dividing the maximum sampling bandwidth by decimation factors. The available sampling bandwidths on the clinical MRI system used to demonstrate the spatial-spatial-spectral technique being discussed included those in Table 1.

Table 1 Acquisition bandwidths are determined by decimating the original sampling bandwidth.

Decimation Factor	Bandwidth (±kHz)
1	62.5000
2	31.2500
3	20.8333
4	15.6250
5	12.5000
6	10.4167
7	8.9286
8	7.8125
9	6.9444
10	6.2500

Decimation Factor	Bandwidth (±kHz)
15	4.1667
16	3.9063
17	3.6765
19	3.2895
31	2.0161
32	1.9531
128	0.4883
170	0.3676
256	0.2441

Although many sampling bandwidths are listed in Table 1 as possible, very few were actually available while acquiring data (highlighted in Table 1). To further complicate matters, not all of the highlighted bandwidths were available for every study performed to demonstrate the spatial-spatial-spectral technique. In most cases, only a subset of the highlighted bandwidths was available. For example, while acquiring data for one study, which will be discussed in great detail later, only the following sampling bandwidths were available: ±15.625kHz, ±6.9444kHz, ±3.6765kHz, and ±2.0161kHz. This could be due to the fact that there is room for only 8 filters in the system at any given time; 4 of which can be set only by the system administrator [40]. It is possible that the system administrator had previously selected a subset of the possible filters and that this subset was altered between the acquisitions that support this study.

Due to the fact that the sampling bandwidths that are calculated by equation 17 are not readily available, an interpolation procedure was implemented in order to translate the acquired data, which used one of the available sampling bandwidths, to data that simulated the desired bandwidth, as calculated by equation 17. Although it may not be intuitively obvious, there are really two phenomena occurring simultaneously during the interpolation procedure. The first is that the received MRI signals have been sampled at the "wrong" sampling bandwidth (the available bandwidth rather than the desired bandwidth) and many of the resulting image pixels are dedicated to parts of the bandwidth that are of no interest to the spatial-spatial-spectral technique. For example, referring to Figure 28, one can see that the acquired bandwidth (black lines, top half of the figure) is much larger than the desired bandwidth (red lines, bottom half of the figure). Also observed from the figure is the fact that only a small number of samples are used in the desired bandwidth region (65 samples, in this example).

The other phenomena happening is that as each projection angle requires a unique desired bandwidth, some other components of Figure 28 actually change, in particular are the desired bandwidth and the number of acquired samples that fall within that bandwidth. So, in order to maintain a consistent number of samples (128 samples in this example) across all projections and to translate the acquired bandwidths to the desired bandwidths an interpolation procedure was used to resample those acquired samples that fall within the bandwidth of interest to the spatial-spatial-spectral technique.

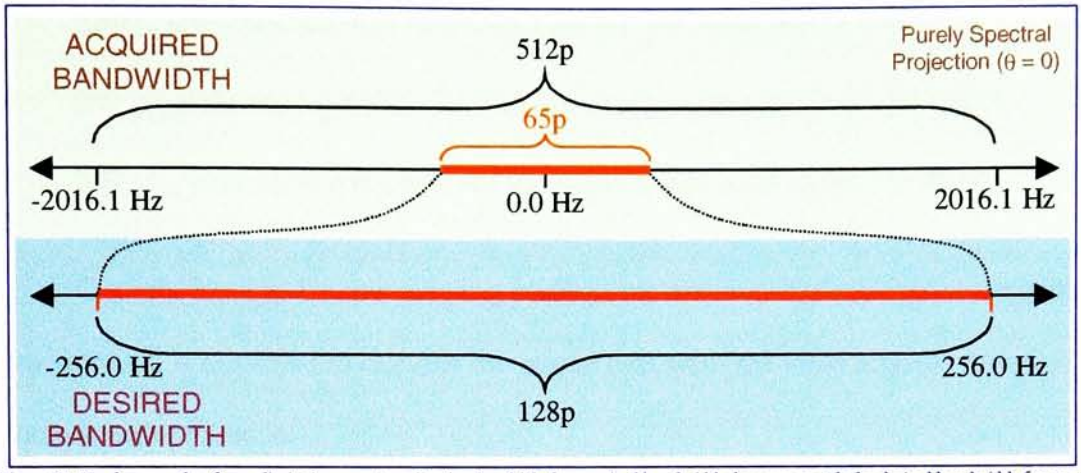

Figure 28 Hardware and software limitations create a situation in which the acquired bandwidth does not match the desired bandwidth for most projections.

In equation form, acquired projection data, y_{in}, is resampled to result in desired projection data, y_{out}. The degree of resampling needed is determined by identifying the sampling positions for the acquired data and then the output sampling positions via equations 19 and 20, respectively:

Equation 19

$$x_{in}(i) = BW_{start\_in} + i\Delta BW_{in}$$

Equation 20

$$x_{out}(j) = BW_{start\_out} + j\Delta BW_{out}$$

Where:

BW_{start_in} represents the first frequency in the acquired bandwidth;

$0 \leq i < N$, where N is the number of acquired samples per column; 512 in most cases;

BW_{start_out} represents the first frequency in the desired bandwidth;

$0 \leq j < M$, where M is the number of output samples per column; 128, in most cases;

ΔBW_{in} is the bandwidth of each acquired sample and equals $BW'(\theta) / N$;

ΔBW_{out} is the bandwidth of each output sample and equals $BW(\theta)$ / M;

BW_{start_in} is the starting frequency of the acquired samples and equals $-BW'(\theta)/2$;

BW_{start_out} is the starting frequency of the output samples and equals $-BW(\theta)/2$;

Once the input and output sampling positions are determined, a cubic spline interpolation method [41,42] is employed to calculate the output data from the input acquired data for each column in each projection.

Since the interpolation procedure is essentially creating samples where none exist, a scaling factor is applied to the result of each interpolation. The use of the scaling factor can be thought of as a means to ensure conservation of energy – that no energy, or signal, is created arbitrarily. The scaling factor is calculated as in equation 21.

Equation 21

$$s = \frac{BW_{out}}{BW_{in}} \frac{N}{M}$$

3.3.3 Filtered Back-projection

The final post-acquisition data manipulation step is to filter the constructed sinograms to account for the back-projection point spread function. As was previously discussed in the back-projection discussion, the back-projection procedure is known to impart a very well defined point spread function, which can be compensated for quite effectively by applying a 1D convolution filter to each row in the input sinogram [4, 26]. Since it is not a goal of this study to investigate the optimal back-projection filter to be used for the purposes of the spatial-spatial-spectral technique

being studied, a 65 sample Ram-Lak convolution filter[9] was applied to each row of each sinogram just prior to back-projection.

[9] More information regarding the Ram-Lak filter is available in Appendix A

Chapter 4

4. Experimental

Phantom construction and use in the demonstration of spatial-spatial-spectral imaging.

As is often done with experimental imaging systems and techniques, known objects, or targets with known characteristics, are used as test targets in order to limit the effects observed in the resulting imagery to causes within the experimental system or technique. Experimental MRI systems and techniques are no exception. As a means of testing the spatial-spatial-spectral imaging technique, test objects, called phantoms, were constructed and used as test targets.

In the case of MRI phantoms, the known objects usually consist of containers filled with well-characterized solutions. The containers are typically constructed of a material with a very short T_2. The theory is that the net magnetization vector associated with these materials realigns with B_0 in such a short amount of time that by the time the MRI system starts to acquire resonance signals, there is no signal from the container material. The solutions, on the other hand, provide signals at very specific, and well-known, times and with very specific, and well-known, spectra. The point here is that by comparing the output of the MRI system against what

the resulting MRI system should produce allows one a technique for characterizing the MRI system or the imaging techniques used by the MRI system.

Phantom complexity is typically defined by the intended use of the phantom. For example, a rather simple phantom is typically used in the calibration procedure for MRI systems. The phantoms used for this test target purpose are a simple spherical container filled with an aqueous solution of paramagnetic material, such as Ni^{++} or Mn^{++}. Knowing the concentration of the paramagnetic component of the solution will allow one to calculate the relaxation times associated with the phantom and therefore to very accurately predict the signals obtained from the MRI system. When these signals are not recorded exactly by the MRI system, the system is adjusted until the predicted and acquired signals match, thus ensuring that the correct signals will be reflected when an unknown target is imaged.

The phantoms used to characterize the spatial-spatial-spectral imaging technique being studied were constructed with the intent of a) demonstrating that the technique actually works, b) characterizing how well the technique works on uncomplicated objects, and c) how well the technique works with more complex objects.

In addition to using phantoms to characterize the spatial-spatial-spectral technique being studied, *in vivo* tissue was also used to demonstrate the technique. In particular, an axial slice through medial tibia of an adult male was imaged using the spatial-spatial-spectral technique in an effort to demonstrate the merits of the technique on actual tissues.

4.1 3Tubes Phantom

4.1.1 Phantom Construction

Construction of an MRI phantom can be rather straightforward and, in fact, construction of the 3Tubes phantom is a good example. The phantom I itself is composed of 3 glass 5mm diameter NMR tubes, placed in a plastic NMR tube holder that separates the tubes by 0.9cm each, which has been inserted into a 2.5 cm diameter, 10 cm length polyethylene cylinder.

The three NMR tubes in the 3Tubes phantom were each filled with a unique solution. The first tube contained aqueous 8mM $NiCl_2$. The second was filled with ϕ=0.6 water (8mM Ni^{+2})-AOT-decane reverse micelle (RM) [6]. The last tube of this phantom contained decane. As a baseline, the spectrum for each of the solutions was measured using an NMR spectrometer. The primary chemical shift (δ) peak locations, relative to TMS, for each solution are listed in Table 2. The three spectra are plotted as a function of chemical shift in Figure 29. The important issue to note is the relative position, in parts per million, of the spectral peaks and the relative magnitude of each. In the plot, the three spectra were normalized such that the maximum amplitude of each were equalized. The spectral normalization did not change the spectral peak locations – only scaled the relative amplitudes of the spectra. Within a given spectrum, however, relative amplitude comparisons can still be made. In particular, one should notice the fact that the amplitude of the 0.90ppm/1.30ppm peaks in the RM solution are significantly lower than the 4.75ppm peak of the same solution.

Table 2 The spectral peaks of the 3Tubes solutions were measured on an NMR spectrometer.

Solution	δ (ppm)				
Decane	1.44	1.83			
RM	0.90	1.30	3.15	4.20	4.75
Water					5.02

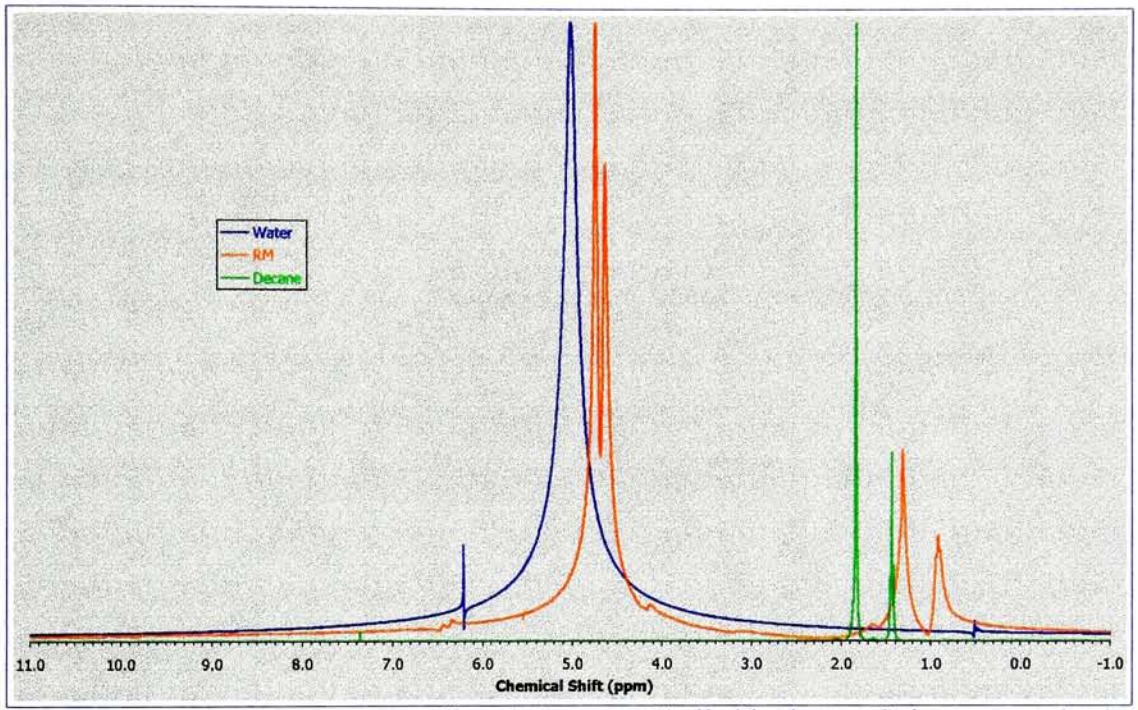

Figure 29 3Tube phantom solution spectra as measured by an NMR spectrometer (signal levels have been normalized to a common maximum).

The external polyethylene cylinder of the 3Tubes phantom was filled with an aqueous solution of 50 mM $NiCl_2$ and Gadodiamide (Nycomed) in order to minimize susceptibility artifacts, while having a minimal signal itself. This reduced susceptibility artifacts by acting as a buffer for the MRI B_0 magnetic field thus reducing the variations in the B_0 field as it encounters the 5mm NMR tubes. Utilizing a susceptibility buffer in this manner is a relatively common practice.

4.1.2 Data Acquisition

One of the advantages of the spatial-spatial-spectral image technique being studied is that it can be used in conjunction with many standard MR imaging protocols. However, in an effort to keep any affects, positive or negative, limited to the merits of the technique itself a very simple imaging protocol was used to demonstrate the spatial-spatial-spectral technique. That simple protocol is the spin echo (SE) protocol (see Appendix B). The acquisition parameters common to all of the projection acquisitions are listed in Table 3.

Table 3 3Tubes acquisition parameters.

Parameter	Value
Repetition Time (TR)	1000 msec.
Echo Time (TE)	35 msec.
Field of View (FOV)	4cm x 4cm
Slice Thickness	2.0 cm
Image Size	256p x 512p
Acquisition Time	2:20.05 min

The 2D slice through the phantom was oriented such that the image plane was perpendicular to the vertical length of the phantom. The frequency-encoding gradient (G_f) was oriented such that it ran along the same direction as a line drawn through the center of the 3 NMR tubes. This meant that the phase-encoding gradient, G_ϕ, was set to be along the image plane, but in the orthogonal direction to G_f. The orientation of the slice through the phantom is demonstrated in Figure 30. Also indicated in the figure are the slice dimensions and each tube is labeled according to its content, the properties of which were previously discussed:

A. Aqueous 8 mM $NiCl_2$ (Water)
B. ϕ=0.6 water (8mM Ni^{+2})-AOT-decane reverse micelle (RM) [17]
C. Decane

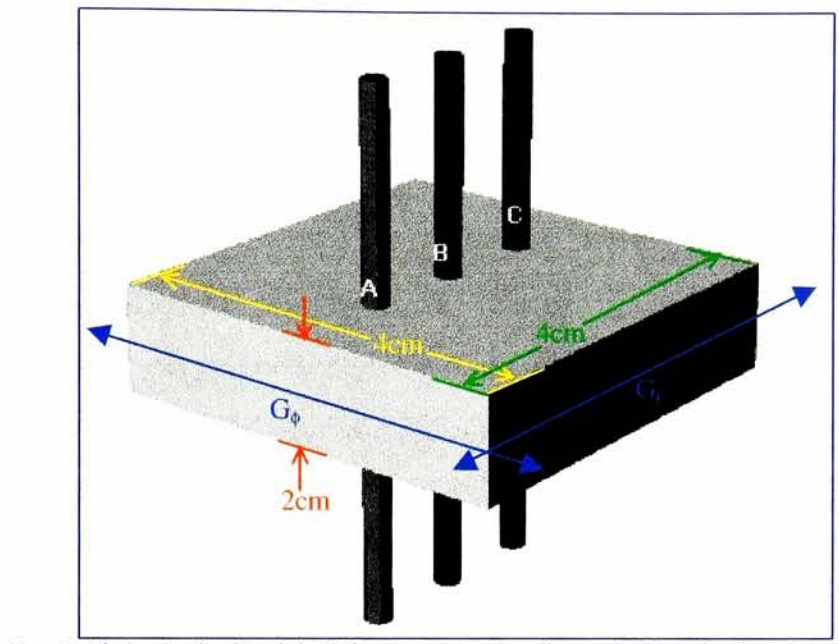

Figure 30 The imaging slice through the 3Tubes phantom was oriented perpendicularly to the phantom's vertical axis.

For each projection, a new gradient and a new sampling bandwidth were chosen, while the other acquisition parameters mentioned above were kept constant. A total of 80 projection acquisitions were collected over a projection angle range of $-\pi/2 \leq \theta \leq \pi/2$ with $\Delta\theta = 2.25$ degrees. Table 4 contains the desired bandwidth (as calculated by equation 17), frequency-encoding gradient, and acquired bandwidth, all as a function of projection angle for a handful of the more interesting projections[10]. One important point to make regarding the acquisition parameters is that the acquired bandwidth is larger than the desired bandwidth for all projection angles. This allowed for an effective use of the interpolation step discussed above. If the situation were reversed (i.e. the acquired bandwidth is less than the desired bandwidth) a situation

[10] Acquisition parameters for the complete set of projections are provided in Appendix B.

would be created in which high frequency data needed for an accurate back-projection would have been thrown away by the MRI system and would therefore be unrecoverable.

Table 4 Projection acquisition parameters associated with the 3Tubes phantom (for selected projections only).

Projection Angle θ (degrees)	Desired Bandwidth BW(θ) (kHz)	Freq.-Encoding Gradient G (G/cm)	Acquired Bandwidth BW'(θ) (kHz)[11]
-90.00	31250.000	1.834780	31250.000
-87.75	12037.765	0.700000	13889.000
-85.50	6389.038	0.381960	7353.000
-83.25	4315.061	0.253980	7353.000
-81.00	3255.648	0.189800	4032.258
-78.75	2615.622	0.151130	4032.258
-76.50	2188.181	0.125210	4032.258
⋮	⋮	⋮	⋮
-45.00	723.984	0.030060	4032.258
⋮	⋮	⋮	⋮
0.00	512.000	0.000000	4032.258
⋮	⋮	⋮	⋮
45.00	723.980	-0.030060	4032.258
⋮	⋮	⋮	⋮
76.50	2188.133	-0.125210	4032.258
78.75	2615.553	-0.151130	4032.258
81.00	3255.540	-0.189800	4032.258
83.25	4314.871	-0.253980	7353.000
85.50	6388.625	-0.381960	7353.000
87.75	12036.381	-0.700000	13889.000
90.00	31250.000	-1.834780	31250.000

Figure 31 contains the $\pi/2$, or purely spatial, projection image. One should notice that the image appears to be a typical MRI acquisition. Since this is the purely spatial projection image, that observation should hold. As is shown in the figure, the orientation of the tubes is maintained – the tube containing water is closest to the top of the image; the RM tube is in the middle; and the decane tube is nearest the bottom of the image. Another observation to be made is the fact that although the image has the same number of pixels in the vertical direction, the background

noise level indicates that only the center half of the image, in the horizontal direction, contains actual data. This is indeed true and was intentionally setup this way because the objects of interest only occupied the center portion of the field of view and acquiring only the center ½ of the FOV reduces the required imaging time by a factor of 2. Remember that this is valid since each column of the image will be treated as a separate spatial-spectral plane. Therefore, columns outside those occupied by the objects of interest will contain only noise or extraneous information and will only prove to increase acquisition and processing times.

In Figure 32, the 0 degree, or purely spectral, projection is displayed. This is obviously not a typical MRI image. One should note that there appears to be two distinct signals in the vertical direction of the image, which corresponds to the frequency direction. One of the signal locations is that from water spectral peaks, the other is from the hydrocarbon spectral location, which in this case is composed of decane and the secondary RM peak.

[11] BW, in this context, is treated as the full bandwidth rather than the half-width (i.e. 31250kHz = ±15625kHz)

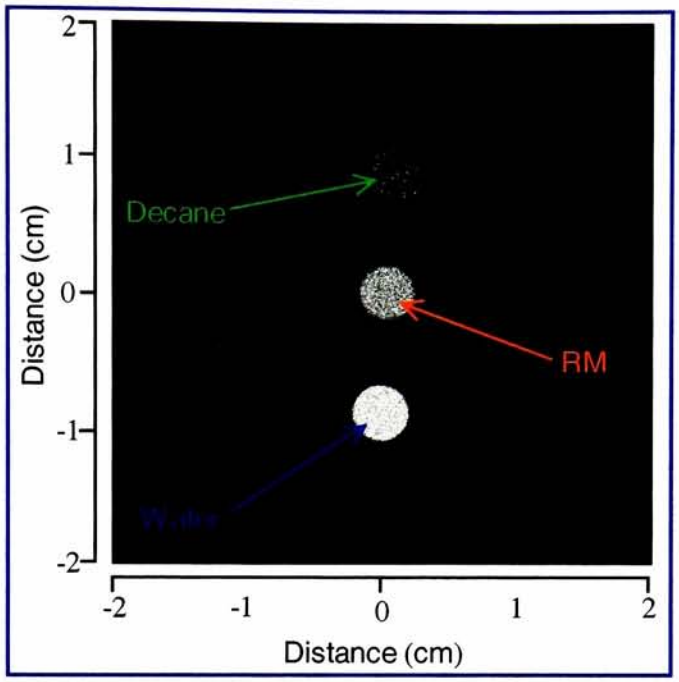

Figure 31 As should be expected, the π/2, or purely spatial, projection appears to be a typical MRI acquisition.

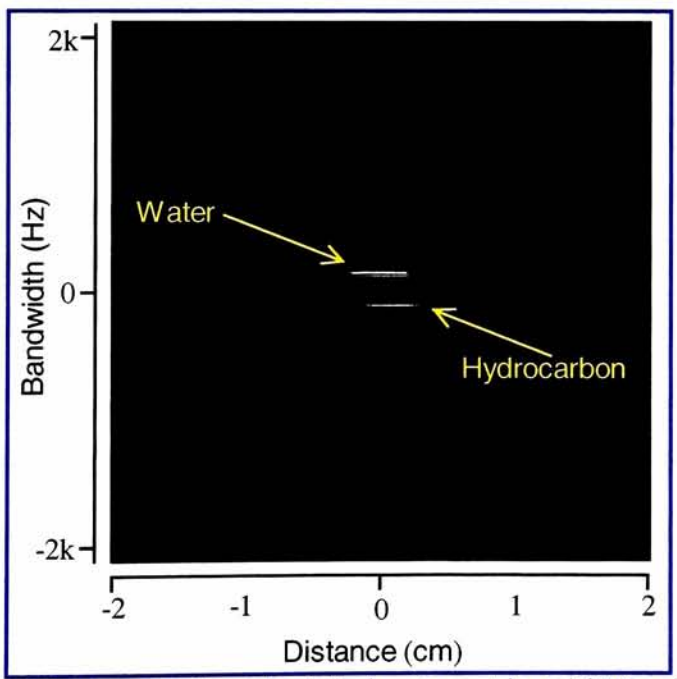

Figure 32 The 0 degree, or purely spectral, projection does not appear to be a typical MRI acquisition.

4.1.3 Results

Since the imaging technique being studied produces a volume of data, it is difficult to display the results of the technique all at once. Therefore, the resulting data volume has been sliced into 2D planes. An example 2D plane is depicted in Figure 33 - a copy of Figure 31 is included for reference.

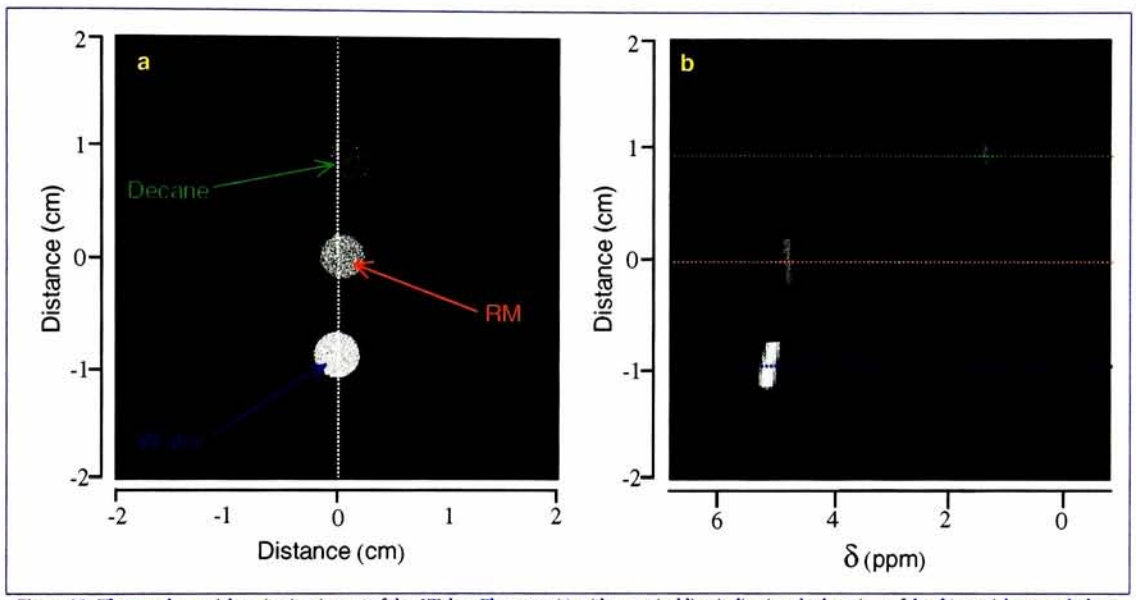

Figure 33 The purely spatial projection image of the 3Tubes Phanotm (a) with a vertical line indicating the location of the (b) spatial-spectral plane.

The dotted line that runs through Figure 33a represents the location of the spatial-spectral plane depicted in Figure 33b. There are several important observations to be made from Figure 33b. The first of which is the fact that there is a very strong signal in the spatial area that corresponds to the water tube (e.g. -1.0 cm) and that the chemical shift of that signal is located near the 5 ppm position on the chemical shift scale. This chemical shift value corresponds nicely with the water peak location that was reported in Table 2. Next, there is a rather strong signal that straddles the 0.0 cm hash mark and falls just below the 5.0 ppm position on the chemical shift scale. This peak corresponds, roughly, with the 4.75 ppm RM peak as reported in Table 2. Next,

there is a strong signal located at approximately 1.0 cm and 1.25 ppm. This signal is located in the spatial range that corresponds to the decane tube and in a spectral range that is similar to the lowest peak location reported for decane in Table 2.

One last observation can be made from Figure 33b. Although it is a bit more of a challenge for the reader to visually resolve, there is a second peak in the spatial area that corresponds to the RM tube (i.e. 0.0 cm). The location of this second chemical shift peak (i.e. ~1.25 ppm) closely resembles the second RM peak reported in Table 2.

The horizontal lines that overlay Figure 33b represent the locations from which data was extracted and plotted on a two-dimensional scatter plot, which is found in Figure 34. As with Figure 33b, there are several important observations to be made from this plot. First and foremost, the locations of the primary peaks, as listed by the small text notations, correspond very closely to those reported in Table 2 for water, and the two RM peaks – both of which are more readily observed in the plot than in Figure 33b. Second, the water and hydrocarbon peaks in the RM solution are resolved. Third, the CH_3 and CH_2 peaks from the decane solution were unresolved. Next, the technique was able to detect a difference between the chemical shift of water in the aqueous 8 mM $NiCl_2$ (5.05 ppm) and water in the RM solution (4.75 ppm).

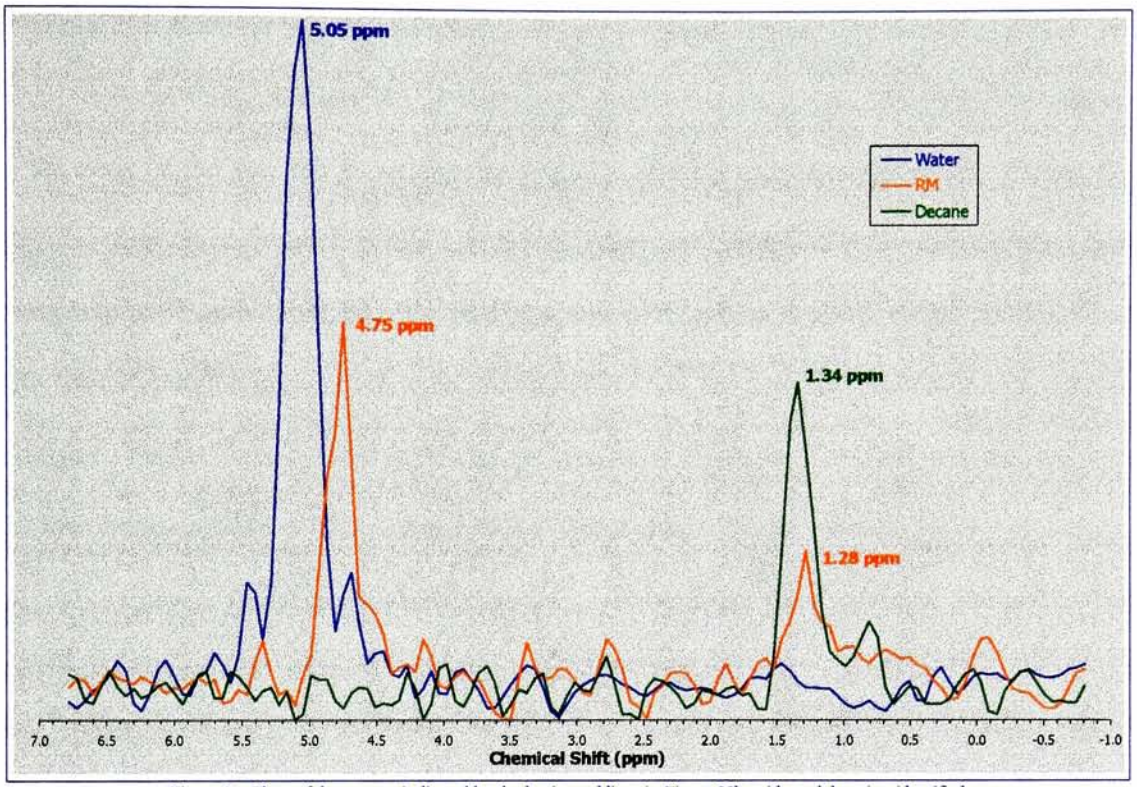

Figure 34 Plots of the spectra indicated by the horizontal lines in Figure 33b, with peak location identified.

4.2 Chambered Phantom

4.2.1 Phantom Construction

In order to provide some idea as to the efficacy of the spatial-spatial-spectral technique on slightly more complicated objects, a second phantom was constructed using sections of PVC pipe with various diameters. First, three tubes of like diameter (1.61 cm outside diameter (OD), 1.18 cm inside diameter (ID)) were located in a row such that their cylindrical axes were parallel and separated by 2.51 cm - a similar geometry as the 3Tube phantom described above, only at a slightly larger scale. The three small tubes created three chambers. The first three tubes were

then surrounded by a larger tube (8.90 cm OD, 7.72 cm ID) which created a fourth chamber. Finally, a fifth chamber was created when two funnel-shaped tubes (12.81 cm OD_{max}, 11.47 cm ID_{max}, 10.16 cm OD_{min}, 8.96 cm ID_{min}) were placed outside the other four. Endplates were affixed to the ends of the inverted funnel-shaped pieces to seal the individual chambers. Figure 35a displays three unassembled pieces of the phantom to allow one to visualize the final configuration. Figure 35b depicts the final phantom as it appears in an assembled configuration, with the exception that the actual phantom has fill-holes in the top-plate that are not depicted in the figure. Figure 35c is a cut-away view of the composite phantom. This final view clearly shows the five chambers, labeled A through E, prior to being filled with test solutions.

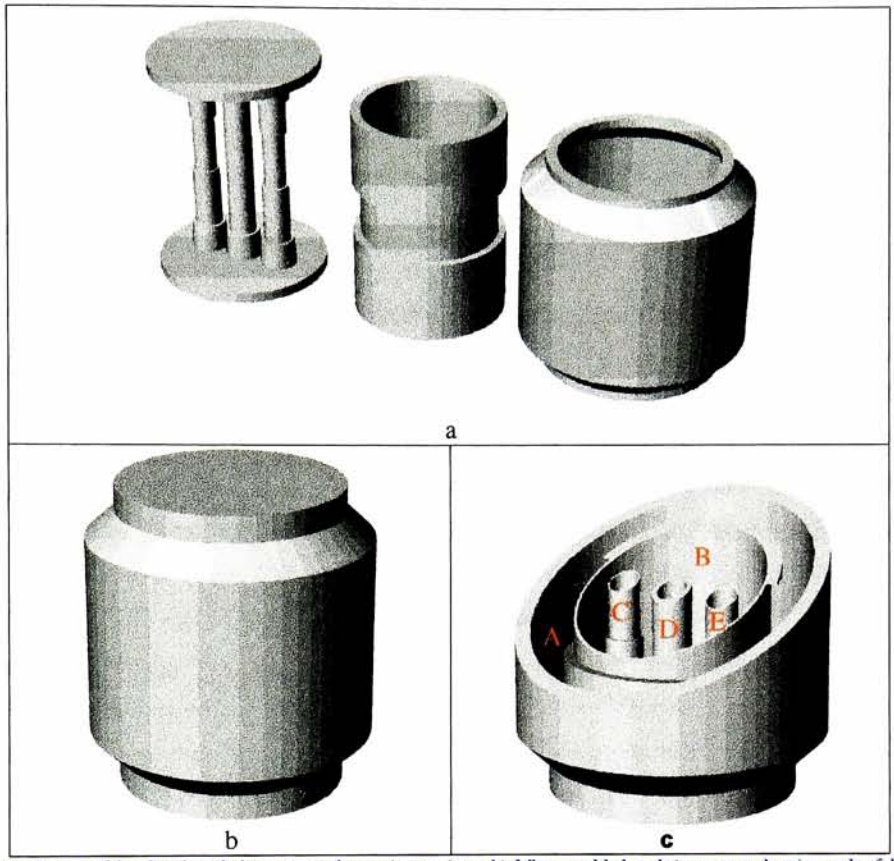

Figure 35 2D renderings of the chambered phantom: a) three primary pieces, b) fully assembled, and c) cut-away showing each of the 5 reservoirs.

As with the 3Tubes phantom, each of the resevoirs of the chambered phantom were filled with a unique solution (the letter corresponds to the resevoir as depicted in Figure 35c):

A. Corn Oil (Wegmans, Rochester, NY)
B. Aqueous 1.63×10^{-4} M Mn^{++}
C. Ethanol [95%]
D. Olive Oil (Casa Villa, Rochester, NY)
E. RM (same solution as for the 3Tube phantom)

These solutions were specifically chosen to test a variaty of issues. First, the same RM solution as was used in the 3Tubes phantom was chosen for one of the reservoirs to enable

comparisons between the two phantoms. Next, aqueous Mn^{++} was used to allow for similar comparisons to the 3Tubes phantom as well as to simulate the large water peak present in MRI studies of muscle tissue, such as in the human leg. Furthering the human tissue simulation theme, two types of oil were used for two of the reservoirs of the chambered phantom. Two oils were chosen to test the ability of the spatial-spatial-spectral technique to distinguish between spectra of very similar content. Finally, ethanol was chosen for the last reservoir as ethanol has relatively low signal and peaks in locations that are quite different than the other solutions. In particular, there is an ethanol peak near 3.5ppm, which is not at either the hydrocarbon nor the water peak locations that are likely exhibited by the other 4 solutions. The primary chemical shift (δ) peak locations, relative to TMS, for each solution are listed in Table 5.

Table 5 The spectral peaks of the chambered phantom solutions were measured on an NMR spectrometer.

Solution	**δ (ppm)**						
Corn Oil	0.9	1.3	1.6	2.0	2.32	4.27	5.37
Ethanol	1.0				3.5		4.7
Olive Oil	0.9	1.3	1.6	2.0	2.32	4.27	5.37
RM	0.9	1.30		3.15		4.20	4.75
Water							5.02

As one can readily see from Table 5, corn oil and olive oil have very similar spectral component peaks. The reason for this is that they also have very similar chemical components. Figure 36 lists the primary constituents of the two solutions, which are primarily mixed glycerides. As can be seen the primary difference in composition is the relative amounts of oleic and linoleic acids in the two solutions. Despite this difference in composition, the spectral peak locations for the two solutions remain quite similar.

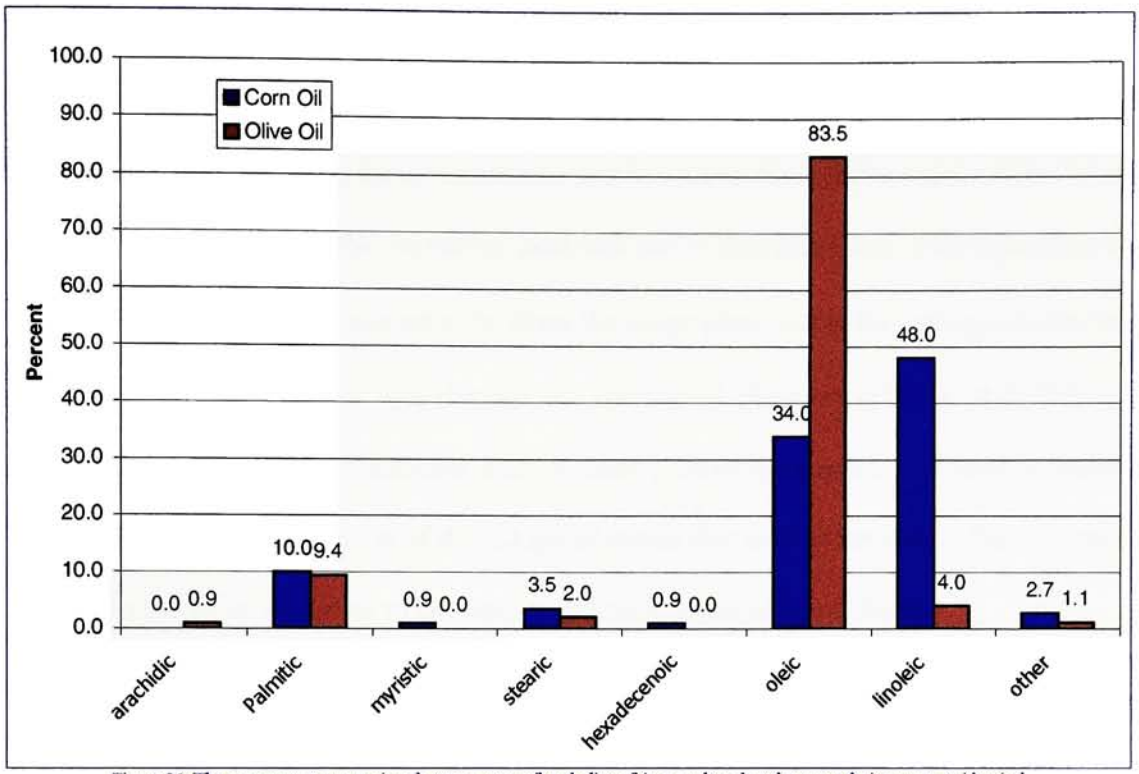

Figure 36 The component comparison between corn oil and olive oil is very close, but the two solutions are not identical.

4.2.2 Data Acquisition

As with the 3Tubes phantom, a simple Spin Echo imaging protocol was used for the chambered phantom projection acquisitions. The shared acquisition parameters are listed in Table 9.

Table 6 Chambered phantom acquisition parameters.

Parameter	Value
Repetition Time (TR)	500 msec.
Echo Time (TE)	35 msec.
Field of View (FOV)	16cm x 16cm
Slice Thickness	0.5 cm
Image Size	256p x 512p
Acquisition Time	2:16.05 min

The 2D slice through the phantom was oriented such that the image plane was perpendicular to the vertical length of the phantom. The frequency-encoding gradient (G_f) was oriented such that it ran along the same direction as a line drawn through the center of the 3 small inner tubes (this is similar to the orientation used with the 3Tubes phantom). This meant that the phase-encoding gradient, G_ϕ, was set to be along the image plane, but in the orthogonal direction to G_f. Figure 37 is a sagittal slice through the chambered phantom (TE/TR = 9/250msec, thickness = 0.3cm, BW = ±15.625kHz, FOV = 16cm^2, 256x256 samples). It is used to indicate the relative thickness and location of the 2D spatial-spatial slice used in this study. Each chamber is labeled in the figure according to its contents and the lettering assigned above.

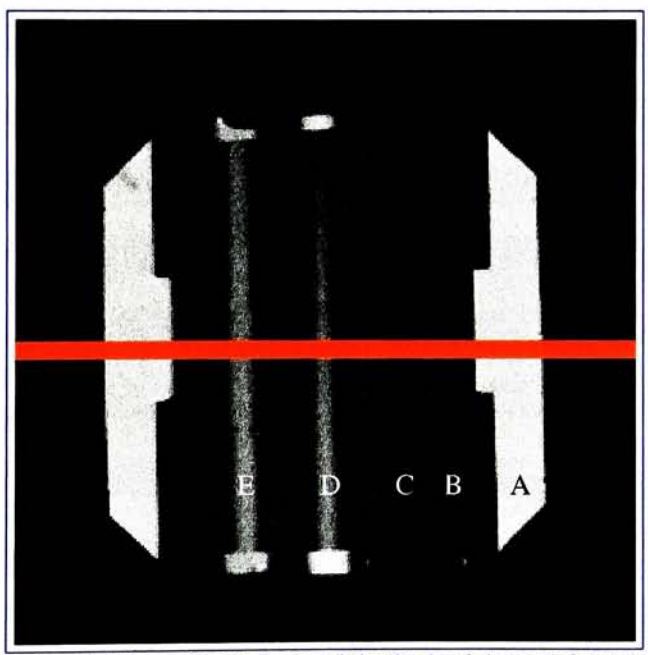

Figure 37 Relative placement and thickness of the 2D slice through the Chambered phantom is first viewed using a sagittal slice.

The relative position of the 2D slice used in this study was chosen as indicated in Figure 37 so as to use portions of the phantom in which the thickness of the PVC tubes had been

reduced. The intent of reducing the wall thickness for the PVC tubes was to simulate a solution-to-solution interface as much as possible. One can see from Figure 37 that this may have been achieved at some interfaces, but not at all. For example, the wall thickness of the reservoir labeled "D" retained a normal thickness causing the interfaces between this solution and its surrounding solution (labeled "B") to be non-adjacent.

For each projection, a new gradient and a new sampling bandwidth were chosen, while the other acquisition parameters that were presented above were kept constant. A total of 40 projection acquisitions were collected over a projection angle range of $-\pi/2 \leq \theta \leq \pi/2$ with $\Delta\theta =$ 4.5 degrees. Table 7 contains the desired bandwidth (as calculated by equation 17), frequency-encoding gradient, and acquired bandwidth, all as a function of projection angle for a handful of the more interesting projections[12]. As with the 3Tubes phantom, the acquisition bandwidth used for the chambered phantom projections was wider than the desired bandwidth in order to allow for effective interpolation later in the procedure. Also as with the 3Tubes phantom acquisitions, nearly all of the projections were acquired with a relatively small bandwidth of 4.032kHz because it was to the smallest bandwidth available on the MRI system at the time the data was acquired.

Table 7 Projection acquisition parameters associated with the chambered phantom.

Projection Angle θ (degrees)	Desired Bandwidth BW(θ) (kHz)	Freq.-Encoding Gradient G (G/cm)	Acquired Bandwidth BW'(θ) (kHz)[13]
-90.00	31250.000	-0.917606	62500.000
-85.50	6389.038	0.095515	6578.947
-81.00	3255.648	0.047461	4032.258

[12] Acquisition parameters for the complete set of projections are provided in Appendix B.
[13] BW, in this context, is treated as the full bandwidth rather than the half-width (i.e. 31250kHz = ±15625kHz)

-76.50	2188.181	0.031311	4032.258
-72.00	1654.786	0.023135	4032.258
⋮	⋮	⋮	⋮
-45.00	723.984	0.007517	4032.258
⋮	⋮	⋮	⋮
0.00	512.000	0.000000	4032.258
⋮	⋮	⋮	⋮
45.00	723.980	-0.007517	4032.258
⋮	⋮	⋮	⋮
72.00	1654.759	-0.023135	4032.258
76.50	2188.133	-0.031311	4032.258
81.00	3255.540	-0.047461	4032.258
85.50	6388.625	-0.095515	6578.947
90.00	31250.000	0.917606	62500.000

Figure 38 contains the $\pi/2$, or purely spatial, projection image through the chambered phantom. One should note that the image appears to be a typical MRI acquisition, just as with the 3Tubes acquisition. Again, as with the 3Tubes phantom, the relative spatial locations of the various chambers are clearly visible, however, labels have been added to assist in the placement of the solutions with the appropriate chambers. One should be able to notice a very slight chemical shift artifact at the vertical boundaries between the oil and water solutions. This is evident because the stipulation of equation 18 was not maintained. With a BW of 31250 and 512 pixels, a frequency width of 220 Hz results in approximately 1.8 pixels of chemical shift.

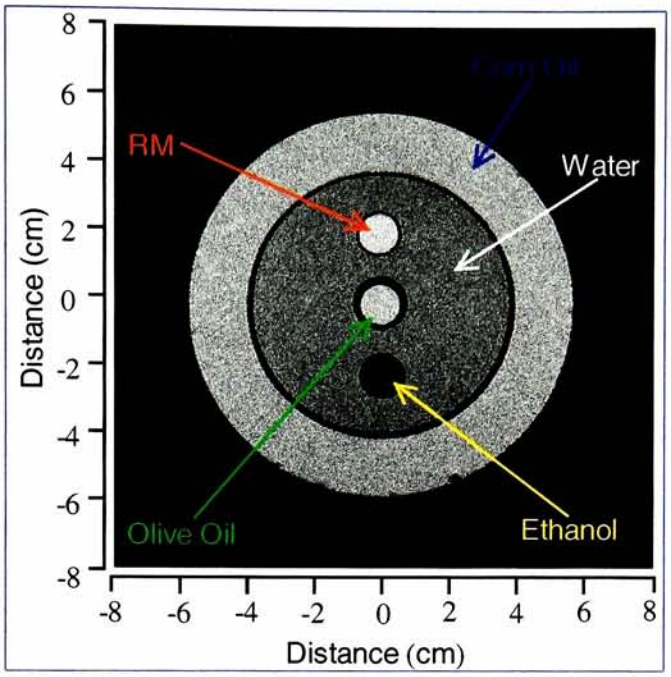

Figure 38 Each solution chamber is clearly visible in the $\pi/2$, or purely spatial, projection.

In Figure 39, the 0 degree, or purely spectral, projection is displayed. This is obviously not a typical MRI image. One should note that there appears to be two distinct signals in the vertical direction of the image, which corresponds to the frequency direction. One of the signal locations is that from water spectral peaks, the other is from the hydrocarbon spectral location, which in this case is composed of corn oil, olive oil, and the secondary RM peak.

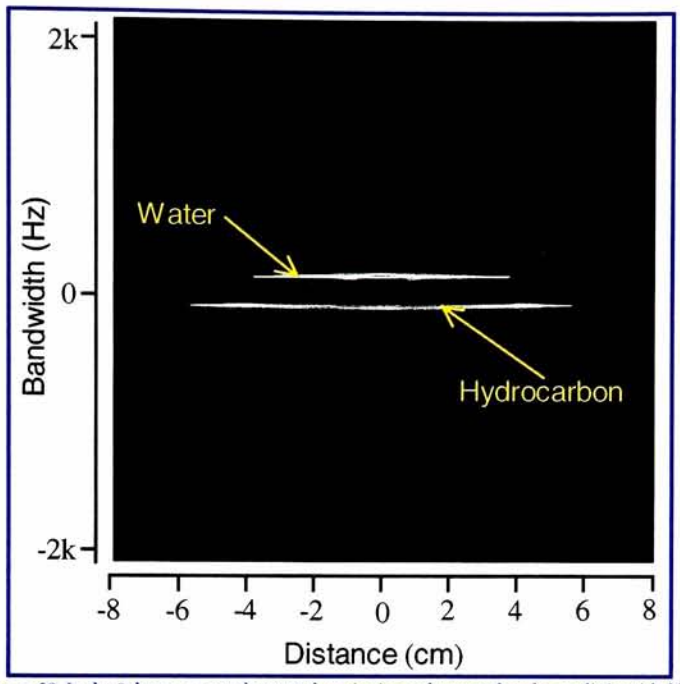

Figure 39 In the 0 degree, or purely spectral, projection only spectral peaks are distinguishable.

4.2.3 Results

The results derived from the chambered phantom data set are in many ways very similar to the results derived from the 3Tubes phantom data set. Figure 40a shows the purely spatial projection image of the chambered phantom. It is a copy of the image in Figure 38. The vertical line through the center of Figure 40a indicates the location of the spatial-spectral plane depicted in Figure 40b. Again, as with the 3Tubes phantom, one can see that the 16 cm FOV is maintained in the vertical, or spatial dimension. The other dimension, the spectral dimension, ranges from approximately –1.0 ppm to 7.0 ppm.

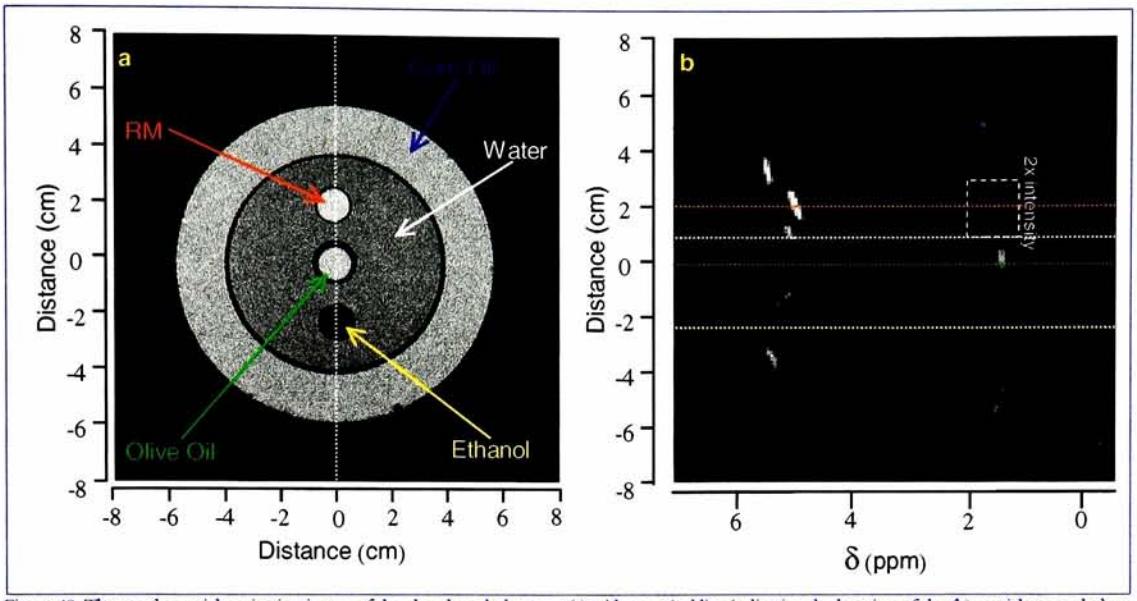

Figure 40 The purely spatial projection image of the chambered phantom (a) with a vertical line indicating the location of the (b) spatial-spectral plane.

Generally speaking, one can see that the chambered phantom results, as displayed, indicate spectral peaks that correspond with the spatial and spectral location that one would expect. For example, there are corn oil peaks in the ~1.5 ppm region for spatial locations that are indicated as being corn oil in Figure 40a. Likewise, there is a similar spectral peak for the olive oil reservoir spatial location. In the 5.0 ppm spectral region, one can see peaks whose spatial locations correspond with the water spatial locations. The final set of peaks of note in Figure 40b, are the reverse micelle peaks. The first RM peak is in the 4.75 ppm region while the other, the intensity of which has been scaled by a factor of 2 to promote visualization, is in the 1.5 ppm region.

The horizontal lines that overlay Figure 40b represent the locations from which data was extracted and plotted on a two-dimensional scatter plot, which is found in Figure 41. A representative trace was selected for each of the solutions. For example, although there are 4

spatial positions from which plots of the water spectrum could have been used, only one was plotted with the other solutions in Figure 41. The water peak resulting from the chambered phantom appears at 5.09 ppm. This peak should fall near 5.02 ppm as listed in Table 5 or near 5.05 ppm as was seen for the 3Tubes data. This seems to be consistent – within 1.4% error when compared to the NMR spectral measurements. On the other hand, the two RM peaks in the chambered phantom data set (4.97 ppm and 1.51 ppm) do not match the two 3Tubes RM peaks (4.75 ppm and 1.28 ppm) – relative errors of 4.6% and 18.0%, respectively. Then again, the spectral distance between the RM peaks in the chambered phantom data were very similar to that of the 3Tubes data. The distances were 3.46 ppm and 3.47 ppm, respectively. Also on the positive side, the water and hydrocarbon peaks in the RM solution were resolved. And finally, the spatial-spatial-spectral technique was able to detect a difference between the chemical shift of water in the aqueous 8 mM $NiCl_2$ (5.09 ppm) and water in the RM solution (4.97 ppm), just as in the 3Tubes data set.

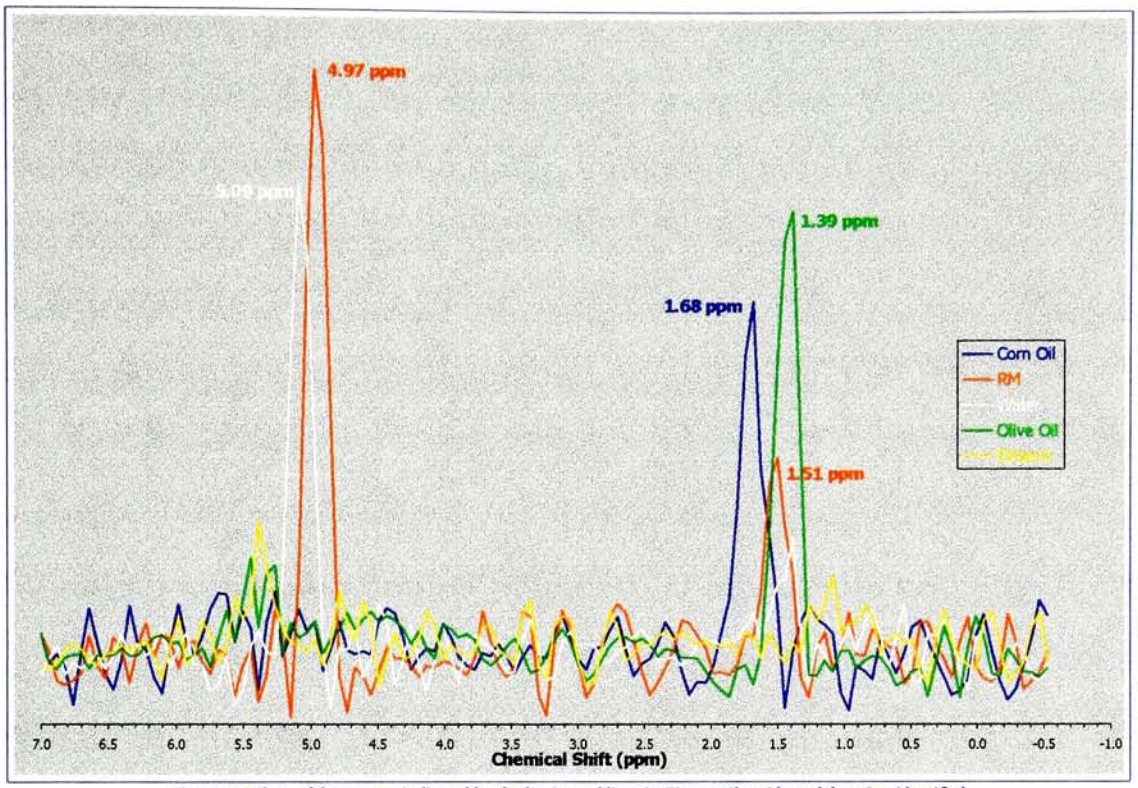

Figure 41 Plots of the spectra indicated by the horizontal lines in Figure 40b, with peak location identified.

4.2.3.1 Three-Dimensional Surface Rendering

As another means of depicting the results of the chambered phantom data set, a three-dimensional surface rendering is displayed in Figure 42. Applying a threshold to the entire data cube and then projecting the created surface to two-dimensions created this rendering. To orient one's self when viewing the figure, annotations have been added to the data cube edges and labels have been added to indicate the solutions from which signal contributions have been made.

There are many observations to be made from Figure 42. Not least of which is the fact that there are essentially two "planes" of data. This makes intuitive sense in that the solutions used in the chambered phantom primarily exhibited peaks either near the water peak location or

near the hydrocarbon peak location. Right off the bat, one can see that there is a large circular ring to the left of the figure. This ring is the signal produced by the corn oil solution in the outermost reservoir of the chambered phantom. Within the corn oil ring, in approximately the same spectral location, are two smaller surfaces. The one in what would be the very center of the phantom is the olive oil signal surface. The other, much smaller surface is the hydrocarbon peak from the RM solution in one of the small inner chambers of the phantom.

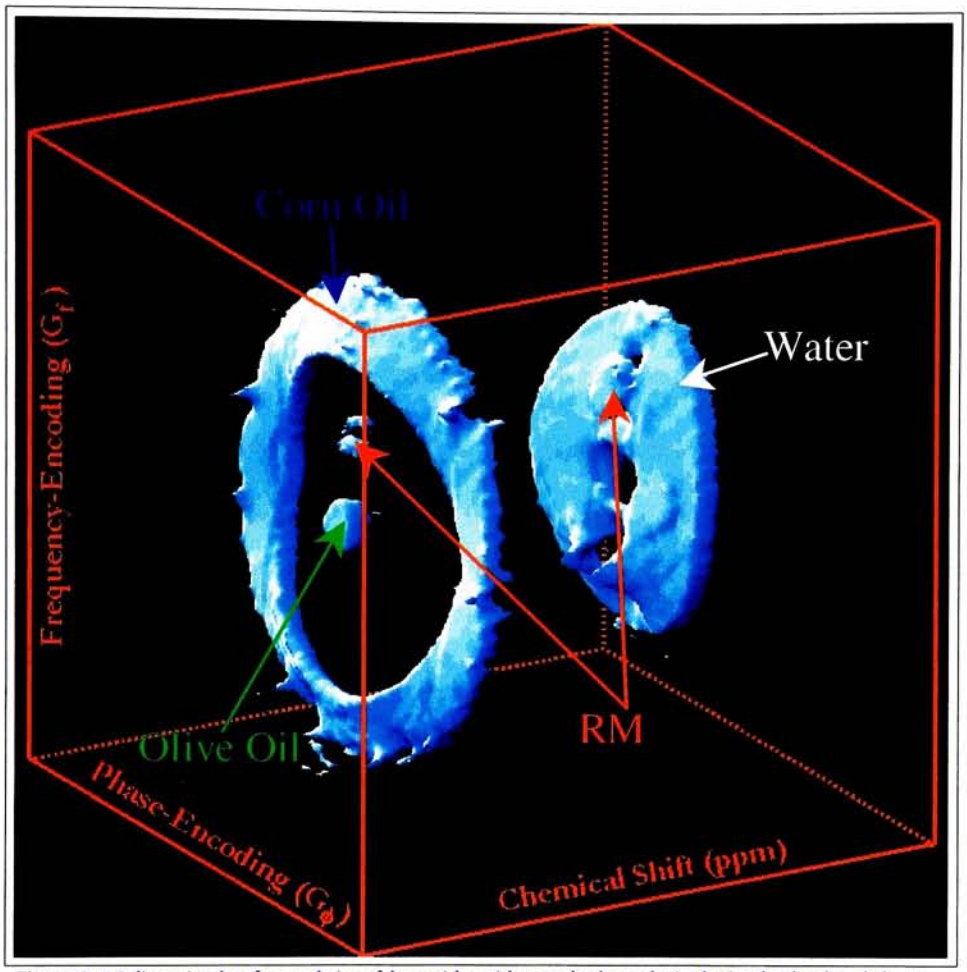

Figure 42 A 3-dimensional surface rendering of the spatial-spatial-spectral volume obtained using the chambered phantom.

The primary surface at the other spectral location as displayed in Figure 42 is produced by the water solution in the large inner chamber of the phantom. Although it is more difficult to see, the RM water peak surface can also be observed in the same general spectral area. It is also interesting to note from Figure 42 that there is no surface in what would be the ethanol chamber. This is consistent with the previous imagery and data plots presented thus far (Figure 37, Figure 38, Figure 40, and Figure 41).

One should also observe from Figure 42, that the two spectral surfaces are not quite as planar as one might have expected. The non-planar characteristic of the spectral surfaces is likely caused by a phenomenon referred to as susceptibility.

4.3 Susceptibility

It can be seen in Figure 42 that the surfaces at the respective spectral locations are not planar, as one might expect due to the fact that a single solution fills each reservoir and the single solution should exhibit a single spectrum regardless of spatial location. This can primarily be seen with the large corn oil and water surfaces. This observation can also be made from Figure 40b. One would expect the spectral signature of a single solution to remain constant independent of the spatial location of the solution. In Figure 40b, it can readily be seen that most of the spectral signals do not start and remain at a constant chemical shift location as the peak traverses its spatial extent. In fact, it seems as a solution's spatial location increases away from the spatial center of the phantom, the solution's spectral non-uniformity increases.

One possible explanation for the non-uniform spectral surfaces is the presence of susceptibility. Susceptibility is an MRI artifact that is essentially caused by variations in the magnetic field throughout an object. Susceptibility, as it pertains to the spatial-spatial-spectral technique being studied, will be discussed in a later section.

Studying the issue of susceptibility in a slightly different manner revealed something rather interesting. By closely examining and comparing the frequency position of the spectral peaks within the corn oil and water solutions of the chambered phantom a "map" of the

susceptibility was created for each solution. Susceptibility maps created from the water and corn oil solutions of the chambered phantom are found in Figure 43. A combined susceptibility map is depicted in Figure 44.

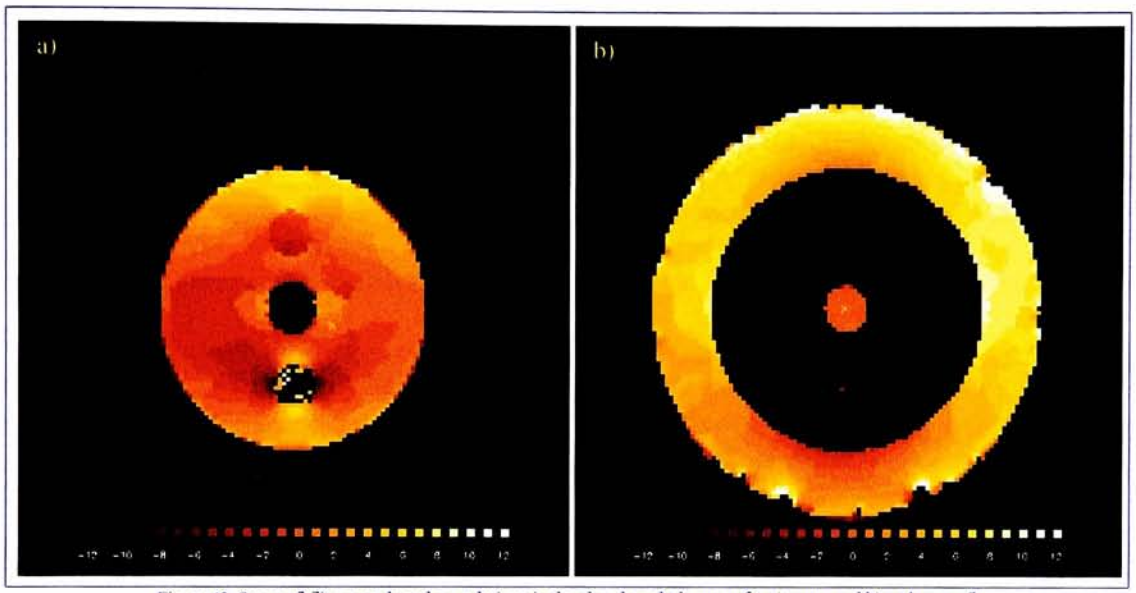

Figure 43 Susceptibility maps based on solutions in the chambered phantom for a) water and b) and corn oil.

The susceptibility maps were created by computing the difference in the spectral location of the water peak for each spatial-spatial location to that of a reference spatial-spatial position. That reference position is indicated by a small white "x" in Figure 43a. The spectral location difference is measured in number of pixels, in the spectral direction, of course, keeping in mind that the chemical shift range of approximately –1.0 to 7.0 is covered by 128 pixels. This translates to 0.0625ppm for each spectral pixel position change. Figure 43b represents a similar susceptibility map for the corn oil and olive oil reservoirs.

Interesting observations can be made form the susceptibility maps of Figure 43 and Figure 44. To begin with, the iso-lines within the maps seem to be directionally oriented. In

other words, the rate of change of the peak location within the susceptibility maps is higher in one direction than in the other. In fact, the direction of faster change is along the axis created by the three small inner chambers. This corresponds to the frequency-encoding gradient direction of the original acquisitions. Another interesting observation, which is clearly visible in Figure 44, is that the amount of shift in the water solution and in the corn oil solution are equal at their boundary in the frequency-encoding direction, but not in at the other boundaries between the two solutions. Both of these observations, along with the shape of the iso-lines with the susceptibility maps, indicate that there was a definite non-uniformity within the B_0 magnetic field through the chambered phantom at the time of data acquisition. Furthermore, these observations suggest that the magnetic field gradient was likely more concentrated at the edges of the phantom, which corresponded to the extremes in the frequency-encoding direction of the acquired MRI images.

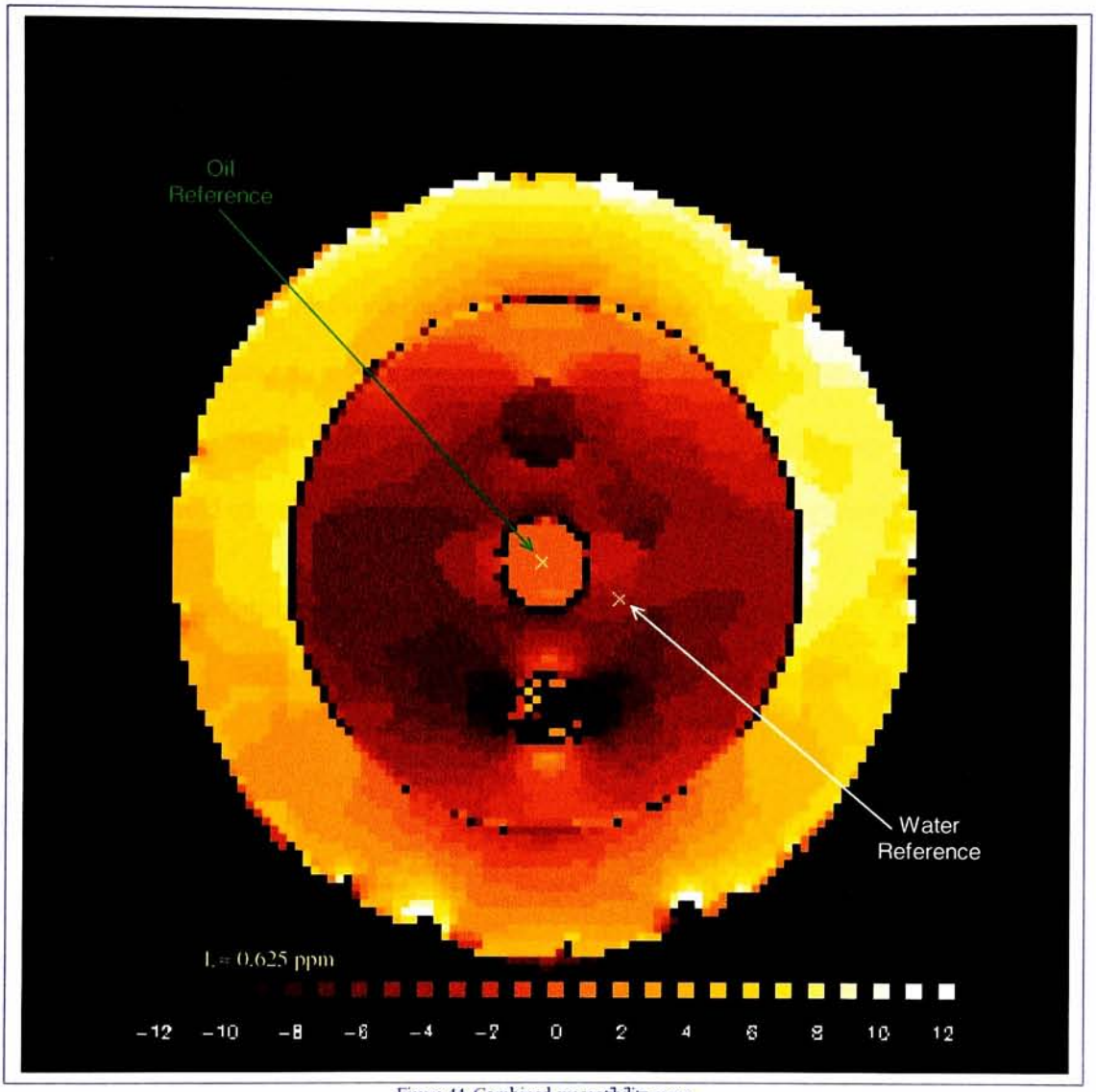

Figure 44 Combined susceptibility maps.

4.4 In Vivo

4.4.1 Data Acquisition

In addition to using phantoms to characterize the spatial-spatial-spectral technique being studied, *in vivo* tissue was also used to demonstrate the technique. In particular, an axial slice through the medial tibia of an adult male was imaged using the spatial-spatial-spectral technique in an effort to demonstrate the merits of the technique on actual tissues. This portion of the human leg was used as it contains both fat and muscle tissues and therefore the spatial-spatial-spectral data volume should contain spectra with both fat and water components, among others.

As with the phantom objects, a simple Spin Echo imaging sequence was used to acquire the *in vivo* data set. Table 8 lists the common acquisition parameters for the various projection images.

Table 8 In vivo acquisition parameters.

Parameter	Value
Repetition Time (TR)	1000 msec.
Echo Time (TE)	35 msec.
Field of View (FOV)	18cm x 18cm
Slice Thickness	1.0 cm
Image Size	256p x 512p
Acquisition Time	3:24.05 min

Again, a non-square number of samples were used in an effort to reduce the acquisition time required for the data collection. Another step taken toward reducing acquisition time for the overall data set was to limit the number of projection images to 20. Although this probably

impacted the results of the acquisition, which will be discussed in detail below, the quality is still sufficient to demonstrate the spatial-spatial-spectral technique.

As with the two phantom experiments, a new gradient and a new sampling bandwidth were chosen for each projection, while the other acquisition parameters mentioned above were kept constant. A total of 20 projection acquisitions were collected over a projection angle range of $-\pi/2 \leq \theta \leq \pi/2$ with $\Delta\theta = 9.0$ degrees. Table 4 contains the desired bandwidth (as calculated by equation 17), frequency-encoding gradient, and acquired bandwidth, all as a function of projection angle. Again, the acquired bandwidth was always larger than the desired bandwidth to allow for effective interpolation.

Table 9 Projection acquisition parameters associated with the *in vivo* acquisition.

Projection Angle θ (degrees)	Desired Bandwidth BW(θ) (kHz)	Freq.-Encoding Gradient G (G/cm)	Acquired Bandwidth BW'(θ) (kHz)[14]
-90.00	62500.000	-0.815458	62500.000
-81.00	3268.542	-0.042177	4032.258
-72.00	1656.335	-0.020560	4032.258
-63.00	1127.629	-0.013111	4032.258
-54.00	871.010	-0.009195	4032.258
-45.00	724.053	-0.006680	4032.258
-36.00	632.855	-0.004853	4032.258
-27.00	574.626	-0.003404	4032.258
-18.00	538.347	-0.002171	4032.258
-9.00	518.382	-0.001058	4032.258
0.00	512.000	0.000000	4032.258
9.00	518.382	0.001058	4032.258
18.00	538.347	0.002171	4032.258
27.00	574.626	0.003404	4032.258
36.00	632.855	0.004853	4032.258
45.00	724.053	0.006680	4032.258
54.00	871.010	0.009195	4032.258
63.00	1127.629	0.013111	4032.258
72.00	1656.335	0.020560	4032.258

[14] BW, in this context, is treated as the full bandwidth rather than the half-width (i.e. 31250kHz = ±15625kHz)

81.00	3268.542	0.042177	4032.258
90.00	62500.000	0.815458	62500.000

Figure 45 contains the $\pi/2$, or purely spatial, projection image. One should notice that the image appears to be a typical MRI acquisition. One other observation that can be made from Figure 45 is that there appears to be the presence of a motion artifact in the image. Indeed, this is true. No flow artifact suppression techniques were employed during the acquisition of the *in vivo* data, but the results do not appear to suffer due to impacts associated with the artifact.

In Figure 46, the 0 degree, or purely spectral, projection is displayed. This is obviously not a typical MRI image. One should note that there appears to be two distinct signals in the vertical direction of the image, which corresponds to the frequency direction. One of the signals is that from water spectral peaks, the other is from the fat spectral peak.

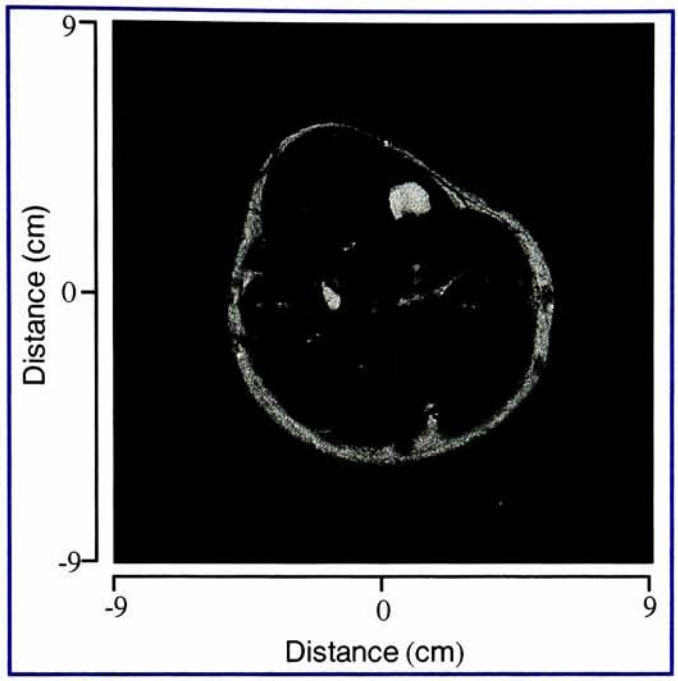

Figure 45 The $\pi/2$, or purely spatial, projection appears to be a typical MRI acquisition.

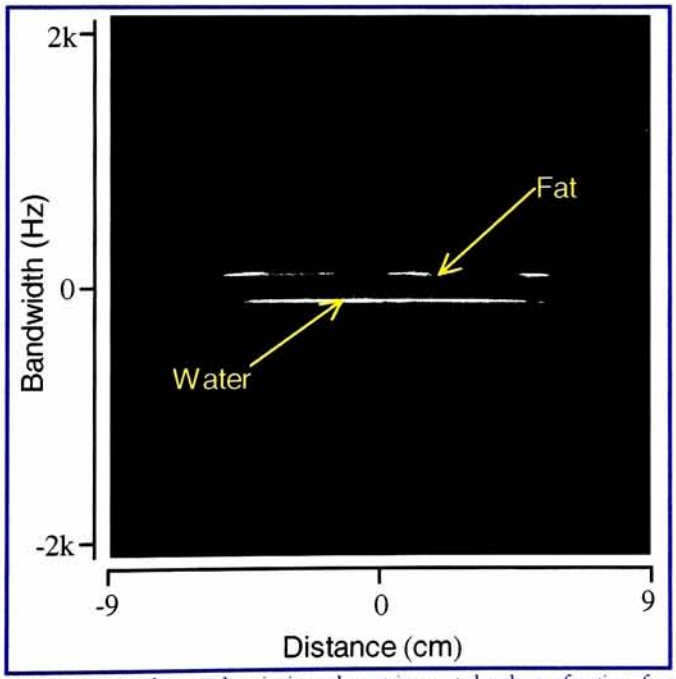

Figure 46 The 0 degree, or purely spectral, projection only contains spectral peaks as a function of spatial position.

4.4.2 Results

As was mentioned above, the low number of projection angles did impact the quality of the results in that there appears to be a significant amount of background noise as well as blurring in the detail of the data. Nevertheless, the spatial-spatial-spectral data volume that resulted from the *in vivo* data acquisition demonstrates that the technique has merit. This can be seen in Figure 47, Figure 48, and Figure 49. Each of the figures depicts a unique spectral, or chemical shift, plane through the spatial-spatial-spectral data volume. In the first of the three figures, Figure 47, bone marrow stands out as the strongest signal. In the next, Figure 48, the fatty tissues near the surface of the leg stand out more than any other. These two seem to make intuitive sense as bone marrow and fatty tissues should exhibit spectral signatures in which peaks are observed near the fat region of the chemical shift scale (i.e. 1.0-2.0 ppm, approximately).

Missing Page

In the final of the three figures, Figure 49, no one location seems to stand out more than others. In fact, it seems that the entire muscle area of the leg has approximately the same signal strength throughout. This also makes intuitive sense in that muscles contain a large water component and therefore the spectrum of muscle should exhibit a peak near the water chemical shift location. This is indeed true in this case as the spatial-spatial plane of Figure 49 was taken from the 5.09 ppm chemical shift location of the spatial-spatial-spectral data volume.

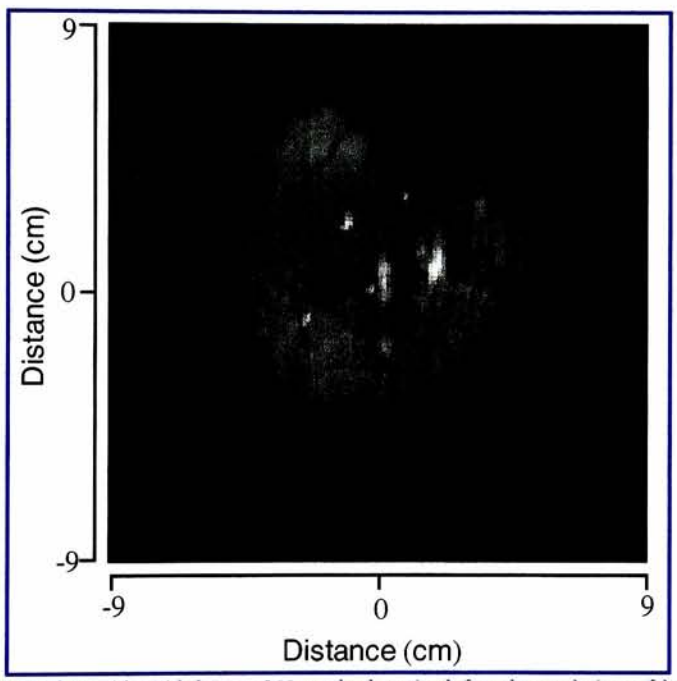

Figure 49 The spatial-spatial plane at ~5.09 ppm has large signals from the muscle tissue of the leg.

4.4.2.1 Three-Dimensional Surface Rendering

One last way in which to visualize the results obtained from the *in vivo* acquisition is depicted in Figure 50. As with the chambered phantom, a three-dimensional rendering of the spatial-spatial-spectral data volume is displayed. In the figure, one can fairly easily determine two primary chemical shift "planes": one for fat and one for water. Within the fat "plane" there is

signal from both surface fat tissue as well as bone marrow. The water "plane" contains signal primarily from the muscle tissue.

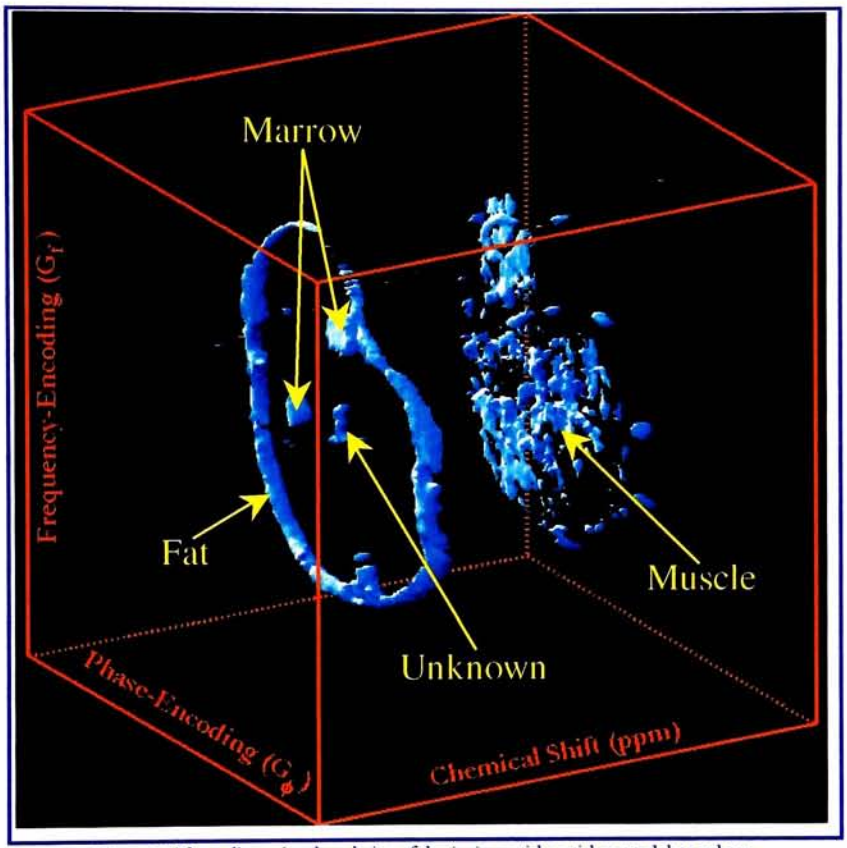

Figure 50 Three-dimensional rendering of the *in vivo* spatial-spatial-spectral data volume.

Chapter 5

5. Analysis

Yes, the technique works, but how well?

Typically it is not enough to demonstrate that a new imaging technique acquires data as it is designed to do. In addition, it is helpful to know how well the technique acquires data and how well might the data be used once it is acquired. Two simple analyses were used to get a handle on these issues. They include full width at half maximum measurements and classification accuracy measurements, both are discussed below.

5.1 Full Width at Half Max (FWHM) Measurements

Full width-at-half-maximum (FWHM) measurements are usually used as a gauge of the resolution of the imaging system being studied. In the case of the spatial-spatial-spectral imaging technique being studied, the FWHM measurements are used as an indicator of the sort of spectral resolution that can be expected from the technique.

One issue that must be discussed prior to presentation of FWHM measurements is the fact that spectral signatures rarely have infinitesimal width and therefore have an inherent FWHM regardless of the imaging system or technique being used to measure them. This concept is clearly demonstrated in the high-resolution NMR spectroscopy measurements presented in Figure

29. In the figure, each of the spectral peaks has a definite width. Therefore, the best achievable FWHM measurement value would equal the actual FWHM of the spectral peak being imaged.

5.1.1 T_2^* Discussion

Another factor that plays into the FWHM measurements, and how they are judged, is the manner in which the solution's actual spectra are measured. One would think that a high-resolution NMR spectrometer result would be ideal for such a situation. Unfortunately, this may not be entirely true because of the T_2^* differences between the NMR spectrometer and the MRI system upon which the spatial-spatial-spectral technique was employed.

If you will recall, the spin-spin relaxation time associated with a precessing magnetic moment is not only dependent upon the inherent relaxation time, but also upon the inhomogenieties of the magnetic field near that precessing magnetic moment. This is shown in equation 8. As one might expect, the $T_{2inhomo}$ value for a high-resolution NMR spectrometer is likely quite different than that of a clinical MRI system. Therefore, the standard to which the FWHM measurements taken from data acquired via the spatial-spatial-spectral technique ought not be derived from NMR spectra, but rather from spectra as measured by the clinical MRI system itself.

5.1.2 One Inch Diameter Spheres

On the clinical MRI system used to demonstrate the spatial-spatial-spectral technique, there is a command that allows one to measure, to a certain extent, the spectra of the object placed in the B_0 field. By limiting the object to a single solution, the spectrum of that solution is

measurable. One issue that has to be dealt with, however, is artifacting, such as susceptibility, that may influence, or alter, the apparent spectrum of the solution as it is being measured. In order to minimize susceptibility, in particular, relatively small, spherical containers were used to hold each solution while its spectrum was measured in the MRI system. There was one for each of the following solutions:

A. Aqueous solution of 50 mM $NiCl_2$ and Gadodiamide (Nycomed)
B. Corn Oil (same as in the chambered phantom)
C. Olive Oil (same as in the chambered phantom)
D. Aqueous 8 mM $NiCl_2$ (Water)
E. Ethanol [95%]
F. RM

Since only the water ($NiCl_2$) and RM solutions were common between the 3Tubes phantom and the MRI spectral measurements, only their spectral measurements are presented in Figure 51. One can readily see that the spectral peak locations are consistent with previously presented versions and that the width of the spectral signatures seems exaggerated as compared to those obtained via high-resolution NMR spectrometer (see Figure 51).

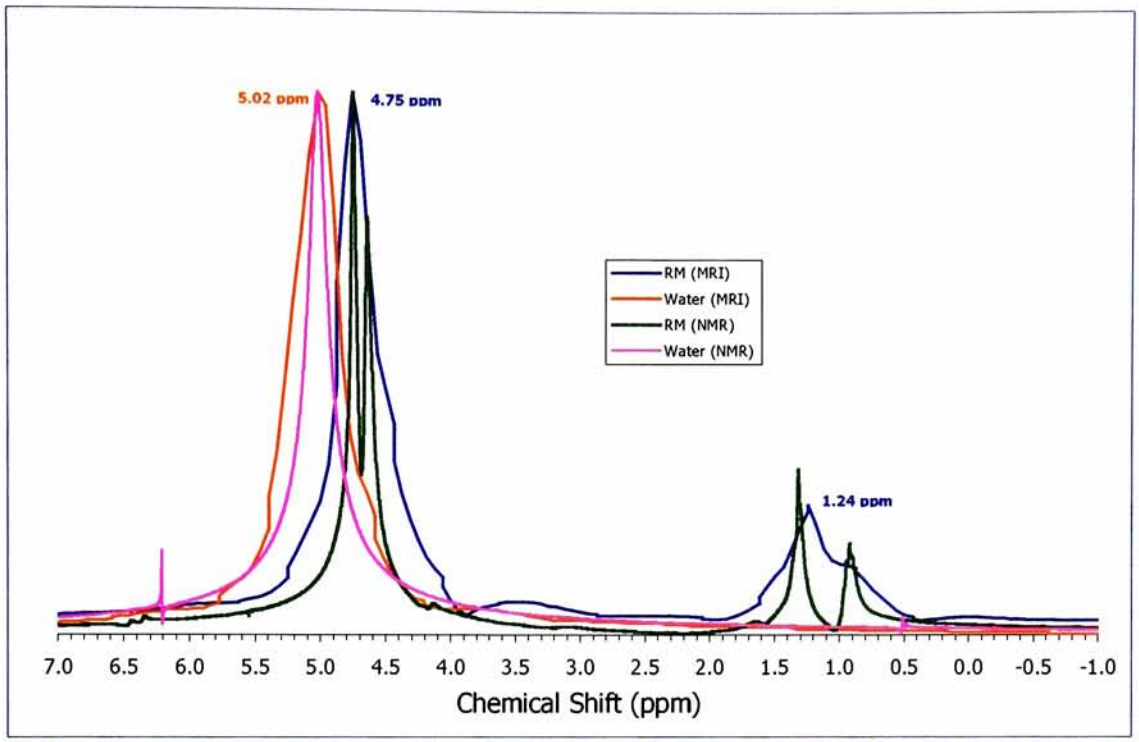

Figure 51 Water and RM solution spectra as measured by the clinical MRI system and an NMR spectrometer (signals normalized to single maximum).

The FWHM for the two solutions and the two measurement methods are numerically listed in Table 10. Obviously the NMR values are smaller and therefore more stringent in terms of a goal for the spatial-spatial-spectral technique. Therefore, all comparisons will be made against the MRI values.

Table 10 NMR and MRI FWHM measurements for water and RM.

Solution Peak	NMR FWHM[15] (ppm)	MRI FWHM[15] (ppm)
Water	0.2151	0.4345
RM A	0.0642	0.3611
RM B	0.0816	
RM C	0.0766	0.5811
RM D	0.1092	

[15] Four peaks were found in the NMR spectrum for the RM solution while only two were measurable via the MRI system.

5.1.3 3Tubes FWHM

Since the best results of the spatial-spatial-spectral technique seemed to come from the 3Tubes phantom experiments, the FWHM measurements were only performed on the spectral peaks in this spatial-spatial-spectral data volume. Figure 52 shows the original spatial-spectral plane that was shown in Figure 33 (with a 180 degree rotation in order to match the output orientation of the FWHM tool), but it also contains blow-up views of each of the three primary spectral peaks. Within each of these views, an automated FWHM measurement tool has indicated the FWHM for each line of data in the spatial direction and an average over those lines for that particular peak is provided within each image of the figure and in Table 11.

Table 11 Average calculated FWHM values using the 3Tubes data volume.

Spectral Peak	Average FWHM (ppm)
Water	0.2723
RM	0.2307
Decane	0.2464

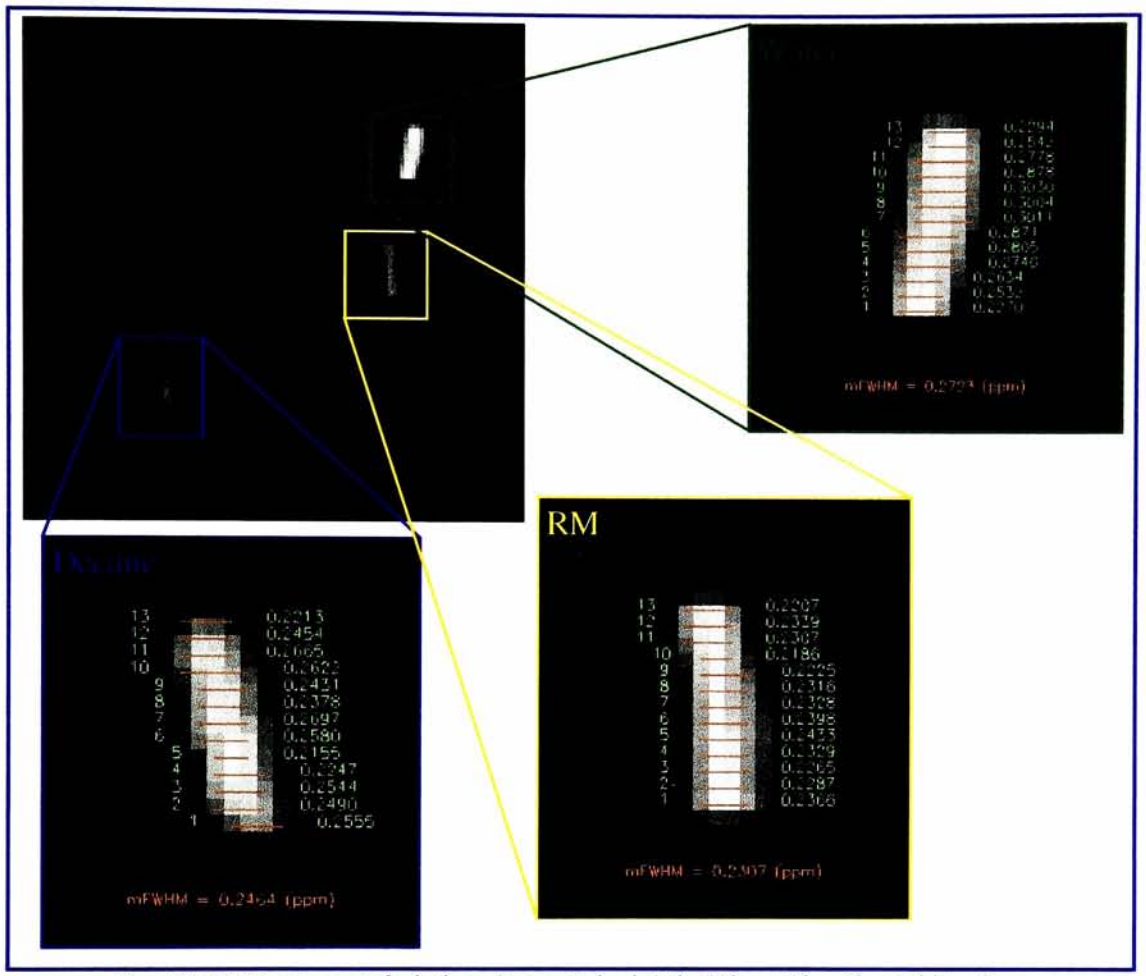

Figure 52 FWHM measurements for the three primary spectral peaks in the 3Tubes spatial-spatial-spectral data volume.

It is worth noting that the way in which the automated FWHM tool works is that it looks for the maximum peak value within the region of interest, which is user supplied. The tool will then start at that maximum value and proceed in the spatial directions, up and down in this case, until ½ of that maximum value is reached. Then, for each spatial line of data within these two half-power points, a FWHM will be calculated relative to the maximum of the particular spatial line that the tool is currently working on. The nice effects of this sort of FWHM tool are that the spectral peak does not have to be at a constant chemical shift location over its extent in the spatial

direction and the tool disregards the original object shape dependence upon the maximum peak value.

The observations to be made from Table 11 and Figure 52 are that the FWHM values, as calculated by the automated tool, are much better than those originally predicted by the MRI system measurements (see Table 10). While it is unclear as to the actual cause of this extra accuracy, it is possible that the acquisition parameters used during the spectrum measurements using the MRI system may not have matched those used during the spatial-spatial-spectral data acquisition. In particular, different TR, TE, or even flip angles could have been employed – each of which may have impacted the recorded signal and therefore the FWHM measurements in one way or another. Unfortunately, due to the way in which the spectra were measured using the clinical MRI system, the parameters used were not readily available and therefore remain a mystery.

5.1.3.1 Dependency upon # of projections

Since the acquisition step of the spatial-spatial-spectral technique requires a separate MRI image for each projection angle, the time required to acquire an entire 80-projection set is quite lengthy. In an effort to reduce the acquisition time a logical thought might be to reduce the number of projection angles. It may or may not be clear, but reducing the number of projection angles has a very dramatic affect on the final quality of the spatial-spatial-spectral data volume.

One way in which to gauge the effects of reducing the number of projection angles might be to calculate the FWHM of the spectral peaks, as was previously reported upon, for

reconstructions created with a variety of number of angles. This was accomplished by modifying the reconstruction tool to allow it to change the delta projection angle setting and thus omit every N projections while performing the back-projection procedure. For example, the tool would use every projection available for N=1, every other projection angle for N=2, every third for N=3, and so on. The other modification made to the back-projection tool was to modify the starting projection. This was done because with particular values of N, it is possible to omit all of the nearly purely spatial projections. Therefore, a starting offset value was implemented.

Table 12 holds the results of the FWHM measurements for the water peak for a wide variety of combinations of offset and delta projection angle. Figure 53 is a surface plot of the data held in Table 12.

Table 12 Water peak FWHM measurements for a variety of back-projection angle offset and delta values.

		Offset					
		0	1	2	3	4	5
Delta	1	0.27	0.14	0.14	0.14	0.13	0.13
	2	0.14	0.13	0.15	0.13	0.14	0.13
	3	0.15	0.15	0.15	0.15	0.14	0.14
	4	0.16	0.14	0.16	0.14	0.15	0.14
	5	0.20	0.14	0.17	0.16	0.17	0.18

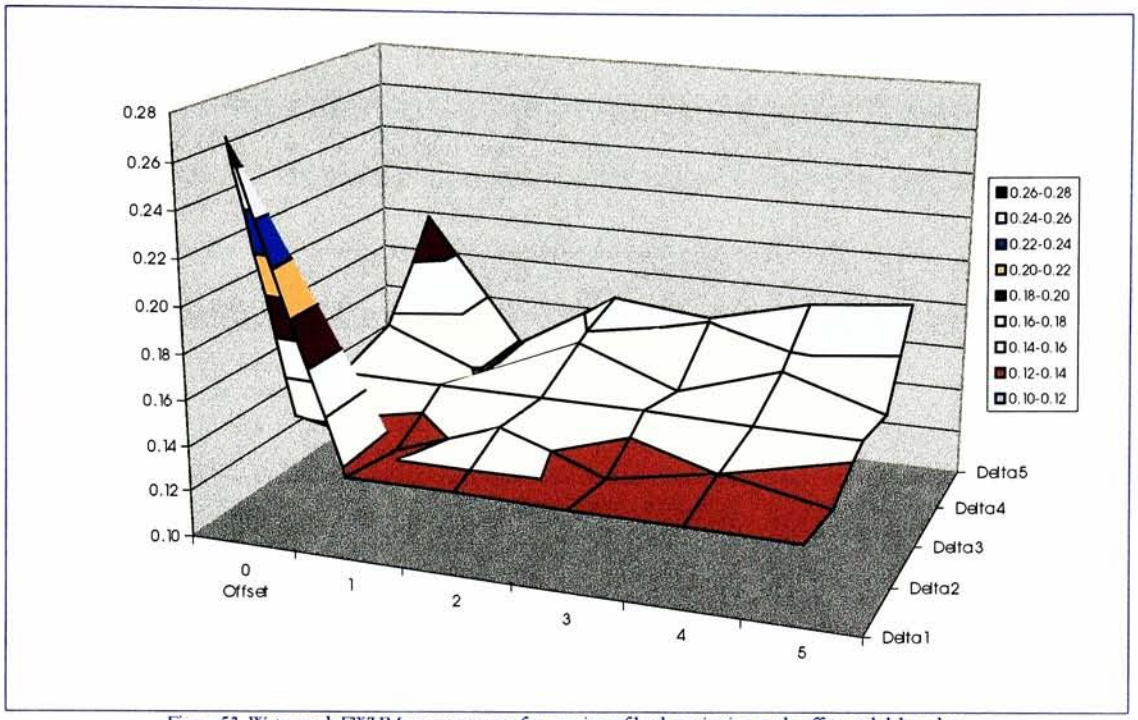

Figure 53 Water peak FWHM measurements for a variety of back-projection angle offset and delta values.

The first thing that jumps out from Figure 53 is the fact that using all of the projections, offset=0 and delta=1, produces the worst FWHM of the set. Keep in mind that the FWHM measurements were only calculated for the spectral extent of the water solution peaks and that due to the way in which the back-projection reconstruction works, including a purely spatial projection will tend to broaden the spectral peaks of the spatial-spectral plane being reconstructed. Therefore, the relatively large FWHM measurement may be a bit misleading without also somehow indicating the spatial accuracy of the reconstructed spatial-spectral plane.

Also of note in Figure 53 is that as the number of projection angles lessen, the FWHM measurements don't necessarily increase, as one would expect. In fact, the water peak FWHM actually gets better when the number of projections is cut in half and then steadily worsens with

fewer projections. Reviewing the spatial-spectral planes created by fewer and fewer projection angles tell a very different tale, however. Figure 54 contains 6 images of the spatial-spectral plane depicted in Figure 33. The number below each of the images in Figure 54 represents the number of projection angles used to reconstruct the spatial-spatial-spectral data volume. It is clear from Figure 54 that including as many projection angles as possible in the reconstruction procedure is nothing short of necessary.

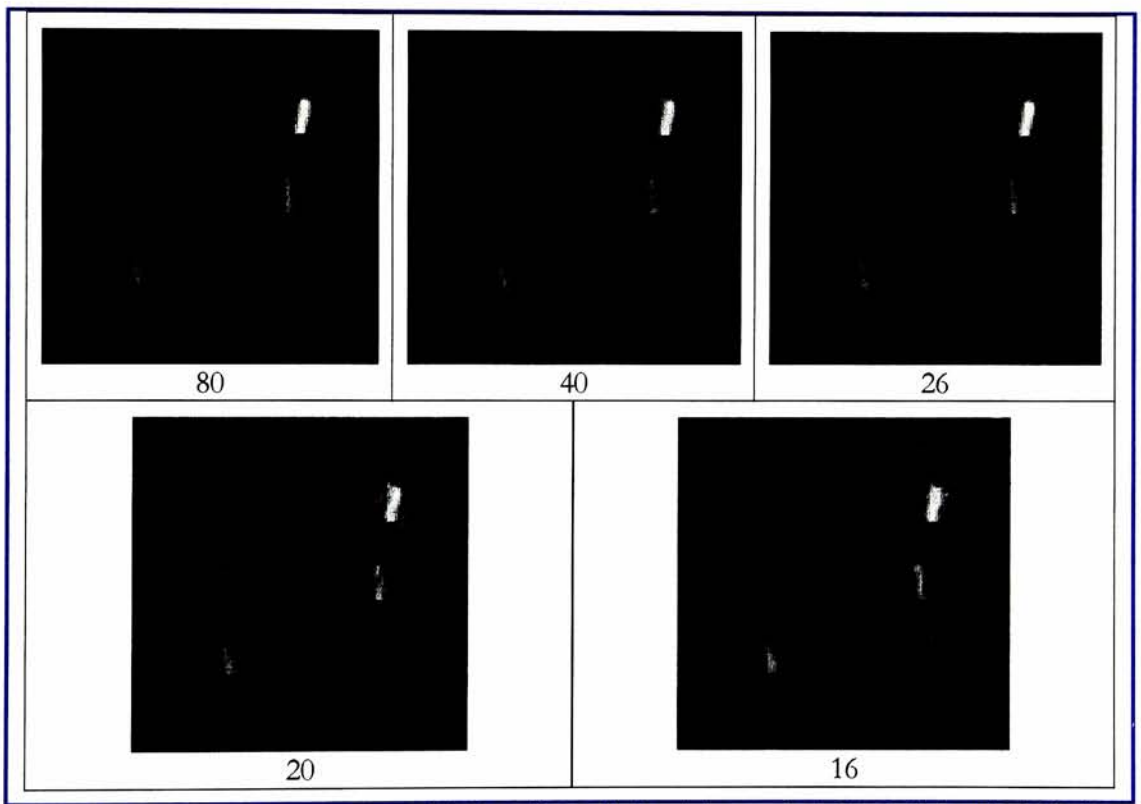

Figure 54 Including fewer and fewer projection angles in the spatial-spectral back-projection procedure is obviously detrimental to final quality.

5.1.3.2 Expected FWHMs

In order to get an idea of the expected FWHM values, a simulation of the spatial-spectral imaging technique was developed. The simulation was designed to simulate the data acquisition

and post-processing for a single spatial-spectral plane with the assumption that multiple planes would follow accordingly. Several assumptions were made in developing the simulation:

- First, variations in the B_0 magnetic field were not simulated. In other words, the B_0 magnetic field was assumed to be perfectly homogeneous over the full extent of the object being imaged.

- Likewise, the magnetic field gradients were assumed to be perfectly linear and well-behaved gradients over the entire extent of the object being imaged.

- Signal-to-Noise was assumed to be constant across all projections. In the actual acquisitions, signal-to-noise fell off with increases in sampling bandwidth. This affect was not simulated.

- The spatial distribution of the B_1 magnetic field was assumed to be perfectly constant. In other words, there were no variations in the transmit or receive field. This means that each B_1 application produced 90-degree or 180-degree rotations in the magnetic moment, exactly, over the full extent of the object being imaged. It also indicates that the receive coil was equally sensitive across the entire sample.

- There were no standing wave or conductivity artifacts included in the smulation.

- Finally, the simulation assumed no residual magnetization was carried over between repetition time periods.

The simulation used the $NiCl_2$ and RM spectra, as measured by the MRI system using the one-inch spheres (see Figure 51), as input spectra. The simulation then assumed spatial locations for these spectra that mimicked the spatial location of the 3Tubes phantom for the center spatial-spectral plane of the data volume (see Figure 33). The simulation then reconstructed the spatial-spectral plane by working through the following steps:

- 512-sample projections were created at 2.25-degree increments, using the same projection sampling bandwidths that were used in the 3Tubes experiment (see Table 4).
- 128-sample interpolations were performed to convert the projections with the acquired sampling bandwidths to projections with the desired sampling bandwidths, as calculated by equation 17.
- A filtered back-projection was performed using the interpolated data to reconstruct the spatial-spectral plane. A 65-point Ram-Lak filter was used in the procedure.
- The number of projections was varied such that all of the acquired projections were used in the reconstruction process (80 projections), then another reconstruction was performed using every other projection (40 projections), then every third projection was used (26 projections), and finally every fourth projection was used (20 projections).
- Average FWHM measurements were made using the single $NiCl_2$ and two RM peaks for each of the reconstructions discussed. Individual FWHM measurements were made for each spatial location over the extent of the peaks and then these individual values were averaged together to result in a single FWHM value for each peak for each reconstruction.

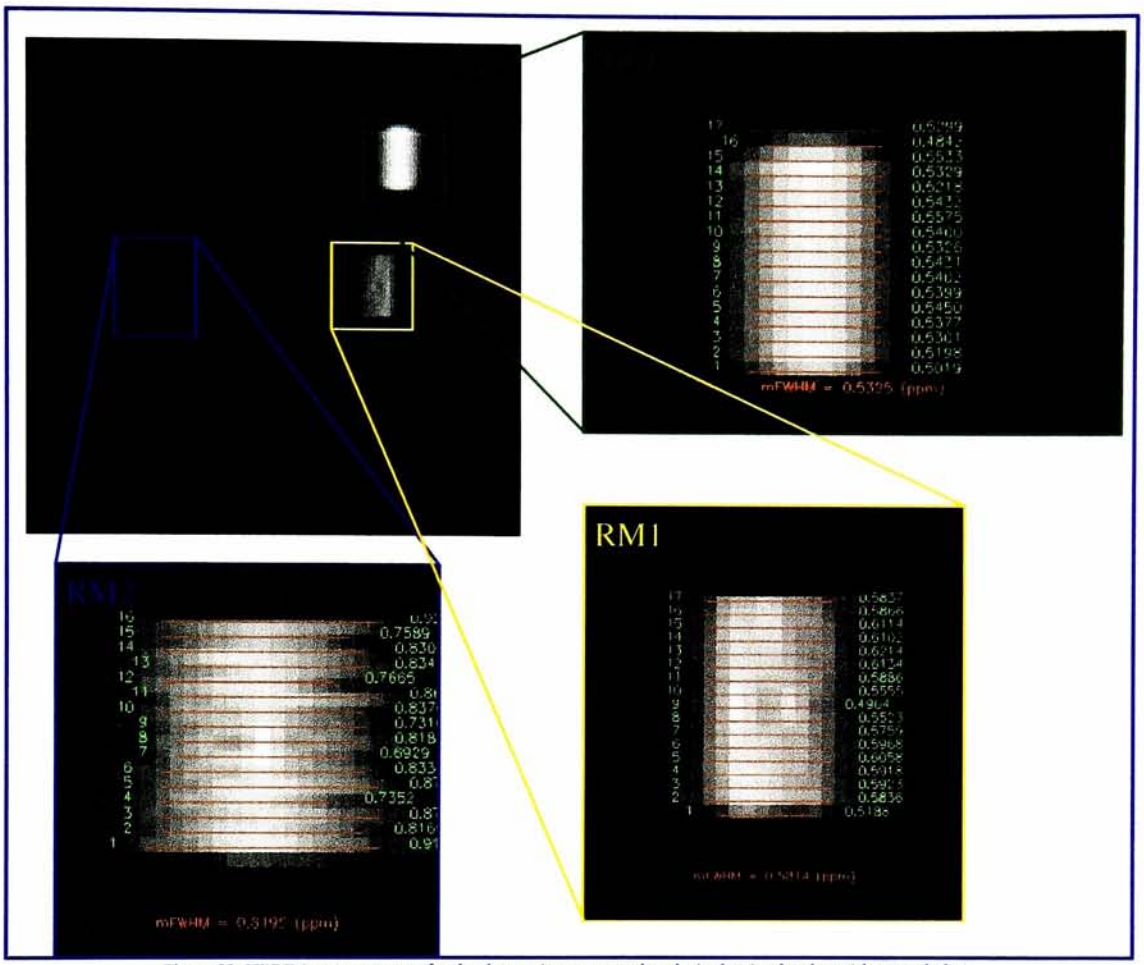

Figure 55 FWHM measurements for the three primary spectral peaks in the simulated spatial-spectral plane.

Figure 55 depicts the FWHM measurements made on the three spectral peaks of the spatial-spectral plane that was reconstructed using all 80 projections. This set of measurements was repeated on the spatial-spectral planes that were reconstructed using variations of the number of projection angles (see Figure 56).

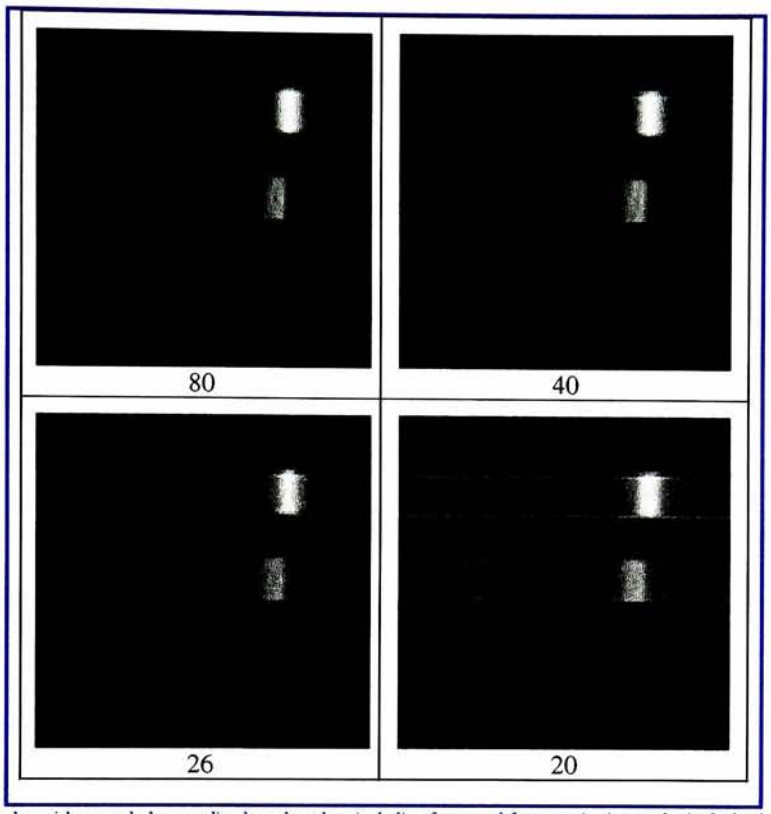

Figure 56 The simulated spatial-spectral plane quality degrades when including fewer and fewer projection angles in the back-projection procedure.

The FWHM measurements made using the simulation data are listed in Table 13. The values in the column marked "Original" in this table represent the FWHM measurements made using the spectra obtained via the MRI system with the one-inch spheres. These values should be considered as "truth" for this set of simulations. Next, FWHM values were not measured for the lower RM peak (referred to as RM2) for the 26- and 20-projection angle cases due to the significantly low signal-to-noise ratio for this peak, which can be observed in the spatial-spectral reconstructions of Figure 56. The low signal-to-noise ratio essentially precluded FWHM measurements. Finally, the FWHM values listed in each of the remaining columns are the respective measurements made on the spatial-spectral planes resulting from fewer and fewer

projection angles. One can see that as more and more projection angles are omitted from the reconstruction process, the FWHM for each of the spectral peaks becomes wider and wider. This indicates worse and worse spectral resolution. The exception to this observation is for the water peak measurement for the 26-projection angle case. This FWHM value seems to buck the trend just discussed. Review of the spatial-spectral reconstructions of Figure 56 indicates that the water peak of the 26-projection angle case seems to be hourglass shaped due to the radial artifacting present in the reconstructions. Therefore, although some of the FWHM measurements are probably representative of the true FWHM measurement for this case, many are somewhat narrower than the true value. This "pulls" the average value down below the true value creating an exception to the trend.

Table 13 FWHM measurements for a variety of numbers of projection angle for each of the three spectral peaks in the simulations.

		Projection Angles used in reconstruction			
Peak	Original	80	40	26	20
Water	0.4346	0.5325	0.5270	0.4403	0.5760
RM1	0.3334	0.5814	0.5924	0.5982	0.6127
RM2	0.5783	0.8195	0.8759	N/A	N/A

Based upon the observations and measurements made using the simulated spatial-spectral reconstructions, one can conclude that the spatial-spatial-spectral imaging technique reconstructs the underlying spectral signatures, albeit at a reduced spectral accuracy than the clinical MRI system is capable of measuring. The spatial accuracy also suffers by a small amount. FWHM measurements were also made in the spatial dimension for the three peaks of the 80-projection angle reconstruction. The spatial dimension growth was calculated at <2.5% in each direction for all of the spectral peaks.

One should be careful when comparing these FWHM values to those reported in sections 5.1.3 and 5.1.3.1 as the FWHM values reported in Table 13 are based upon a simulation that used the one-inch sphere spectral measurements as input. And, the one-inch sphere spectral measurements may have used slightly different imaging parameters (i.e. TE, TR, etc.) than were used during the 3Tubes experiment. It is not known what the imaging parameters were for the one-inch sphere spectral measurements since a MRI system diagnosis tool was used to make these measurements and therefore the parameters were not readily available for recording purposes.

5.2 Classification Analysis

One way in which spatial-spatial-spectral volumes of data will likely be used in the future is as input information to tissue identification, or classification, routines. Therefore, it makes sense to use such a routine as a generalized metric to indicate how well the spatial-spatial-spectral imaging technique creates data volumes that are useful. The results of using a parallelpiped classification tool to segment the spatial-spatial-spectral volumes that result from the technique being studied are presented below. Also presented are the results of a more manual approach in which particular spectral planes were used in a histogram segmentation method for classifying data volumes into object types.

5.2.1 3Tubes Classification

While trying to take advantage of current techniques and tools, a general parallelpiped classification technique was used to classify the 3Tubes data volume. The tool is part of a larger software package referred to as the Environment for Visualizing Images (ENVI) [45]. The

package is essentially a collection of remote sensing related tools for manipulating and analyzing panchromatic, multispectral, and hyperspectral data sets. Therefore, the tool was already set up to deal with a data volume such as that resulting from the spatial-spatial-spectral imaging technique being studied.

The first step in the procedure of classifying the spatial-spatial pixels in the data volume as belonging to one class, or object, or another was to train the classification tool by selecting pixels that are known to belong to that object type. Then, the trained tool takes that information and tries to assign each spatial-spatial pixel in the data volume to a particular object based on the spectral characteristics of the pixels provided during the training. The parallelpiped classification method is one of the more simplistic ones in that it attempts to construct parallelpipeds around clusters of data points in multi-dimensional histograms in order to segment the data volume into distinct object types.

There are two primary manners in which one can judge the results of the parallelpiped classification. The first is by viewing the resulting class map. The other is by examining the resulting confusion matrices. Class maps are usually color-coded, two-dimensional, spatial-spatial images in which each color represents a unique class or object type. Several example class maps are provided in Figure 57. In the figure, pixels classified as RM are colored green; water pixels are red; decane are blue; and unclassified pixels are black.

Missing Pages

From: 121

To : 145

Equation 32

$$\hat{f}(x,y) = \int_0^{\pi}\int_{-\infty}^{\infty} p_\theta(t)\delta[x\cos(\theta) + y\sin(\theta) - t]dtd\theta$$

Or, in polar coordinates:

Equation 33

$$\hat{f}(\rho,\phi) = \int_0^{\pi}\int_{-\infty}^{\infty} p_\theta(t)\delta[\rho\cos(\theta - \phi) - t]dtd\theta$$

As was shown above

Equation 34

$$p_\theta(t) = \delta(t)$$

by substitution we have

Equation 35

$$\hat{f}(\rho,\phi) = \int_0^{\pi}\int_{-\infty}^{\infty} \delta(t)\delta[\rho\cos(\theta - \phi) - t]dtd\theta$$

Because of the first $\delta(t)$ in the equation, the whole inner integral collapses as it is only non-zero at t=0. Therefore, what remains is:

Equation 36

$$\hat{f}(\rho,\phi) = \int_0^{\pi} \delta[\rho\cos(\theta - \phi)]d\theta$$

Now, we have to rely on a definition provided in Gaskill [37]:

Equation 37

$$\delta(f(\theta)) = \sum_n \frac{\delta(\theta - \theta_n)}{|f'(\theta_n)|}$$

where θ_n are the roots of $f(\theta)=0$ and the denominator is the 1st derivative of $f(\theta)$ evaluated at $\theta=\theta_n$. The only value of θ that satisfies this relationship that lies within the 0 to π range, which are the limits of integration in the above back-projection equation, are at $\theta_n=\phi+\pi/2$. Using this information, we arrive at::

Equation 38

$$f(\theta)=\rho\cos(\theta-\phi)$$

Equation 39

$$f'(\theta)=\frac{d\rho}{d\theta}\cos(\theta-\phi)=-\rho\sin(\theta-\phi)$$

Equation 40

$$f'(\theta=\phi+\frac{\pi}{2})=-\rho\sin(\theta-\phi)\Big|_{\theta=\phi+\frac{\pi}{2}}=-\rho\sin(\phi+\frac{\pi}{2}-\phi)=-\rho$$

Equation 41

$$\left|f'(\theta)\right|=\rho$$

Equation 42

$$\delta(f(\theta))=\sum_{n=1}^{1}\frac{\delta[\theta-(\phi+\frac{\pi}{2})]}{\rho}=\frac{\delta[\theta-(\phi+\frac{\pi}{2})]}{\rho}$$

Equation 43

$$\hat{f}(\rho,\phi)=\int_0^{\pi}\frac{\delta[\theta-(\phi+\frac{\pi}{2})]}{\rho}d\theta=\frac{1}{\rho}$$

Equation 44

$$\hat{f}(\rho,\phi)=\frac{1}{\rho}$$

which is clearly different than the original object. In other words, the point spread function of the back-projection procedure is a smear factor that falls-off radially with increased distance. Another way to represent the effects of back-projection is in terms of the original object:

Equation 45

$$\hat{f}(\rho,\phi) = \frac{1}{\rho} ** f(\rho,\theta)$$

By employing the convolution theorem, we know that the Fourier space representation of the estimated object is:

Equation 46

$$\hat{F}(u,v) = \frac{1}{\omega} F(u,v)$$

This make compensating for the effects of back-projection relatively straightforward. In fact, it is as simple as multiplying the Fourier Transform of the back-projection result by ω:

Equation 47

$$F(u,v) = \omega \hat{F}(u,v)$$

The nice part about this is that w is well defined and relatively easy to implement. It can be shown, via the Central Slice Theorem, that the Fourier Transform of a projection, $F\{p_\theta(t)\}$, through the original object, f(x,y), at a particular angle θ is equivalent to the 1D slice through the Fourier Transform of the object at the same angle, $F_\theta(u,v)$. Therefore, we can restate the back-projection equation as follows:

Equation 48
$$\hat{f}(x,y)=\int_0^{\pi}\int_{-\infty}^{\infty} p_{\theta_i}(t)\delta[x\cos(\theta)+y\sin(\theta)-t]dtd\theta$$

Equation 49
$$\hat{f}(x,y)=\int_0^{\pi}\int_{-\infty}^{\infty}\left[\int_{-\infty}^{\infty} F_\theta(\omega)e^{i2\pi\omega t}d\omega\right]\delta[x\cos(\theta)+y\sin(\theta)-t]dtd\theta$$

Equation 50
$$\hat{f}(x,y)=\int_0^{\pi}\int_{-\infty}^{\infty}\frac{F_\theta(\omega)}{|\omega|}e^{i2\pi\omega(x\cos(\theta)+y\sin(\theta))}|\omega|d\omega d\theta$$

Equation 51
$$\hat{f}(x,y)=\frac{f(x,y)}{|\omega|}$$

Equation 52
$$f(x,y)=\hat{f}(x,y)|\omega|$$

which is exactly what we saw earlier. The issue that this points out is the fact that if we trace this back to the original back-projection equation, then we can see that if we manipulate the projections correctly, then we can compensate for the $|\omega|$ difference between the original object and the back-projection estimate of the original object. This can be accomplished by convolving each projection with a compensation filter of by multiplying the Fourier Transform of each projection with a compensation filter. Let's look at the convolution filter version as a starting point.

Since

Equation 53

$$p_\theta(t) \xleftrightarrow{FT_{1D}} F_\theta(\omega)$$

Let's define

Equation 54

$$Q_\theta(t) \xleftrightarrow{FT_{1D}} F_\theta(\omega)|\omega|$$

Therefore

Equation 55

$$Q_\theta(t) = P_\theta(t) ** k(t)$$

where k(t) is an unknown convolution filter designed to compensate for the back-projection PSF. To define k(t), let's look first at the function K(ω), which we know already to be $|\omega|$. This function can be defined over a finite width, $^{+}$- ω_0, according to Gaskill [37] function definitions as

Equation 56

$$K(\omega) = |\omega| \mathrm{Re}ct\left(\frac{\omega}{2\omega_0}\right)$$

which can also be written as

Equation 57

$$K(\omega) = \omega_0 \mathrm{Re}ct\left(\frac{\omega}{2\omega_0}\right) - \omega_0 Tri\left(\frac{\omega}{\omega_0}\right)$$

Taking the Fourier transform we get

Equation 58

$$k(t) = \omega_0\left[2\omega_0 Sinc(2\omega_0 t) - \omega_0 Sinc^2(\omega_0 t)\right]$$

Substituting $1/2\tau$ for ω_0 and sampling this function at $t=n\tau$, we get

Equation 59

$$k(n\tau) = \frac{1}{2\tau^2} Sinc(n) - \frac{1}{4\tau^2} Sinc^2\left(\frac{n}{2}\right)$$

Or,

Equation 60

$$k(n\tau) = \begin{cases} \frac{1}{4\tau^2} & if\ n = 0 \\ 0 & if\ n = even \\ \frac{-1}{n^2\pi^2\tau^2} & if\ n = odd \end{cases}$$

This filter is referred to as the Ram-Lak filter based on the name of its creators Ramachandran and Lakshminarayanan [7]. When plotted, $k(n\tau)$ looks like this, for $\tau=1$:

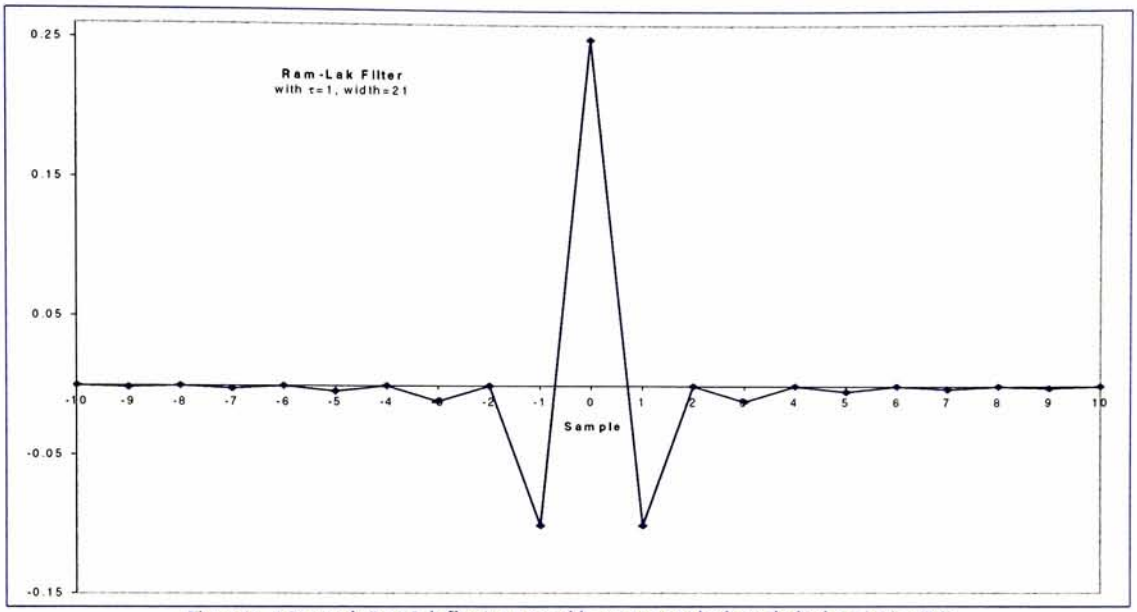

Figure 64 A 21 sample Ram-Lak filter is a reasonable one to use to back out the back-projection PSF.

There are three other widely used filters, and probably many more not so widely used filters. These three are the Shepp-Logan, the LowPass Cosine, and the Generalized Hamming filters:

Shepp-Logan:

Equation 61

$$K(\omega) = |\omega| Sinc\left(\frac{\pi\omega}{\omega_0}\right) \mathrm{Re}ct\left(\frac{\omega}{2\omega_0}\right)$$

Lowpass Cosine:

Equation 62

$$K(\omega) = |\omega| \cos\left(\frac{\pi\omega}{\omega_0}\right) \mathrm{Re}ct\left(\frac{\omega}{2\omega_0}\right)$$

Generalized Hamming:

Equation 63

$$K(\omega) = |\omega| \left[0.54 + (1 - 0.54) \cos\left(\frac{2\pi\omega}{\omega_0} \right) \right] \mathrm{Rect}\left(\frac{\omega}{2\omega_0} \right)$$

Here is a comparison of the frequency domain representation of the four primary filters:

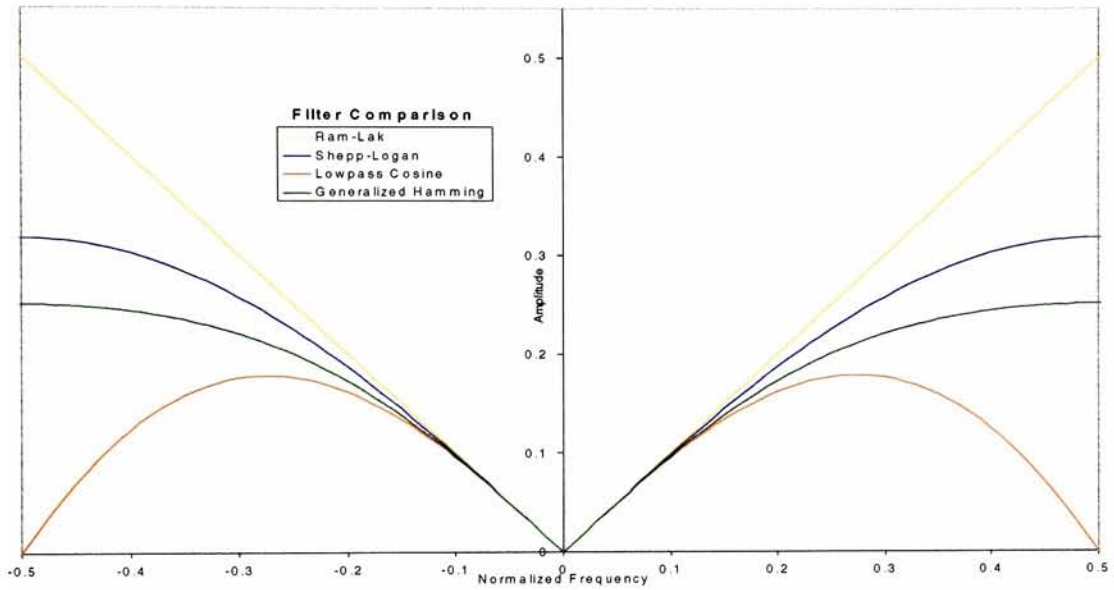

Appendix

B

Appendix B: Spin-Echo Imaging

A short overview of one of the more prevalent imaging protocols.

One of the most basic imaging protocols used by MRI systems is the spin-echo imaging protocol. The fundamental basis for the protocol is the 90°-FID sequence, but the spin-echo protocol adds a slight, albeit important, twist. In an effort to reduce acquisition times, the spin-echo protocol creates an *echo* of the 90°-FID signal, which is also recorded and placed into k-space. In fact, multiple echoes can be created and then recorded, which further reduces imaging times.

The theory of the spin echo protocol is based upon that of the 90°-FID, or saturation recovery, imaging protocol that has already been discussed. Recall that for the 90°-FID protocol, the net magnetic moment, which is initially aligned with the B_0 magnetic field, is rotated down to the transverse plane by applying B_1 for an appropriate length of time. Once the magnetic moment has been rotated and the B_1 field has been removed, the net magnetic moment begins to realign with the B_0 magnetic field. At the same time, the individual magnetic moments, which are precessing in the transverse plane, begin to de-phase. Since the dephasing occurs rather quickly relative to realignment with the B_0 field, components of the individual magnetic moments remain

in the transverse plane for quite some time after dephasing has reduced the signal to unrecordable levels. The spin-echo protocol takes advantage of the fact that magnetic moments continue to precess in the transverse plane even after they have dephased. The signal produced by the net magnetic moment in the transverse plane can be restored to recordable levels by forcing the individual magnetic moments to rephase. The rephrasing produces a duplicate, or echo, of the first signal produced.

Remember that the dephasing is caused by the fact that the individual magnetic moments precess in the transverse plane at slightly different rates. Although they are all precessing, the individual magnetic moments spread-out in the transverse phase because some precess faster than the average and some precess slower. The faster magnetic moments get "ahead" of the rest while the slower ones fall behind. This process is depicted pictorially in Figure 11.

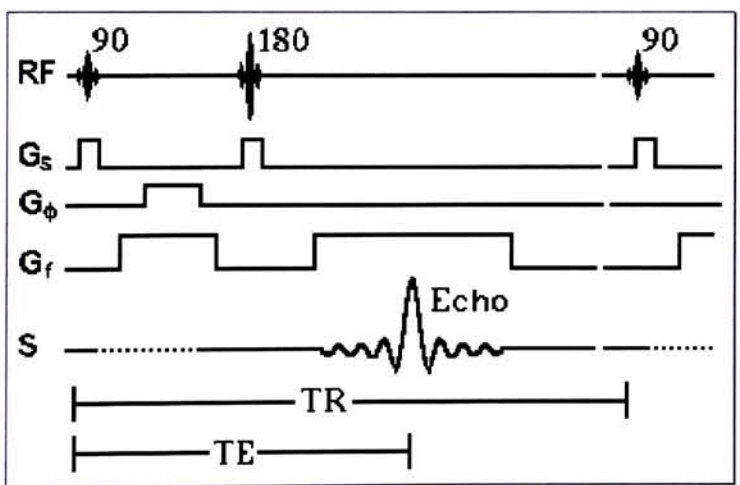

Figure 65 A basic Spin-Echo timing diagram (or pulse sequence). Use with permission [3].

By applying another rotation-inducing B_1 magnetic field – this one corresponding to a 180° rotation – one is able to flip all of the precessing magnetic moments such that the slower

magnetic moments are ahead of the others and the faster magnetic moments are behind. Under these circumstances, the faster magnetic moments will "catch up" to the rest at the same time as the slower ones fall back. When this happens, the individual magnetic moments are rephased and the original signal is restored and then begins to decay again as the slower moments fall behind and the faster moments get ahead. The spin-echo timing diagram is presented in Figure 65.

In the figure, the first line represents the relative timing of the B1-inducing radio frequency (RF) pulse used to rotate the precessing magnetic moments (the number next to each indicates the rotation angle induced). There are also three gradients depicted (G_s, G_ϕ, and G_f), which represent the slice selection gradient, the phase-encoding gradient and the frequency-encoding gradient, respectively. The line labeled "S" in the figure describes the recordable signal. Finally, there are two timing reference lines at the bottom of the figure. The first depicts the length of the repetition time (TR); the other is for the echo time (TE). TR and TE are timing parameters that are fundamental to the spin-echo imaging protocol.

One spin-echo characteristic that is not necessarily depicted in Figure 65 is the fact that the amplitude of each echo signal is reduced due to the T_1 signal decay phenomena discussed in section 2.1.6. The spin echo sequence relies upon the fact that individual magnetic moments continue to precess in the transverse plane even after they have dephased and that applying the 180° B1 field can rephrase them. Since the T_1 signal decay is occurring simultaneously, it is essentially reducing the amount of the net magnetic moments that remain in the transverse plane and therefore is reducing the net signal level, even when the individual magnetic moments have

rephrased. Even though there is an echo-to-echo signal decay, spin-echo imaging has provided a means of speeding the imaging process and is therefore used quite frequently.

Appendix C

Appendix C: Imaging Parameters

Specific imaging parameters were used to acquire data using the clinical MRI system.

A complete listing of the parameters used during the data acquisition phase of the project are presented here for each of the phantom experiments: the 3Tubes phantom and the chambered phantom. The imaging parameters used to acquire data for the *in vivo* experiment is also presented.

3Tubes Phantom Collection Parameters

Table 26 Acquisition parameters used for the 3Tubes phantom.

Projection Angle θ (degrees)	Desired Bandwidth BW(θ) (kHz)	Freq.-Encoding Gradient G (G/cm)	Acquired Bandwidth BW'(θ) (kHz)	Converted MRI Output Filename
-177.75	512.395	-0.001180	4032.258	e8576s3i63.bin
-175.50	513.583	-0.002370	4032.258	e8576s3i22.bin
-173.25	515.573	-0.003560	4032.258	e8576s3i62.bin
-171.00	518.380	-0.004760	4032.258	e8576s3i23.bin
-168.75	522.028	-0.005980	4032.258	e8576s3i61.bin
-166.50	526.544	-0.007220	4032.258	e8576s3i24.bin
-164.25	531.967	-0.008480	4032.258	e8576s3i60.bin
-162.00	538.341	-0.009770	4032.258	e8576s3i25.bin
-159.75	545.720	-0.011090	4032.258	e8576s3i59.bin
-157.50	554.171	-0.012450	4032.258	e8576s3i26.bin
-155.25	563.771	-0.013860	4032.258	e8576s3i58.bin
-153.00	574.610	-0.015320	4032.258	e8576s3i27.bin
-150.75	586.796	-0.016830	4032.258	e8576s3i57.bin
-148.50	600.456	-0.018420	4032.258	e8576s3i28.bin
-146.25	615.739	-0.020090	4032.258	e8576s3i56.bin
-144.00	632.821	-0.021840	4032.258	e8576s3i29.bin
-141.75	651.910	-0.023700	4032.258	e8576s3i55.bin
-139.50	673.257	-0.025670	4032.258	e8576s3i30.bin
-137.25	697.159	-0.027790	4032.258	e8576s3i54.bin

-135.00	723.978	-0.030060	4032.258	e8576s3i31.bin
-132.75	754.150	-0.032520	4032.258	e8576s3i53.bin
-130.50	788.214	-0.035200	4032.258	e8576s3i32.bin
-128.25	826.833	-0.038130	4032.258	e8576s3i52.bin
-126.00	870.841	-0.041380	4032.258	e8576s3i33.bin
-123.75	921.294	-0.044990	4032.258	e8576s3i51.bin
-121.50	979.551	-0.049060	4032.258	e8576s3i34.bin
-119.25	1047.392	-0.053680	4032.258	e8576s3i50.bin
-117.00	1127.186	-0.059000	4032.258	e8576s3i35.bin
-114.75	1222.169	-0.065210	4032.258	e8576s3i49.bin
-112.50	1336.863	-0.072570	4032.258	e8576s3i36.bin
-110.25	1477.797	-0.081480	4032.258	e8576s3i48.bin
-108.00	1654.746	-0.092520	4032.258	e8576s3i37.bin
-105.75	1883.033	-0.106590	4032.258	e8576s3i47.bin
-103.50	2188.109	-0.125210	4032.258	e8576s3i38.bin
-101.25	2615.518	-0.151130	4032.258	e8576s3i46.bin
-99.00	3255.486	-0.189800	4032.258	e8576s3i39.bin
-96.75	4314.776	-0.253980	7353.000	e8576s3i45.bin
-94.50	6388.419	-0.381960	7353.000	e8576s3i40.bin
-92.25	12035.688	-0.700000	13889.000	e8576s3i42.bin
-90.00	31250.000	1.834780	31250.000	e8576s3i41.bin
-87.75	12037.765	0.700000	13889.000	e8576s3i43.bin
-85.50	6389.038	0.381960	7353.000	e8576s3i3.bin
-83.25	4315.061	0.253980	7353.000	e8576s3i44.bin
-81.00	3255.648	0.189800	4032.258	e8576s3i4.bin
-78.75	2615.622	0.151130	4032.258	e8576s3i81.bin
-76.50	2188.181	0.125210	4032.258	e8576s3i5.bin
-74.25	1883.086	0.106590	4032.258	e8576s3i80.bin
-72.00	1654.786	0.092520	4032.258	e8576s3i6.bin
-69.75	1477.829	0.081480	4032.258	e8576s3i79.bin
-67.50	1336.889	0.072570	4032.258	e8576s3i7.bin
-65.25	1222.190	0.065210	4032.258	e8576s3i78.bin
-63.00	1127.204	0.059000	4032.258	e8576s3i8.bin
-60.75	1047.406	0.053680	4032.258	e8576s3i77.bin
-58.50	979.564	0.049060	4032.258	e8576s3i9.bin
-56.25	921.305	0.044990	4032.258	e8576s3i76.bin
-54.00	870.850	0.041380	4032.258	e8576s3i10.bin
-51.75	826.841	0.038130	4032.258	e8576s3i75.bin
-49.50	788.221	0.035200	4032.258	e8576s3i11.bin
-47.25	754.157	0.032520	4032.258	e8576s3i74.bin
-45.00	723.984	0.030060	4032.258	e8576s3i12.bin
-42.75	697.164	0.027790	4032.258	e8576s3i73.bin
-40.50	673.261	0.025670	4032.258	e8576s3i13.bin
-38.25	651.914	0.023700	4032.258	e8576s3i72.bin
-36.00	632.824	0.021840	4032.258	e8576s3i14.bin
-33.75	615.742	0.020090	4032.258	e8576s3i71.bin
-31.50	600.459	0.018420	4032.258	e8576s3i15.bin
-29.25	586.799	0.016830	4032.258	e8576s3i70.bin
-27.00	574.612	0.015320	4032.258	e8576s3i16.bin
-24.75	563.773	0.013860	4032.258	e8576s3i69.bin
-22.50	554.173	0.012450	4032.258	e8576s3i17.bin
-20.25	545.722	0.011090	4032.258	e8576s3i68.bin
-18.00	538.342	0.009770	4032.258	e8576s3i18.bin
-15.75	531.968	0.008480	4032.258	e8576s3i67.bin
-13.50	526.545	0.007220	4032.258	e8576s3i19.bin
-11.25	522.028	0.005980	4032.258	e8576s3i66.bin
-9.00	518.381	0.004760	4032.258	e8576s3i20.bin
-6.75	515.573	0.003560	4032.258	e8576s3i65.bin
-4.50	513.583	0.002370	4032.258	e8576s3i21.bin

-2.25	512.395	0.001180	4032.258	e8576s3i64.bin
0.00	512.000	0.000000	4032.258	e8576s3i1.bin
2.25	512.395	-0.001180	4032.258	e8576s3i63.bin
4.50	513.583	-0.002370	4032.258	e8576s3i22.bin
6.75	515.573	-0.003560	4032.258	e8576s3i62.bin
9.00	518.380	-0.004760	4032.258	e8576s3i23.bin
11.25	522.028	-0.005980	4032.258	e8576s3i61.bin
13.50	526.544	-0.007220	4032.258	e8576s3i24.bin
15.75	531.967	-0.008480	4032.258	e8576s3i60.bin
18.00	538.341	-0.009770	4032.258	e8576s3i25.bin
20.25	545.721	-0.011090	4032.258	e8576s3i59.bin
22.50	554.172	-0.012450	4032.258	e8576s3i26.bin
24.75	563.772	-0.013860	4032.258	e8576s3i58.bin
27.00	574.611	-0.015320	4032.258	e8576s3i27.bin
29.25	586.797	-0.016830	4032.258	e8576s3i57.bin
31.50	600.457	-0.018420	4032.258	e8576s3i28.bin
33.75	615.740	-0.020090	4032.258	e8576s3i56.bin
36.00	632.822	-0.021840	4032.258	e8576s3i29.bin
38.25	651.911	-0.023700	4032.258	e8576s3i55.bin
40.50	673.258	-0.025670	4032.258	e8576s3i30.bin
42.75	697.161	-0.027790	4032.258	e8576s3i54.bin
45.00	723.980	-0.030060	4032.258	e8576s3i31.bin
47.25	754.152	-0.032520	4032.258	e8576s3i53.bin
49.50	788.216	-0.035200	4032.258	e8576s3i32.bin
51.75	826.836	-0.038130	4032.258	e8576s3i52.bin
54.00	870.844	-0.041380	4032.258	e8576s3i33.bin
56.25	921.298	-0.044990	4032.258	e8576s3i51.bin
58.50	979.556	-0.049060	4032.258	e8576s3i34.bin
60.75	1047.397	-0.053680	4032.258	e8576s3i50.bin
63.00	1127.192	-0.059000	4032.258	e8576s3i35.bin
65.25	1222.176	-0.065210	4032.258	e8576s3i49.bin
67.50	1336.872	-0.072570	4032.258	e8576s3i36.bin
69.75	1477.808	-0.081480	4032.258	e8576s3i48.bin
72.00	1654.759	-0.092520	4032.258	e8576s3i37.bin
74.25	1883.051	-0.106590	4032.258	e8576s3i47.bin
76.50	2188.133	-0.125210	4032.258	e8576s3i38.bin
78.75	2615.553	-0.151130	4032.258	e8576s3i46.bin
81.00	3255.540	-0.189800	4032.258	e8576s3i39.bin
83.25	4314.871	-0.253980	7353.000	e8576s3i45.bin
85.50	6388.625	-0.381960	7353.000	e8576s3i40.bin
87.75	12036.381	-0.700000	13889.000	e8576s3i42.bin
90.00	31250.000	-1.834780	31250.000	e8576s3i2.bin
92.25	12037.073	0.700000	13889.000	e8576s3i43.bin
94.50	6388.832	0.381960	7353.000	e8576s3i3.bin
96.75	4314.966	0.253980	7353.000	e8576s3i44.bin
99.00	3255.594	0.189800	4032.258	e8576s3i4.bin
101.25	2615.587	0.151130	4032.258	e8576s3i81.bin
103.50	2188.157	0.125210	4032.258	e8576s3i5.bin
105.75	1883.069	0.106590	4032.258	e8576s3i80.bin
108.00	1654.772	0.092520	4032.258	e8576s3i6.bin
110.25	1477.818	0.081480	4032.258	e8576s3i79.bin
112.50	1336.880	0.072570	4032.258	e8576s3i7.bin
114.75	1222.183	0.065210	4032.258	e8576s3i78.bin
117.00	1127.198	0.059000	4032.258	e8576s3i8.bin
119.25	1047.402	0.053680	4032.258	e8576s3i77.bin
121.50	979.560	0.049060	4032.258	e8576s3i9.bin
123.75	921.301	0.044990	4032.258	e8576s3i76.bin
126.00	870.847	0.041380	4032.258	e8576s3i10.bin
128.25	826.838	0.038130	4032.258	e8576s3i75.bin

130.50	788.219	0.035200	4032.258	e8576s3i11.bin
132.75	754.155	0.032520	4032.258	e8576s3i74.bin
135.00	723.982	0.030060	4032.258	e8576s3i12.bin
137.25	697.163	0.027790	4032.258	e8576s3i73.bin
139.50	673.260	0.025670	4032.258	e8576s3i13.bin
141.75	651.913	0.023700	4032.258	e8576s3i72.bin
144.00	632.823	0.021840	4032.258	e8576s3i14.bin
146.25	615.741	0.020090	4032.258	e8576s3i71.bin
148.50	600.458	0.018420	4032.258	e8576s3i15.bin
150.75	586.798	0.016830	4032.258	e8576s3i70.bin
153.00	574.612	0.015320	4032.258	e8576s3i16.bin
155.25	563.772	0.013860	4032.258	e8576s3i69.bin
157.50	554.173	0.012450	4032.258	e8576s3i17.bin
159.75	545.721	0.011090	4032.258	e8576s3i68.bin
162.00	538.341	0.009770	4032.258	e8576s3i18.bin
164.25	531.967	0.008480	4032.258	e8576s3i67.bin
166.50	526.545	0.007220	4032.258	e8576s3i19.bin
168.75	522.028	0.005980	4032.258	e8576s3i66.bin
171.00	518.381	0.004760	4032.258	e8576s3i20.bin
173.25	515.573	0.003560	4032.258	e8576s3i65.bin
175.50	513.583	0.002370	4032.258	e8576s3i21.bin
177.75	512.395	0.001180	4032.258	e8576s3i64.bin
180.00	512.000	0.000000	4032.258	e8576s3i1.bin

Chambered Phantom Collection Parameters

Table 27 Chambered phantom acquisition parameters.

Projection Angle θ (degrees)	Desired Bandwidth BW(θ) (kHz)	Freq.-Encoding Gradient G (G/cm)	Acquired Bandwidth BW'(θ) (kHz)	Converted MRI Output Filename
-175.50	513.583	-0.000592	4032.258	e10582s3i44.bin
-171.00	518.380	-0.001191	4032.258	e10582s3i42.bin
-166.50	526.544	-0.001805	4032.258	e10582s3i40.bin
-162.00	538.341	-0.002442	4032.258	e10582s3i38.bin
-157.50	554.171	-0.003114	4032.258	e10582s3i36.bin
-153.00	574.610	-0.003830	4032.258	e10582s3i34.bin
-148.50	600.456	-0.004606	4032.258	e10582s3i32.bin
-144.00	632.821	-0.005461	4032.258	e10582s3i30.bin
-139.50	673.257	-0.006420	4032.258	e10582s3i28.bin
-135.00	723.978	-0.007517	4032.258	e10582s3i26.bin
-130.50	788.214	-0.008801	4032.258	e10582s3i24.bin
-126.00	870.841	-0.010346	4032.258	e10582s3i22.bin
-121.50	979.551	-0.012267	4032.258	e10582s3i20.bin
-117.00	1127.186	-0.014753	4032.258	e10582s3i18.bin
-112.50	1336.863	-0.018148	4032.258	e10582s3i16.bin
-108.00	1654.746	-0.023135	4032.258	e10582s3i14.bin
-103.50	2188.109	-0.031311	4032.258	e10582s3i12.bin
-99.00	3255.486	-0.047460	4032.258	e10582s3i10.bin
-94.50	6388.419	-0.095511	6578.947	e10582s3i8.bin

-90.00	31250.000	-0.917606	62500.000	e10582s3i6.bin
-85.50	6389.038	0.095515	6578.947	e10582s3i7.bin
-81.00	3255.648	0.047461	4032.258	e10582s3i9.bin
-76.50	2188.181	0.031311	4032.258	e10582s3i11.bin
-72.00	1654.786	0.023135	4032.258	e10582s3i13.bin
-67.50	1336.889	0.018148	4032.258	e10582s3i15.bin
-63.00	1127.204	0.014753	4032.258	e10582s3i17.bin
-58.50	979.564	0.012267	4032.258	e10582s3i19.bin
-54.00	870.850	0.010346	4032.258	e10582s3i21.bin
-49.50	788.221	0.008801	4032.258	e10582s3i23.bin
-45.00	723.984	0.007517	4032.258	e10582s3i25.bin
-40.50	673.261	0.006420	4032.258	e10582s3i27.bin
-36.00	632.824	0.005461	4032.258	e10582s3i29.bin
-31.50	600.459	0.004606	4032.258	e10582s3i31.bin
-27.00	574.612	0.003830	4032.258	e10582s3i33.bin
-22.50	554.173	0.003114	4032.258	e10582s3i35.bin
-18.00	538.342	0.002442	4032.258	e10582s3i37.bin
-13.50	526.545	0.001805	4032.258	e10582s3i39.bin
-9.00	518.381	0.001191	4032.258	e10582s3i41.bin
-4.50	513.583	0.000592	4032.258	e10582s3i43.bin
0.00	512.000	0.000000	4032.258	e10582s3i4.bin
4.50	513.583	-0.000592	4032.258	e10582s3i44.bin
9.00	518.380	-0.001191	4032.258	e10582s3i42.bin
13.50	526.544	-0.001805	4032.258	e10582s3i40.bin
18.00	538.341	-0.002442	4032.258	e10582s3i38.bin
22.50	554.172	-0.003114	4032.258	e10582s3i36.bin
27.00	574.611	-0.003830	4032.258	e10582s3i34.bin
31.50	600.457	-0.004606	4032.258	e10582s3i32.bin
36.00	632.822	-0.005461	4032.258	e10582s3i30.bin
40.50	673.258	-0.006420	4032.258	e10582s3i28.bin
45.00	723.980	-0.007517	4032.258	e10582s3i26.bin
49.50	788.216	-0.008801	4032.258	e10582s3i24.bin
54.00	870.844	-0.010346	4032.258	e10582s3i22.bin
58.50	979.556	-0.012267	4032.258	e10582s3i20.bin
63.00	1127.192	-0.014753	4032.258	e10582s3i18.bin
67.50	1336.872	-0.018148	4032.258	e10582s3i16.bin
72.00	1654.759	-0.023135	4032.258	e10582s3i14.bin
76.50	2188.133	-0.031311	4032.258	e10582s3i12.bin
81.00	3255.540	-0.047461	4032.258	e10582s3i10.bin
85.50	6388.625	-0.095515	6578.947	e10582s3i8.bin
90.00	31250.000	0.917606	62500.000	e10582s3i5.bin
94.50	6388.832	0.095511	6578.947	e10582s3i7.bin
99.00	3255.594	0.047460	4032.258	e10582s3i9.bin
103.50	2188.157	0.031311	4032.258	e10582s3i11.bin
108.00	1654.772	0.023135	4032.258	e10582s3i13.bin
112.50	1336.880	0.018148	4032.258	e10582s3i15.bin
117.00	1127.198	0.014753	4032.258	e10582s3i17.bin
121.50	979.560	0.012267	4032.258	e10582s3i19.bin
126.00	870.847	0.010346	4032.258	e10582s3i21.bin
130.50	788.219	0.008801	4032.258	e10582s3i23.bin
135.00	723.982	0.007517	4032.258	e10582s3i25.bin
139.50	673.260	0.006420	4032.258	e10582s3i27.bin
144.00	632.823	0.005461	4032.258	e10582s3i29.bin

148.50	600.458	0.004606	4032.258	e10582s3i31.bin
153.00	574.612	0.003830	4032.258	e10582s3i33.bin
157.50	554.173	0.003114	4032.258	e10582s3i35.bin
162.00	538.341	0.002442	4032.258	e10582s3i37.bin
166.50	526.545	0.001805	4032.258	e10582s3i39.bin
171.00	518.381	0.001191	4032.258	e10582s3i41.bin
175.50	513.583	0.000592	4032.258	e10582s3i43.bin
180.00	512.000	0.000000	4032.258	e10582s3i4.bin

In Vivo Collection Parameters

Table 28 Acquisition parameters used during *in vivo* data collection.

Projection Angle θ (degrees)	Desired Bandwidth BW(θ) (kHz)	Freq.-Encoding Gradient G (G/cm)	Acquired Bandwidth BW'(θ) (kHz)	Converted MRI Output Filename
-171.00	518.382	0.001058	4032.258	E9306S1I5.bin
-162.00	538.347	0.002171	4032.258	E9306S1I7.bin
-153.00	574.627	0.003404	4032.258	E9306S1I9.bin
-144.00	632.857	0.004853	4032.258	E9306S1I11.bin
-135.00	724.054	0.006680	4032.258	E9306S1I13.bin
-126.00	871.013	0.009195	4032.258	E9306S1I15.bin
-117.00	1127.635	0.013111	4032.258	E9306S1I17.bin
-108.00	1656.349	0.020560	4032.258	E9306S1I19.bin
-99.00	3268.597	0.042177	4032.258	E9306S1I21.bin
-90.00	62500.000	-0.815458	62500.000	E9306S1I27.bin
-81.00	3268.542	-0.042177	4032.258	E9306S1I23.bin
-72.00	1656.335	-0.020560	4032.258	E9306S1I20.bin
-63.00	1127.629	-0.013111	4032.258	E9306S1I18.bin
-54.00	871.010	-0.009195	4032.258	E9306S1I16.bin
-45.00	724.053	-0.006680	4032.258	E9306S1I14.bin
-36.00	632.855	-0.004853	4032.258	E9306S1I12.bin
-27.00	574.626	-0.003404	4032.258	E9306S1I10.bin
-18.00	538.347	-0.002171	4032.258	E9306S1I8.bin
-9.00	518.382	-0.001058	4032.258	E9306S1I6.bin
0.00	512.000	0.000000	4032.258	E9306S1I4.bin
9.00	518.382	0.001058	4032.258	E9306S1I5.bin
18.00	538.347	0.002171	4032.258	E9306S1I7.bin
27.00	574.626	0.003404	4032.258	E9306S1I9.bin
36.00	632.855	0.004853	4032.258	E9306S1I11.bin
45.00	724.053	0.006680	4032.258	E9306S1I13.bin
54.00	871.010	0.009195	4032.258	E9306S1I15.bin
63.00	1127.629	0.013111	4032.258	E9306S1I17.bin
72.00	1656.335	0.020560	4032.258	E9306S1I19.bin
81.00	3268.542	0.042177	4032.258	E9306S1I21.bin
90.00	62500.000	0.815458	62500.000	E9306S1I26.bin
99.00	3268.597	-0.042177	4032.258	E9306S1I23.bin
108.00	1656.349	-0.020560	4032.258	E9306S1I20.bin

117.00	1127.635	-0.013111	4032.258	E9306S1I18.bin
126.00	871.013	-0.009195	4032.258	E9306S1I16.bin
135.00	724.054	-0.006680	4032.258	E9306S1I14.bin
144.00	632.857	-0.004853	4032.258	E9306S1I12.bin
153.00	574.627	-0.003404	4032.258	E9306S1I10.bin
162.00	538.347	-0.002171	4032.258	E9306S1I8.bin
171.00	518.382	-0.001058	4032.258	E9306S1I6.bin
180.00	512.000	0.000000	4032.258	E9306S1I4.bin

Appendix D

Appendix D: Code

A lot can be learned from the actual computer instructions used in the course of the project.

Presented here is a subset of the computer code developed, implemented, and used during the course of the project. The procedures that follow are the core procedures used to convert the acquired MRI imagery into sinograms, to back-project the created sinograms and to recombine the reconstructed spatial-spectral planes into a spatial-spatial-spectral volume. Also included is C code used to convert the acquired MRI images to 16 bit per pixel binary images suitable for use by the IDL procedures. Each procedure presented is commented further within the individual procedure.

Sinogram Creation Code

```
pro build_multiple, w1, Eventtop

        common msmri_common
        common msmri_widgets

        fulltime = systime( 1 )
        c = intarr( xraw, xraw )
        fullset = dblarr( nlns, yext, xraw )

        x_in = dblarr( xraw )
        x_out = dblarr( nlns )
        x_ina = dblarr( xraw )
        x_outa = dblarr( nlns )
        y_in = dblarr( yraw )
        y_out = dblarr( nlns )
        tmpib = dindgen( xraw )
        tmpis = dindgen( nlns )

        testdata = dblarr( yext )
```

```
bwout = sqrt( (b_max*b_min)^2 / ( (b_max * cos( !PI*acqdata.angle/180. ))^2 + $
                                    (b_min * sin( !PI*acqdata.angle/180. ))^2 ) )

for location=(yext/4),(3*yext/4) do begin

        openr, lun, acqdata.filename[location], /GET_LUN
        readu, lun, c

        if( isIBM ) then $
                c = swap_endian( c )

        maxc = max( c )

        c_norm = double(c) * double(max( acqdata.maxval ) / $
                                acqdata.maxval[location])

        close, lun
        free_lun, lun

        delta_bwin = double(acqdata.bandwidth[location]) / double( xext )
        start_bwin = double(-acqdata.bandwidth[location] / 2.0)
        x_in = start_bwin + delta_bwin * tmpib
        x_ina = reverse( x_in, 1 )

        delta_bwout = bwout[location] / double( nlns )
        start_bwout = -bwout[location] / 2.0
        x_out = start_bwout + delta_bwout * tmpis
        x_outa = reverse( x_out, 1 )

        scalor = ( bwout[location] / acqdata.bandwidth[location] * $
                                double(yraw) ) / double(nlns)

        for column=255L,255 do begin

                y_in[*] =c_norm[column,*]
                y_ina = reverse( y_in, 1 )

                y_out = INTERPOL( y_in, x_in, x_out )
                q = where( y_out lt 0.0, count )
                if( count ne 0 ) then y_out[q] = 0.0

                fullset[*,location,column] = y_out[*] * scalor

                if( (location - yext/4) eq 40 ) then $
                        fullset[*,location,column] = fullset[*,location-1,column]

                newloc = location + yext/2
                if( (newloc gt (3.0*yext/4.0)) and (newloc lt yext) ) then begin
                        y_out = INTERPOL( y_ina, x_ina, x_outa )
                        fullset[*,newloc,column] = y_out[*] * scalor
                endif

                newloc = location - yext/2
                if( (newloc gt -1.0) and (newloc lt (yext/4.0)) ) then begin
                        y_out = INTERPOL( y_ina, x_ina, x_outa )
                        fullset[*,newloc,column] = y_out[*] * scalor
                endif

        endfor  ;for each column

endfor  ;for each location (file)

interpped = congrid( fullset, nlns, yext, nlns )
WSET, w1

end
```

Backprojection Code

```
pro DoBackProjectAll, BPDraw, SinDraw

        common msmri_common
        common msmri_widgets

        c_out = fltarr( nlns, yext )                    ;Holds the sinogram
        projs = fltarr( nlns, yext )
        projsums = findgen( nlns )*0.0

        newdcvals = fltarr( nlns )
        for l=0,nlns-1 do begin
                dcvals = fltarr(yext)
                projs[*,*] = interpped[*,*,l]
                print,"Column = ", l, " Max = ", max( projs )
                for x=0,yext-1 do begin
                        line = projs[*,x]
                        line_f = fft( line, -1 )
                        dcvals[x] = line_f[0]
                endfor
                newdcvals[l] = total( dcvals ) / yext
        endfor

        q = where((filter ne 0), count)
        if( RamLakFilter and (count eq 0) ) then BuildFilter, "RamLak"

        for column=0L,(nlns-1) do begin

                if(max(interpped[*,*,column])-min(interpped[*,*,column]) gt 2.0) then begin

                        if( RamLakFilter ) then begin
                                s = size( filter )
                                tmpsp = fltarr(nlns+s(1)*2,nangs)
                                tmpsp[0:nlns-1,0:nangs-1] = interpped[*,*,column]
                                tmpsp = shift( tmpsp, s(1) )
                                tmpsp2 = convol( tmpsp, filter, 1.0 )
                                tmpsp2 = shift( tmpsp2, -s(1))
                                c_out[*,*] = tmpsp2[0:nlns-1,0:nangs-1]
                        endif else begin
                                c_out[*,*] = interpped[*,*,column]
                        endelse

                        tmpbpimage = fltarr( nlns, nlns )

                        if( (min( c_out ) ne 0.0) or (max( c_out ) ne 0.0) ) then begin
                                for j=nangs/4+pindex,(3*nangs/4)-1,bpdelta do begin

                                        riemann, c_out, tmpbpimage, (acqdata.angle[j] * $
                                                !PI/180.0), row=j, /backproject, cubic = -0.5

                                endfor
                        endif

                        tb_f = fft( tmpbpimage, -1 )
                        tb_f[0,0] = newdcvals[column]
                        bpimage[*,*,column] = abs(fft( tb_f, 1 ))
                endif
        endfor

        recs = fltarr( nlns, nlns )
        for l=0,nlns-1 do begin
                recs[*,*] = bpimage[*,*,l]
                print,"Column = ", l, " Max = ", moment( recs )
        endfor

        return

end
```

MRI Image Conversion Code

```
/* 5.x Compreseed Image Header  */

typedef struct pixhdr{
       long    img_magic;       /* magic number */
       long    img_hdr_length; /* length of total header in bytes and a
                               byte displacement to the 'pixel data area' */
       long    img_width;          /* width (pixels) of image */
       long    img_height;         /* height (pixels) of image */
       long    img_depth;          /* depth (1, 8, 16, or 24 bits) of pixel */
       long    img_compress;    /* type of compression; see IC_* below */
       long    img_dwindow;     /* default window setting */
       long    img_dlevel;          /* default level setting */
       long    img_bgshade;     /* background shade to use for non-image */
       long    img_ovrflow;     /* overflow value */
       long    img_undflow;     /* underflow value */
       long    img_top_offset; /* number of blank lines at image top */
       long    img_bot_offset; /* number of blank lines at image bottom */
       short   img_version;     /* version of the header structure    */
                               /* and a word to malongain 32 bit alignment */
       unsigned int  img_checksum; /* 16 bit end_around_carry sum of pixels */
       long    img_p_id;        /* a byte disp to unique image identifier */
       long    img_l_id;        /* byte length of unique image identifier */
       long    img_p_unpack;    /* a byte disp to 'unpack control' */
       long    img_l_unpack;    /* byte length of 'unpack control' */
       long    img_p_compress; /* a byte disp to 'compression control' */
       long    img_l_compress; /* byte length of 'compression control' */
       long    img_p_histo;     /* a byte disp to 'histogram control' */
       long    img_l_histo;     /* byte length of 'histogram control' */
       long    img_p_te;         /* a byte disp to 'text plane data' */
       long    img_l_text;      /* byte length of 'text plane data' */
       long    img_p_graphics; /* a byte disp to 'graphics plane data' */
       long    img_l_graphics; /* byte length of 'graphics plane data' */
       long    img_p_dbHdr;     /* a byte disp to 'data base header data' */
       long    img_l_dbHdr;     /* byte length of 'data base header data' */
       long    img_level0ffset; /* value to add to stored Pixel Data values */
                               /* to get the correct presentation value */
       long    img_p_user;       /* byte displacement to user defined data */
       long    img_l_user;       /* byte length of user defined data */
} PixHdr;

/*
Expand.c
*/
#include <stdio.h>
#include <fcntl.h>
#include <stdlib.h>
#include <sys/types.h>
#include <sys/stat.h>
/*#include <io.h>*/
#include <malloc.h>
#include <string.h>


#define   INBUFF_SIZE   8192
#define   OUTBUFF_SIZE  2*INBUFF_SIZE

int fillbuf( int handle, char *inbuff);

long expand( int in_handle, int out_handle,
                     long uncompressed_size, long compressed_size)
{
   unsigned char       *in_bot,*in_ptr,*in_top;
   unsigned short      p,inlimit,int_temp,last_pixel,*out_bot,*out_ptr,*out_top;
   long                out_count;
   unsigned int        output_bytes;
   FILE                *logfile;
   int                 j, ndump;
```

```
logfile = fopen( "test.log", "w" );
if(logfile == NULL)
{
   perror("\n Cannot Open the log file");
   exit(-1);
}

if( (out_bot = (unsigned short *) malloc( OUTBUFF_SIZE )) == NULL )
{
   printf("\n Not enough memory for file decompression ");
   return(0);
}
out_top=out_bot+INBUFF_SIZE;
out_ptr=out_bot;

if( (in_bot = (unsigned char *)malloc(INBUFF_SIZE)) == NULL )
{
   printf("\n Not enough memory for file decompression ");
   return(0);
}
in_top = in_bot + INBUFF_SIZE;
in_ptr = in_bot;

last_pixel = 0;
inlimit = fillbuf( in_handle, in_bot );
out_count = 0;

ndump = 0;
do
{
   int_temp = (unsigned short) * in_ptr++;
   compressed_size--;

   if( in_ptr == in_top )
   {
      inlimit = fillbuf( in_handle, in_bot );
      in_top = in_bot + inlimit;
      in_ptr = in_bot;
   }

   if ( int_temp<128 )
   {
      if( int_temp<64 )
         int_temp = last_pixel + int_temp;
      else
         int_temp = last_pixel - ( 64 - (int_temp & 63) );

   }
   else if( int_temp >191 )
   {
      p = (unsigned short) *in_ptr++;
      compressed_size--;

      if( in_ptr == in_top )
      {
         inlimit = fillbuf( in_handle, in_bot );
         in_top = in_bot + inlimit;
         in_ptr = in_bot;
      }
      int_temp = p << 8;

      p = (unsigned short) *in_ptr++;
      compressed_size--;

      if( in_ptr == in_top )
      {
         inlimit = fillbuf( in_handle, in_bot );
         in_top = in_bot + inlimit;
         in_ptr = in_bot;
      }

      int_temp = int_temp | (unsigned short) p;
```

```
      }
      else
      {
         int_temp = int_temp & 63;
         p = (unsigned short) *in_ptr++;
         compressed_size--;

         if( in_ptr == in_top )
         {
            inlimit = fillbuf( in_handle, in_bot);
            in_top = in_bot + inlimit;
            in_ptr = in_bot;
         }


         int_temp = int_temp << 8;
         int_temp += (unsigned short) p;

         if( int_temp < 8192 )
            int_temp += last_pixel;
         else
            int_temp = last_pixel - ( 8192 - ( int_temp & 8191 ) );
      }

      *out_ptr++ = int_temp;
      last_pixel = int_temp;

      if( out_ptr == out_top )
      {

/*       swab((char *)out_bot,(char *)out_bot,OUTBUFF_SIZE);*/

/*       if( ndump == 0 )*/
            for( j=0; j<(OUTBUFF_SIZE/2.0); j++ )
               fprintf(logfile,"%d\t%d\n", j, out_bot[j] );

         ndump++;

         if((write(out_handle,(char *)out_bot,OUTBUFF_SIZE)==-1))
            perror(" Error writing output file ");

         ndump++;

         out_count+=OUTBUFF_SIZE;
         out_ptr=out_bot;
      }
   } while( compressed_size != 0 );


   output_bytes = (int) ( uncompressed_size - out_count );
/*   swab((char *)out_bot,(char *)out_bot,output_bytes*2);*/

   fprintf( stderr,"^^^About to write to logfile\n" );
/*   if( ndump == 0 )*/
      for( j=0; j<(OUTBUFF_SIZE/2.0); j++ )
         fprintf( logfile, "%d\t%d\n", j, out_bot[j] );

   fprintf( stderr,"^^^About to write to out_handle\n" );
/*   if( (write( out_handle, (char *) out_bot, OUTBUFF_SIZE ) == -1 ) ) */
   if( (write( out_handle, (char *) out_bot, output_bytes ) == -1 ) )
      perror("Error writing output file ");

   fprintf( stderr,"^^^About to close logfile\n" );
   close( logfile );
   free(in_bot);
   free(out_bot);
   return(output_bytes - (long)(out_ptr-out_bot)*2);
}

/*
           fillbuf
```

```
 Function Description:

 fillbuf is a routine that will load the given buffer with
 INBUFF_SIZE of data.  If the function is unsucessful the program will
 be terminated.  The value returned is the number of bytes in
 the buffer.

 Call with:  file handle, char buffer

 Returns:  if sucessful:   number of bytes read
           else            -1
*/


int fillbuf( int handle, char *inbuff)
{
   int bytes;
   if( (bytes = read( handle, inbuff, INBUFF_SIZE )) == -1 )
   {
      perror("\n Could not read input file\n");
      return(-1);
  }

  return( bytes );
}

/*
MR2INT.C
*/
/* This is the 5.x image decompression code */
/* This is only a prototype.                */
#include <stdio.h>
#include <unistd.h>
#include <stdlib.h>
#include <sys/types.h>
#include <sys/stat.h>
#include <fcntl.h>
/*#include <io.h> */
#include "5ximage.h"

unsigned int swabint( unsigned int input );
unsigned long swablong( unsigned long input );
void Conv_header_2_PC_byte_order( PixHdr *ImagePtr );
extern long expand( int in_handle, int out_handle,
                    long uncompressed_size, long compressed_size);
int main( int argc, char **argv );

int main( int argc, char **argv )
{
   int         infile, outfile;
   struct stat stat_buf;
   PixHdr      ImgHeader;
   long        compressed_size, uncompressed_size, delta;

  /* set mask for file creating */
   umask( 022 );

   infile = open( argv[1], O_RDONLY );

   if( infile == -1 )
   {
      perror("\n Cannot Open the input file");
      exit(-1);
   }

  /* open output file. Create it if necessary */
   outfile=open(argv[2], O_RDWR | O_CREAT, 0744 );

   if( outfile == -1 )
   {
      perror("\n Cannot Open the output file");
```

```
      exit(-1);
   }

   read( infile, &ImgHeader, sizeof(ImgHeader) );

   fprintf( stderr,"\nMR File:\t%s.\n", argv[1] );
   fprintf( stderr,"\nImgHeader:\n" );
   fprintf( stderr,"\timg_magic:\t%d\n", ImgHeader.img_magic );
   fprintf( stderr,"\timg_hdr_length:\t%d\n", ImgHeader.img_hdr_length );
   fprintf( stderr,"\timg_width:\t%d\n", ImgHeader.img_width );
   fprintf( stderr,"\timg_height:\t%d\n", ImgHeader.img_height );
   fprintf( stderr,"\timg_depth:\t%d\n", ImgHeader.img_depth );
   fprintf( stderr,"\timg_compress:\t%d\n", ImgHeader.img_compress );
   fprintf( stderr,"\timg_dwindow:\t%d\n", ImgHeader.img_dwindow );
   fprintf( stderr,"\timg_dlevel:\t%d\n", ImgHeader.img_dlevel );
   fprintf( stderr,"\timg_bgshade:\t%d\n", ImgHeader.img_bgshade );
   fprintf( stderr,"\timg_ovrflow:\t%d\n", ImgHeader.img_ovrflow );
   fprintf( stderr,"\timg_undflow:\t%d\n", ImgHeader.img_undflow );
   fprintf( stderr,"\timg_top_offset:\t%d\n", ImgHeader.img_top_offset );
   fprintf( stderr,"\timg_bot_offset:\t%d\n", ImgHeader.img_bot_offset );
   fprintf( stderr,"\timg_version:\t%d\n", ImgHeader.img_version );
   fprintf( stderr,"\timg_checksum:\t%d\n", ImgHeader.img_checksum );
   fprintf( stderr,"\timg_p_id:\t%d\n", ImgHeader.img_p_id );
   fprintf( stderr,"\timg_l_id:\t%d\n", ImgHeader.img_l_id );
   fprintf( stderr,"\timg_p_unpack:\t%d\n", ImgHeader.img_p_unpack );
   fprintf( stderr,"\timg_l_unpack:\t%d\n", ImgHeader.img_l_unpack );
   fprintf( stderr,"\timg_p_compress:\t%d\n", ImgHeader.img_p_compress );
   fprintf( stderr,"\timg_l_compress:\t%d\n", ImgHeader.img_l_compress );
   fprintf( stderr,"\timg_p_histo:\t%d\n", ImgHeader.img_p_histo );
   fprintf( stderr,"\timg_l_histo:\t%d\n", ImgHeader.img_l_histo );
   fprintf( stderr,"\timg_p_te:\t%d\n", ImgHeader.img_p_te );
   fprintf( stderr,"\timg_l_text:\t%d\n", ImgHeader.img_l_text );
   fprintf( stderr,"\timg_p_graphics:\t%d\n", ImgHeader.img_p_graphics );
   fprintf( stderr,"\timg_l_graphics:\t%d\n", ImgHeader.img_l_graphics );
   fprintf( stderr,"\timg_p_dbHdr:\t%d\n", ImgHeader.img_p_dbHdr );
   fprintf( stderr,"\timg_l_dbHdr:\t%d\n", ImgHeader.img_l_dbHdr );
   fprintf( stderr,"\timg_levelOffset:\t%d\n", ImgHeader.img_levelOffset );
   fprintf( stderr,"\timg_p_user:\t%d\n", ImgHeader.img_p_user );
   fprintf( stderr,"\timg_l_user:\t%d\n", ImgHeader.img_l_user );

/*   Conv_header_2_PC_byte_order(&ImgHeader);*/

   fprintf( stderr,"^^^About to fstat\n" );
   fstat( infile, &stat_buf );
   fprintf( stderr,"^^^About to fseek to position:\t%d\n", ImgHeader.img_hdr_length );
   lseek( infile, ImgHeader.img_hdr_length, SEEK_SET );

  /* calculate compressed and uncompressed size */
   compressed_size = ( ((long)stat_buf.st_size) - ImgHeader.img_hdr_length );
   uncompressed_size = (long)( ImgHeader.img_width * ImgHeader.img_height *
                               ImgHeader.img_depth/8 );

   fprintf( stderr,"^^^About to decompress\n" );
  /* call function to decompress the file */
   delta = expand( infile, outfile, uncompressed_size, compressed_size);

  /* show info */
   fprintf( stdout, "\tCompressed size:\t%d\n\tUncompressed size:\t%d\n",
                     compressed_size, uncompressed_size - delta );

   fflush( stdout );

}

void Conv_header_2_PC_byte_order( PixHdr *ImgHeader )
{
   int                i;
   unsigned long      *ptr;


   ptr = (unsigned long *) ImgHeader;
```

```
    i = sizeof( PixHdr ) / sizeof( long );
    while(i--)
    {
        *ptr = swablong( *ptr );
        ptr++;
    }
}

unsigned int swabint( unsigned int input )
{
    unsigned inttemp;

    swab( (char *) &input, (char *) &temp, 2 );
    return( temp );
}

unsigned long swablong( unsigned long input )
{
    unsigned long       temp;

    swab( (char *) &input, (char *) &temp, 4 );
    temp = (temp<<16) + (temp>>16);
    return( temp );
}
```